

High-resolution spectroscopy
in superfluid helium droplets.
Investigation of vibrational fine
structures in electronic spectra of
phthalocyanine and porphyrin
derivatives.

Dissertation

zur Erlangung des Doktorgrades
der Naturwissenschaften (Dr. rer. nat.)
an der Naturwissenschaftlichen Fakultät IV
– Chemie und Pharmazie –
der Universität Regensburg



vorgelegt von
Ricarda Eva Friederike Elisabeth Riechers
aus Kling

Regensburg 2011

Promotionsgesuch eingereicht am 22.03.2011.

Diese Arbeit wurde angeleitet von Herrn Prof. Dr. Alkwin Slenczka am Institut für Physikalische und Theoretische Chemie der Universität Regensburg.

Prüfungsausschuss:

Prof. Dr. Nikolaus Korber, Vorsitzender

Prof. Dr. Alkwin Slenczka

Prof. Dr. Bernhard Dick

Prof. Dr. Alfons Penzkofer

The man in the glass

When you get what you want in your struggle for self,
And the world makes you king for one day,
Just go to a mirror and look at yourself,
And see what that man has to say.

For it isn't your father or mother or wife,
Whose judgment upon you must pass,
The fellow whose verdict counts most in your life,
Is the one staring back from the glass.

You may be like Jack Horner and chisel a plum,
And think you're a wonderful guy,
But the man in the glass says you're only a bum,
If you can't look him straight in the eye.

He's the fellow to please never mind all the rest,
For he's with you clear up to the end,
And you've passed your most dangerous, difficult test,
If the man in the glass is your friend.

You may get what you want down the pathway of years,
And get pats on the back as you pass,
But your final reward will be heartaches and tears,
If you've cheated the man in the glass.

Peter 'Dale' Wimbrow Sr.

Table of contents

1	Introduction and purpose of the study	1
2	Basic principles of superfluid helium droplets	4
2.1	Generation of superfluid helium droplets and their physical properties	4
2.2	Doping of superfluid helium droplets	8
3	Electronic spectroscopy of organic molecules in helium droplets	11
3.1	Excitation spectra of organic molecules in helium droplets	11
3.1.1	Zero phonon line (ZPL)	14
3.1.2	Phonon wing (PW)	15
3.2	Emission spectra of organic molecules in helium droplets	18
4	Experimental setup and methods of measurement	21
4.1	Measurements with continuous helium droplet beam	21
4.1.1	Layout of the helium droplet apparatus	21
4.1.2	Optical detection unit and laser system	24
4.1.3	Methods of measurement	25
4.1.3.1	Fluorescence excitation	25
4.1.3.2	Dispersed emission	25
4.2	Measurements with pulsed helium droplet beam	27
4.2.1	Layout of the pulsed helium droplet apparatus	27
4.2.2	Acquisition for fluorescence excitation and pulsed laser system	27
4.3	Chemicals	28

5	Reflected helium droplet beam	30
5.1	ZPL asymmetry and droplet size	31
5.2	Determination of mean droplet sizes	33
5.2.1	Case (1)	34
5.2.2	Case (2)	37
5.3	Interpretation of case (2) as reflected beam	38
5.3.1	Geometric examination	38
5.3.2	Examination of peak intensities	41
6	Phthalocyanine species	43
6.1	Chloroaluminiumphthalocyanine (AlClPc)	45
6.1.1	Fluorescence excitation of AlClPc	46
6.1.2	Dispersed emission of AlClPc	50
6.1.3	Fine structure in emission spectra of AlClPc-Ar ₁ complexes	54
6.2	2,9,16,23-Tetra- <i>tert</i> -butylphthalocyanine (TTBPc)	60
6.2.1	Fluorescence excitation of TTBPc	61
6.2.2	Dispersed emission of TTBPc	64
7	Porphyrin species	71
7.1	Free-base porphyrin (FBP)	73
7.1.1	Fluorescence excitation of FBP	74
7.1.2	Dispersed emission of FBP	80
7.2	5,15-Diphenylporphyrin (DPP)	82
7.2.1	Fluorescence excitation of DPP	83
7.3	5,10,15,20-Tetraphenylchlorin (TPC)	89
7.3.1	Fluorescence excitation of TPC	90
7.3.2	Dispersed emission of TPC	95
7.4	5,10,15,20-Tetramethylporphyrin (TMP)	98
7.4.1	Fluorescence excitation of TMP	99
7.4.2	Dispersed emission of TMP	104
7.5	5,10,15,20-Tetrapropylporphyrin (TPrP)	108

7.5.1	Fluorescence excitation of TPrP	109
7.5.2	Dispersed emission of TPrP	112
7.6	Etioporphyrin I (Etio)	115
7.6.1	Fluorescence excitation of Etio	116
7.6.2	Dispersed emission of Etio	118
7.7	Comparative summary of the porphyrin species	124
7.7.1	Fine structure of electronic transitions	124
7.7.2	Vibrational mode structure in dispersed emission	126
8	Conclusion	128
	Appendix	135
	HPLC analysis of FBP	136
	HPLC analysis of DPP	138
	HPLC analysis of TPP	140
	HPLC analysis of TPC	142
	HPLC analysis of TMP	144
	HPLC analysis of TPrP	145
	HPLC analysis of Etio	148
	References	149

1 Introduction and purpose of the study

Helium droplets serve as a cryogenic matrix since the rotationally resolved IR spectrum of SF₆ doped into helium droplets in 1995 revealed their low temperature of 0.37 ± 0.05 K [1]. Thereupon, numerous atoms (see for example [2, 3, 4]), inorganic and organic molecules (see for example [1, 5, 6, 7, 8, 9, 10, 11]), van der Waals complexes (see for example [12, 13, 14, 15]), radicals [16, 17] and several chemical reactions [18, 19] have been investigated using helium nanodroplets as host system (see also review articles [20, 21, 22, 23]). These experiments provide information on the molecular dynamics in a cold and dissipative environment as well as on the superfluid helium droplet and its dynamics itself. Superior to supersonic jet experiments where rotational temperatures of 1 K are easily reached while vibrational temperatures of 10 K may persist, superfluid helium droplets incorporating a molecule cool all degrees of freedom of the dopant to the same temperature safe in the sub-Kelvin regime at 0.37 K. Due to the dissipative medium, simplification of electronic spectra is achieved since only very few rotational levels remain occupied. Though, comparison with isolated molecules in supersonic jet expansions revealed significant deviations concerning electronic spectra of certain molecules (see for example [11, 24, 25, 26, 27, 28]). Phenomena such as line splitting, phonon wings or dramatic line broadening clearly point to a not yet entirely understood involvement of guest-host interactions. At first, line broadening effects were interpreted as a primary result of large amplitude motions like e.g. torsional motions [11, 24]. Though, not all molecules with the potential of large amplitude motions exhibit substantial

line broadening [11] and, additionally, even rigid molecules like e.g. 3-hydroxyflavone that do not allow for large amplitude motions may lead to significantly broadened spectra [28]. In order to further explore this problem, a series of suitable model compounds was investigated by means of high-resolution electronic spectroscopy being able to reveal sensitive guest-host interactions (cf. chapters 6 and 7).

In general, mechanisms that may cause line broadening in electronic spectra either depend on damping of nuclear rearrangement or disturbance of the electronic excitation process. Phthalocyanines and porphyrins, which are centrosymmetric molecules excluding the existence of a molecular dipole moment while higher moments may be present, are known to possess a rather rigid molecular backbone. Therefore, interaction of the molecule with the superfluid helium droplet can be assumed to be mainly mediated via differing substituent groups. Moreover, a considerably large variety of substituted compounds is commercially available and the electronic excitation spectra fit well into the spectral range covered by the continuous wave dye laser used for this study. Thus, several porphyrin and phthalocyanine derivatives substituted with different types and numbers of alkyl and aryl groups were chosen. This enables enquiring for a direct or indirect effect of low energy vibrational modes on the line width in electronic spectra of organic molecules doped into superfluid helium droplets.

Fluorescence excitation spectra of the electronic origins and dispersed emission spectra were recorded with a continuous helium droplet source combined with a continuous wave dye laser. In the case of fluorescence excitation spectra including vibrational modes, a pulsed source in combination with pulsed dye laser systems was used for the majority of substances. The latter became necessary since the photon flux provided by the continuous wave dye laser was not sufficient to record vibronic transitions for most porphyrin compounds due to the considerably low fluorescence quantum yields of the substituted porphyrins. Thus, a comparison of vibrational modes derived from dispersed emission spectra with the corresponding fluorescence excitation spectra finally became possible.

Within the course of this study also a replacement of the formerly used flow-through cryostat by a closed-cycle cryostat unit was performed. This made an adjustment procedure of the nozzle unit to the droplet beam axis defined by the openings of the skimmer and the pick-up cell necessary. It revealed that the helium droplets can be reflected into the detection chamber via collision with the skimmer if the nozzle is not adjusted to the actual droplet beam axis (cf. chapter 5).

2 Basic principles of superfluid helium droplets

This chapter provides in its first section an introduction into the general technique of producing superfluid helium droplets and their physical characteristics. In a second section, the process of doping helium droplets with foreign particles will be elucidated.

2.1 Generation of superfluid helium droplets and their physical properties

The p - T -phase diagram of the ^4He isotope (adapted from [29]) illustrates that helium undergoes a phase transition from the gas into the liquid phase but does not exhibit a further transition into the solid phase by lowering its temperature at pressures below 25 bar (see figure 2.1). However, by going below the limit of 2.17 K distinctive discontinuities of physical properties, e.g. a singularity in the heat capacity, are registered [30]. These observations are interpreted as the transition into a so-called superfluid phase. The phase boundary between liquid and superfluid phase is referred to as λ -line. The solid lines in figure 2.1 indicate the phase boundaries between solid, liquid, gas and superfluid phase. The absence of a triple point, where solid, liquid and gas phase are at equilibrium, marks another characteristic feature of ^4He and simultaneously provides evidence that helium clusters are liquid.

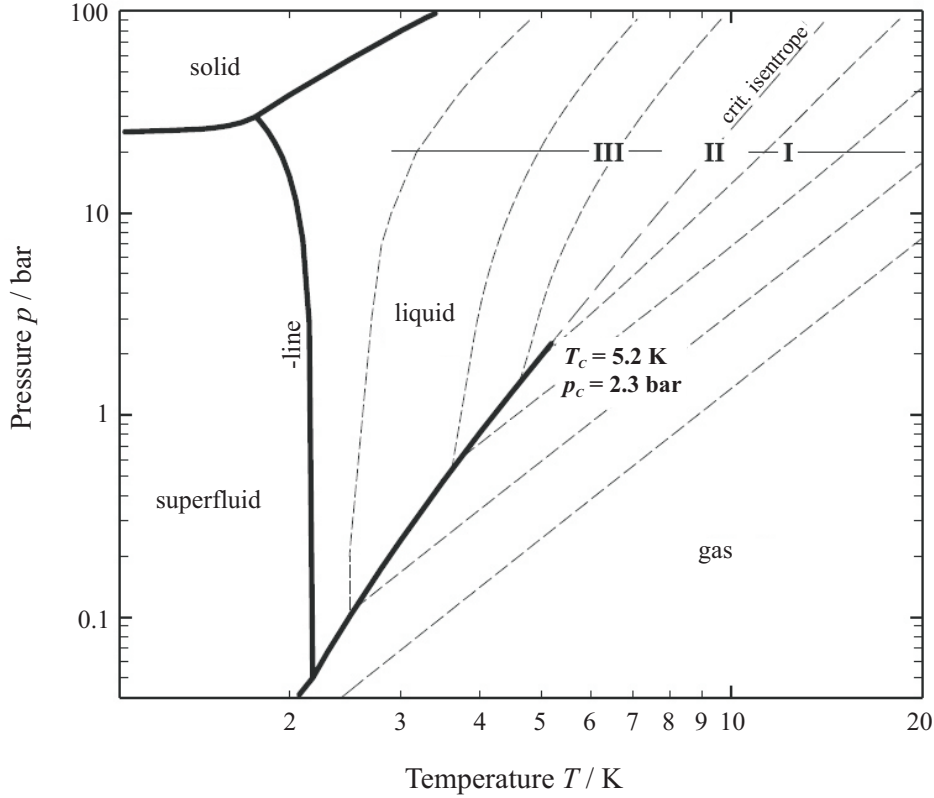


Fig. 2.1: Phase diagram of the ^4He isotope (adapted from [29]). The solid lines represent phase boundaries, the dashed lines indicate isentropes. T_c and p_c are the temperature and pressure at the critical point, respectively.

The generation of a directed beam of helium droplets results from the expansion of gaseous or liquid helium at high pressure (e.g. 20 – 30 bar) into the vacuum through a nozzle with a small opening diameter (e.g. $5 \mu\text{m}$) that is precooled to $T_0 < 20 \text{ K}$. The expansion corresponds to one of the isentropes in the phase diagram of ^4He (dashed lines in figure 2.1). Several typical isentropes are plotted in the phase diagram for three regions indicated from I to III. In region I, the so-called subcritical region, the expanded helium approaches the phase boundary between liquid and gas from the gaseous state. Consequently, droplets are formed by condensation of the gas. The critical isentrope which passes through the critical point ($T_c = 5.2 \text{ K}$ and $p_c = 2.3 \text{ bar}$) is denoted as II. In the region marked with III, referred to as supercritical, the approach of the liquid–gas phase boundary occurs from the liquid

state. Therefore, in the latter case, droplet generation takes place via fragmentation of the liquid phase.

The helium droplets formed in these three regions differ in both their mean size and their size distribution. For a stagnation pressure $p_0 = 20$ bar, the threshold between subcritical and supercritical expansion lies at $T_0 = 9.2$ K [31]. In case of the subcritical helium expansion, the droplet size distribution and the mean droplet size were either determined by deflecting the droplet beam with a second molecular beam consisting of either SF₆, Kr or Ar [32, 33] or by analyzing the droplet beam attenuation after electron impact ionization [34]. Very small helium clusters, on the other hand, i.e. less than 100 atoms, were investigated by diffraction from nanoscale transmission gratings making use of their wave character [35]. For droplet sizes in the range of $700 < N < 10^5$ atoms, the scattering experiments lead to a droplet size distribution which can be described by a log-normal distribution [32]:

$$f(N) = \frac{1}{Nd\sqrt{2\pi}} e^{-\frac{(\ln N - \mu)^2}{2d^2}} \quad (2.1)$$

with the two parameters μ and d . The mean droplet size \bar{N} subsequently results in

$$\bar{N} = e^{\mu + \frac{d^2}{2}} \quad (2.2)$$

where the standard deviation is

$$s_{\bar{N}} = \bar{N} \sqrt{e^{d^2} - 1} \quad . \quad (2.3)$$

However, if the helium clusters are produced via supercritical expansion the resulting droplets are too heavy to gain sufficiently large scattering angles in diffraction experiments. Thus, in this case the droplet size distribution which could be fitted with an exponential model was determined by deflection of afore ionized droplets in an electric field [36, 37, 38]. Yet, this method could only be used to investigate clusters within the range of $10^5 < N < 10^8$ helium atoms. Even larger droplets, comprising $N > 10^9$ atoms, were obtained by expanding compressed normal or superfluid liquid helium at $T_0 = 1.6 - 4.2$ K and $p_0 = 0.5 - 30$ bar [39]. Under these conditions, the size of the rather monodisperse droplets resulting from Rayleigh oscillation-induced breakup was determined by microscope observations.

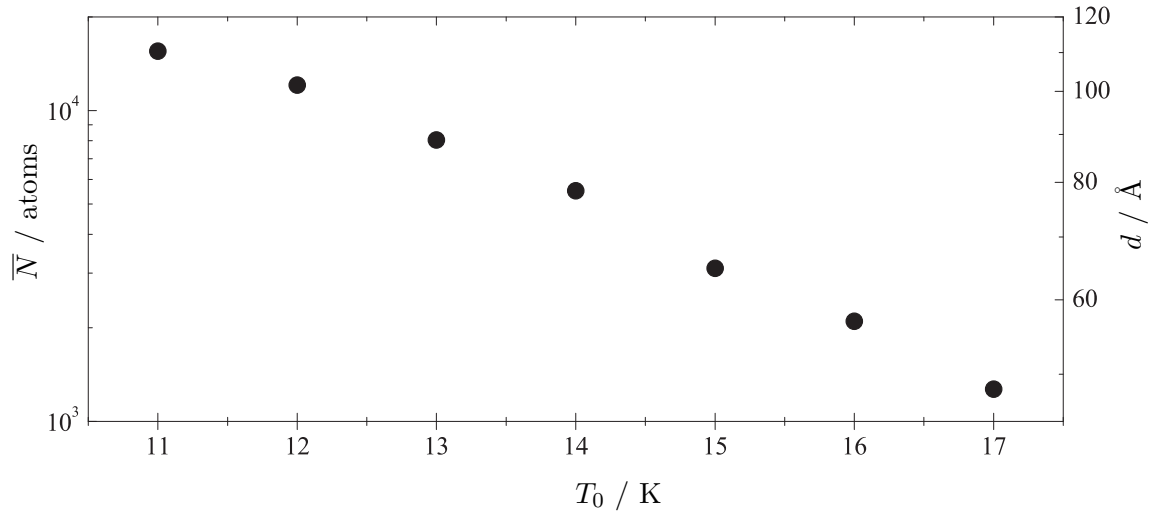


Fig. 2.2: Illustration of the mean droplet size \bar{N} and the diameter d of helium droplets resulting from an expansion at a stagnation pressure of $p_0 = 20$ bar depending on the nozzle temperature T_0 (plotted with data from reference [40]).

In the case of a subcritical expansion with a constant stagnation pressure of $p_0 = 20$ bar and varying nozzle temperatures T_0 from 11 up to 17 K, figure 2.2 displays the mean droplet size \bar{N} (left axis) based on data taken from reference [40]. The respective droplet diameters d which are displayed on the right ordinate, were determined by calculating the droplet radius r presuming a spherical cluster (following reference [41]) by using the number N of helium atoms per droplet with $r = r_0 \cdot N^{1/3}$. $r_0 = 2.22$ Å represents the radius of a single ${}^4\text{He}$ atom resulting from the density of superfluid helium. Generally, it can be stated that, for a given stagnation pressure, \bar{N} increases by lowering the nozzle temperature.

The velocity of the droplet beam produced from a nozzle with an orifice diameter of $5 \mu\text{m}$ at $p_0 = 20$ bar typically ranges from 215 m/s at $T_0 = 8$ K [31] to 360 m/s at $T_0 = 15$ K [34].

By using intensity profiles of the rotational fine structure from infrared spectra of OCS and SF₆ molecules in ${}^4\text{He}$ droplets, the droplet temperature was determined to be 0.37 ± 0.02 K [6] and 0.38 ± 0.01 K [42] respectively. This result indicates the superfluidity of the helium droplets, given that at this temperature and an inner

pressure p_i of approximately 1.3 bar (calculated from $p_i = \frac{2\gamma}{r}$ [43] with the surface tension $\gamma = 3.536 \cdot 10^{-4} \text{ Nm}^{-1}$ [44] and a droplet radius r of about 55 \AA for a mean droplet size of $\bar{N} = 15360$ helium atoms at $p_0 = 20 \text{ bar}$ and $T_0 = 11 \text{ K}$ [40]) only the superfluid phase exists (cf. figure 2.1).

Following their formation via adiabatic expansion, the droplets cool by evaporating single helium atoms from the droplet surface. At this, 4 to 5 cm^{-1} per atom [45, 46] are required to overcome the binding energy. Hence, the droplet temperature decreases continuously until the evaporation rate gets low enough to obtain a stationary state. According to [45, 46], this process takes 10^{-8} to 10^{-7} s and finally leads to the above-mentioned droplet temperature of 0.38 K .

2.2 Doping of superfluid helium droplets

To generate helium droplets doped with a single particle, the droplet beam has to pass a pick-up cell in which the respective substance is available in the gas phase at pressures of $1 \cdot 10^{-6}$ up to $3 \cdot 10^{-5} \text{ mbar}$ [6, 21, 47] depending on the length of the cell.

Making several assumptions, namely a monodisperse droplet size distribution as well as a constant capture cross section $\sigma_{k\text{oa}g}$ of the helium clusters (i.e. the droplet size is independent of the number of particles already doped into the droplet), the fraction $P_k(L)$ of helium clusters which are doped with k particles after passing a pick-up cell with the length L that provides a dopant particle density of n is given by a Poisson distribution [43]:

$$P_k(L) = \frac{(\sigma_{k\text{oa}g} n L)^k}{k!} e^{-\sigma_{k\text{oa}g} n L} \quad . \quad (2.4)$$

Solving

$$\frac{d}{dn} P_k(L) = 0 \quad (2.5)$$

one can deduce equidistant maxima with

$$n = \frac{k}{\sigma_{k\text{oa}g} L} \quad (2.6)$$

for $k > 0$. In figure 2.3 the respective functions for $k = 0..4$ are shown. In the case of $k = 0$ the result is a decreasing exponential function which accounts for the decreasing amount of bare droplets. For $k > 0$ the graphs start by increasing with n^k until a maximum is reached which is followed by an exponential decrease. The optimization of a certain particle number k is consequently accomplished by observing the spectroscopic signal of a particular (complex) species while tuning n in the pick-up cell until maximum signal is obtained.

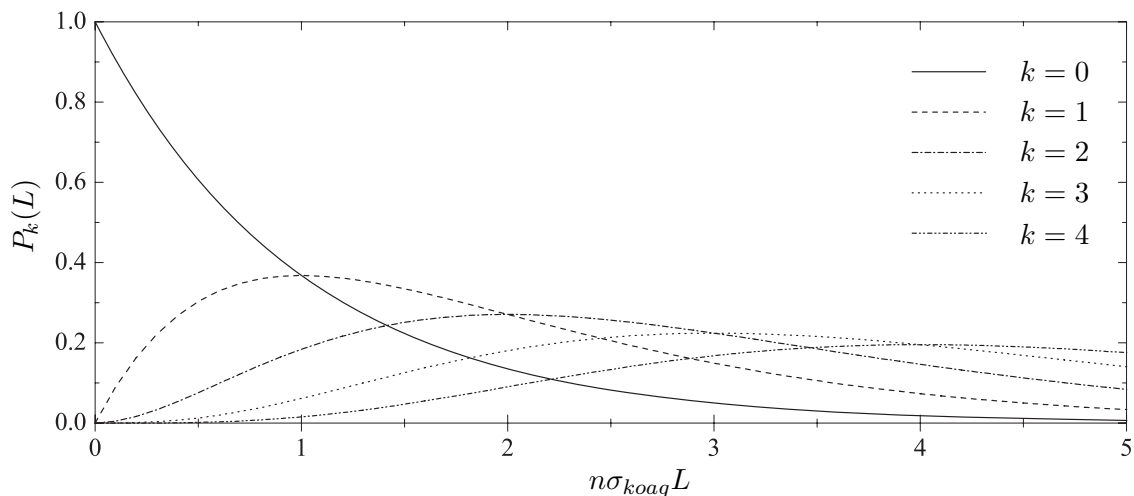


Fig. 2.3: Fraction of helium droplets $P_k(L)$ doped with k particles. n represents the particle density in the pick-up cell with the length L and σ_{koag} the capture cross section of the droplets.

Following the pick-up process, the embedded molecule transfers its translational, vibrational and rotational energy to the helium cluster. Similar to the behavior of the bulk phase, this energy dissipation becomes manifest in evaporation of helium atoms from the droplet surface. As mentioned before (see section 2.1), one evaporating helium atom leads to a dissipating energy equivalent of 5 cm^{-1} on average [45, 46]. In the case of SF_6 , by picking up a single molecule at room temperature, 612 ± 30 atoms of the helium cluster evaporate [43] while for the pick-up of the larger phthalocyanine molecule roughly 3000 evaporating atoms are estimated [48]. By means of this effective evaporative cooling, the captured species reach their final

temperature of 0.38 K, which is identical for all degrees of freedom, fairly quick (within less than 10^{-8} s [43]) compared to supersonic jet expansions or solid matrices. Dopant particles are classified according to their location within the helium droplet. Species residing on the droplet surface are denoted as heliophobe while those who penetrate into the droplet are referred to as heliophile. Reference [49] presents a simple model to predict the behavior of a certain species. It compares the depth of the potential well as well as the minimum distance of the helium–helium potential with the potential between helium and the captured species. Generally, closed-shell species penetrate into the helium droplet while alkali atoms (Li, Na, K, Rb and Cs) reside at the surface and alkaline earth metals (Mg, Ca, Sr and Ba) just have a shallow entrance depth (see review articles [50, 51]). Spectroscopically, heliophile species differ from heliophobe ones in terms of line widths where the former exhibit very narrow ($< 1 \text{ cm}^{-1}$ at the electronic origin and up to several wavenumbers for vibronic transitions) and the latter very broad (up to several hundred wavenumbers) lines widths(see for example [2, 3, 7, 26, 52]). All molecules investigated for the purpose of this study are closed-shell species and therefore belong to the class of heliophile molecules.

3 Electronic spectroscopy of organic molecules in helium droplets

This chapter describes the characteristics of electronic spectroscopy of molecules embedded in superfluid helium droplets. Since superfluid helium generally acts as a merely inert solvent which, compared to other low-temperature matrices like e.g. solid argon or n-octane, interacts only weakly with the dopant, the electronic transitions of a molecule doped into a superfluid helium droplet will be juxtaposed to the situation of a molecule isolated in a supersonic jet. The aim of recording electronic spectra of molecules in superfluid helium droplets for the purpose of this study and examining them concerning their matrix-related spectral features is to gain insight into the interaction between the dopant and its surrounding helium environment, in particular the nature of solvation.

3.1 Excitation spectra of organic molecules in helium droplets

Figure 3.1 schematically depicts the energy level diagram of the electronic ground state S_0 and the first electronically excited singlet state S_1 of a molecule in the gas phase compared to the situation in a matrix environment, for the present case a superfluid helium droplet. Besides the vibrational ground state also several vibrationally excited states for S_0 and S_1 are drawn as well as, for the vibrational ground states, quasi-continuous levels of the helium environment. In case of a cold

supersonic jet expansion, the cooling process provides low temperature so that the molecules are preferentially in the vibrational ground state of S_0 . The signals in the fluorescence excitation spectra, i.e. detecting the integrated fluorescence as function of the excitation frequency, reveals transitions from the lowest vibrational state of S_0 into the variety of vibrational levels of S_1 and, consequently, provide information about the (ro)vibrational structure in the excited state. At this, the transition with the lowest energy, from S_0 into the vibrational ground state of S_1 , is referred to as electronic origin or alternatively as 0_0^0 -transition. For both cases, supersonic jet and helium droplet spectroscopy, the radiative decay competes against non-radiative decay mechanisms such as internal conversion, internal vibrational redistribution or intersystem crossing.

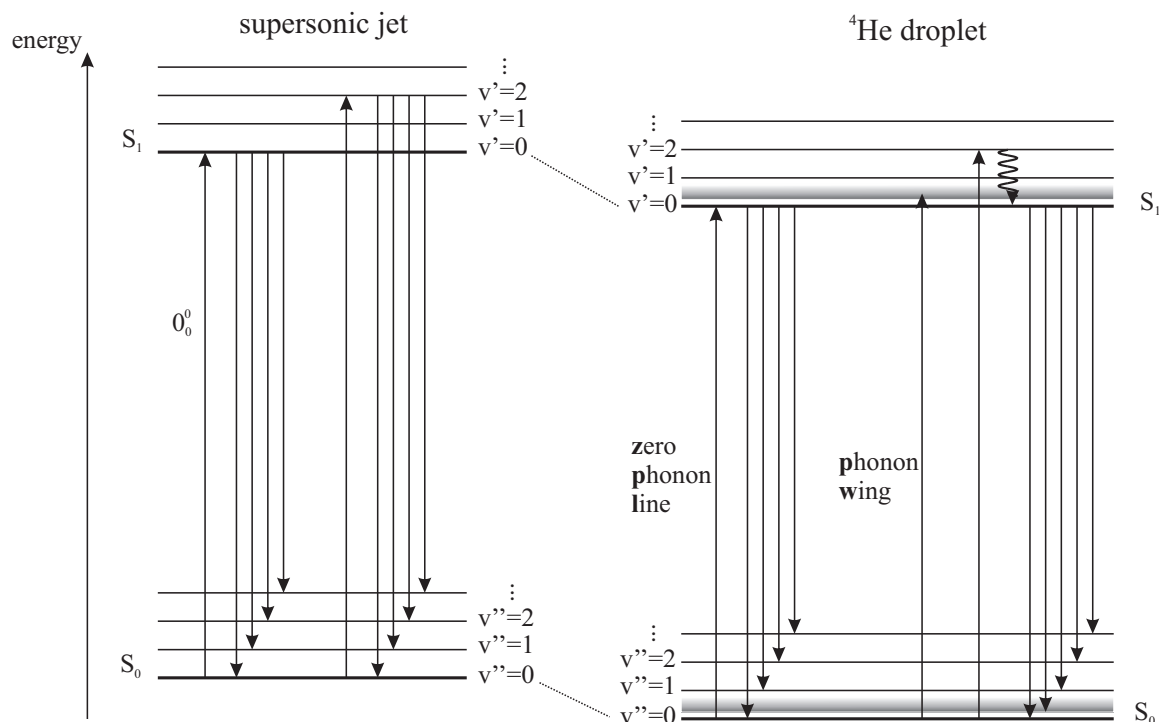


Fig. 3.1: Schematic comparison of electronic $S_1 \leftarrow S_0$ -transitions of organic molecules isolated in the gas phase with the situation of a matrix isolation in helium droplets. For details see text.

The transition frequency at the electronic origin in helium droplets is shifted compared to the supersonic jet experiments as the matrix environment provokes an energy reduction, i.e. a stabilization by solvation in the helium droplet, of both, the electronic ground and excited state, whereas the situation shown in figure 3.1 – a major drop of the excited state opposite to the ground state corresponding to an increased binding of the dopant to the droplet upon excitation – explains the fact that the 0_0^0 -transition of many molecules, like for instance anthracene, tetracene, phthalocyanine and porphyrin, doped into helium droplets is red shifted [7, 53, 54, 55, 56]. The spectral shift depends not only on the nature of the matrix environment, but, in the case of superfluid helium droplets, also on the cluster size [48, 57]. Though, by exciting rovibrational transitions no significant change is induced in the molecule's electron cloud and therefore most molecular vibrations are unaffected by the helium droplet environment, i.e. exhibit at most negligible shifts compared to the isolated molecule [20]. However, in the case of large amplitude motions, like e.g. torsional modes, broadening may occur [24].

Moreover, in helium droplets the matrix environment enables the coupling of the pure molecular transition with collective excitation states of the matrix. In the case of helium droplet spectroscopy, in general the term phonons is used, even if one distinguishes three types of elementary excitations in superfluid helium, namely phonons, ripplons (surface modes) and vortices (rotation modes) [58]. Phonons are imagined as volume compressional vibrations of the helium shell around a molecule which are simultaneously induced by electronically exciting the dopant molecule [21]. Therefore, besides the pure molecular transition which appears as zero phonon line (ZPL) in the excitation spectrum, also excitation of matrix states, called phonon wing (PW), are facilitated (see for example figures 3.2 and 3.3). Due to the low temperature of 0.38 K in the helium droplets, matrix states are not occupied in the electronic ground state. Thus, transitions exclusively occur from the electronic ground state into energetically higher lying matrix states coupled to molecular states of S_1 resulting in the fact that, in the excitation spectra, the PW always appears on the high-frequency side of the ZPL.

3.1.1 Zero phonon line (ZPL)

The ZPLs in the excitation spectra of many organic molecules in helium droplets are displayed as sharp lines with line widths below 1 cm^{-1} (see for example figure 3.3). In the case that pulsed lasers are used as the excitation source, the observed line width is often determined by the line width of the laser [50]. Otherwise, when high-resolution continuous wave lasers are utilized, the line width may be determined by Doppler broadening, power broadening or solely by the life time of the excited state. In the latter case, if only the homogeneous line width is dominating, the line is of Lorentzian shape. Regarding the merely minor matrix-related inhomogeneous broadening, mostly due to the lack of definite sites [50], this situation makes particularly apparent the advantages of the helium droplet isolation method over other low-temperature matrices for its use in high resolution spectroscopy of larger molecules by simplifying the spectra. However, the comparably small inhomogeneous line broadening due to the distribution of droplet sizes originating from the expansion can be used to deduce the droplet size distribution by analyzing the ZPL's shape [48, 59].

Several molecules like for example indole, 3-methylindole [60], anthracene [24], tetracene [61], perylene [8], biphenylene [62], Mg-phthalocyanine and Zn-phthalocyanine [26] exhibit a splitting of their ZPL. This phenomenon is not yet entirely understood but, for example in the case of tetracene, tentatively explained either by different conformations of a first non-superfluid shell of helium atoms around the molecule or by the tunneling of one or two localized helium atoms [61, 63].

The line widths of vibronic transitions can exceed the line width of the ZPL at the electronic origin. This reveals that vibrationally excited states possess a shorter lifetime compared to the vibrational ground state of S_1 . Therefore, one can assume that, preceded by efficient internal vibrational redistribution, fast energy dissipation into the surrounding helium droplet takes place.

Although various organic molecules exhibit sharp lines in their excitation spectra (cf. for example [7, 8, 10]), recent experiments concerning anthracene derivatives

revealed significant broadening of the electronic origin as well as for the vibronic transitions [11]. In the case of 9-phenylanthracene and 2-methylanthracene, the broadening of the excitation spectra could be reproduced by convolution of the respective supersonic jet spectra with a constant line width as single fit parameter. Since the broadening occurs in combination with large amplitude motions, namely torsional modes of the substituent group, it is presumably related to the change of the molecule's electron density distribution which is characterized by electrostatic moments such as dipole moment, quadrupole moment etc. [64]. A change of the size and orientation of the dipole moment, as is the case for 9-phenylanthracene and 2-methylanthracene, obviously leads to line broadening in the electronic spectra. The short time constants for damping, 0.1 ps and 0.3 ps for 9-phenylanthracene and 2-methylanthracene, respectively, are attributed to the fact that strong coupling between molecule and helium environment due to the geometry change enhances dissipation of pure vibrational excess as well as electronic excitation energy [11]. This explanation is also in agreement with the low fluorescence quantum yield exhibited by the two anthracene derivatives (cf. [11]).

3.1.2 Phonon wing (PW)

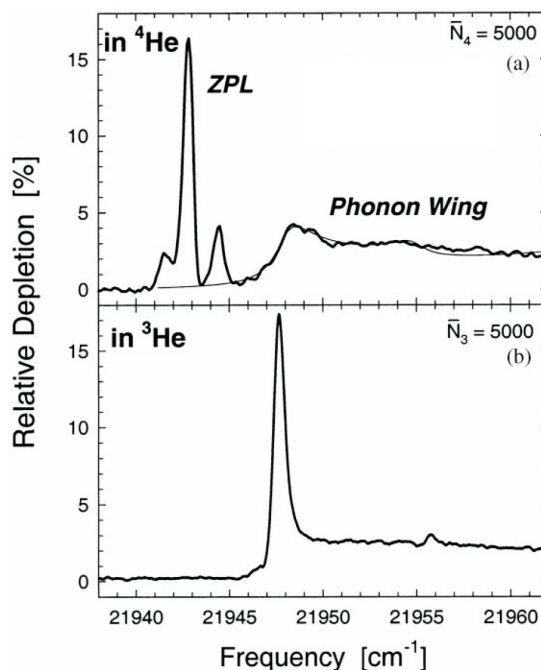
PWs appear on the blue side of the 0_0^0 -transition and all vibronic transitions (cf. section 3.1) illustrated as quasi-continuous levels exemplarily for the vibrational ground state of S_0 and S_1 in figure 3.1. The intensity ratio ZPL:PW is strongly dependent on the photon flux provided by the excitation laser. Since the transition probability of the ZPL is usually larger than that of the PW, the ZPL is readily saturated at moderate laser intensity while the PW is not (see for example figure 3.3). Since in the present study a continuous wave dye laser was used as well as two different pulsed dye lasers (see chapters 4.1.2 and 4.2.2) obviously drastically different photon fluxes were available which will be discussed in chapter 7 for several molecules.

The continuous wave dye laser used in this study (cf. chapter 4.1.2) with an output power of 100 – 350 mW measured directly behind the laser finally yields approxi-

mately 15 mW in the helium droplet apparatus. The latter value is estimated from measurements of the laser power directly in front of the entrance and exit windows of the machine which gave values of 20 mW and 10 mW respectively. Assuming a wavelength of 650 nm and a size of the light spot of 1 mm^2 the corresponding photon flux amounts to $4.91 \cdot 10^{22} \text{ m}^{-2}\text{s}^{-1}$. Contrarily, by using a pulsed dye laser with an output energy measured directly behind the laser of 1.3 mJ up to 13 mJ and a pulse length of 10 ns, the laser power inside the machine can be estimated to be $1.3 \cdot 10^4 \text{ W}$ up to $1.3 \cdot 10^5 \text{ W}$. Assuming typical experimental conditions with a light spot of 9 mm^2 and a wavelength of 650 nm, the photon flux in this case amounts to $4.73 \cdot 10^{27} \text{ m}^{-2}\text{s}^{-1}$ or $4.73 \cdot 10^{28} \text{ m}^{-2}\text{s}^{-1}$. Thus, an increase of the photon flux of five or six orders of magnitude is achieved by using pulsed lasers. Within this range, saturation of the ZPL and also of the PW can be reached as has been discussed in reference [24].

Generally, PWs are observed exclusively in combination with electronic excitation. Even though, one group claims the existence of PWs in the infrared spectrum of methane when using high laser power [58]. However, examining the presented spectra, the existence of additional absorption bands blueshifted to the vibrational

Fig. 3.2: Electronic origin of the fluorescence excitation spectrum of glyoxal in a) ^4He and b) ^3He droplets (taken from ref. [65]). The thin solid line in the upper spectrum corresponds to the fit of the density of states distribution of superfluid ^4He to match the spectral shape of the phonon wing (see text).



transitions is not obvious.

In the case of glyoxal the gap of 5 cm^{-1} between ZPL and PW in the fluorescence excitation spectrum as well as the spectral structure of the PW could be reproduced satisfactorily by computer simulations [66] (see figure 3.2 upper spectrum). The simulations were based on the state density distribution of the phonons in the superfluid bulk phase of ^4He which was obtained from neutron scattering experiments (see ref. [67] and references therein). Since the spectral shape of the PW can be well approximated with the dispersion curve of elementary excitations of the bulk superfluid, this study was interpreted as the strongest evidence for superfluidity

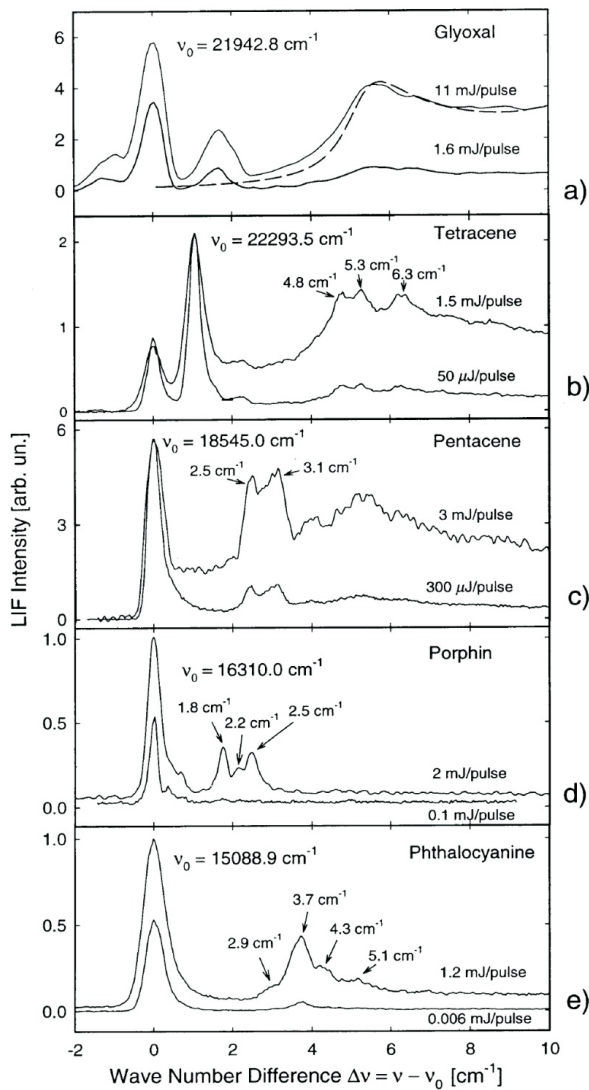


Fig. 3.3: Fluorescence excitation spectra of glyoxal, tetracene, pentacene, porphyrin, and phthalocyanine in ^4He droplets measured with different laser intensities respectively as indicated for each panel (taken from reference [7]). For details see text.

of helium droplets [66]. In order to support this assumption the fluorescence excitation spectrum of glyoxal in pure non-superfluid ^3He droplets was recorded [65] (see figure 3.2 lower spectrum). This spectrum shows no gap between ZPL and PW corresponding to the dispersion curve of the (under the experimental conditions of droplet formation following the expansion of the gas through a nozzle into a high vacuum chamber) normally fluid ^3He isotope which exhibits the density of states distribution of a classical liquid. Moreover, the rotational fine structure of the ZPL, and thus, the free rotation of the molecule, is suppressed.

For several other molecules like for example tetracene, pentacene, porphyrin and phthalocyanine one finds a gap between ZPL and PW [7] notwithstanding the size of the ZPL–PW gap as well as the spectral structure of the phonon wing vary for different molecules. Particularly, for the four molecules just mentioned the distinctive fine structure of the PW with pronounced maxima differs significantly from the broad and rather unstructured PW which was found for glyoxal (cf. figure 3.3) or bulk superfluid helium. The attempt to explain these experimental results is based on the assumption that larger aromatic molecules interact more intensely with the surrounding helium than the comparably small glyoxal molecule. Hence, the spectral shape of the PW is considered to reflect the excitation of a localized solvation layer of helium atoms around larger molecules [7]. Several computer simulations were able to provide evidence for the verification of a shell consisting of few helium atoms tightly attached to the respective molecule [63, 68, 69, 70].

3.2 Emission spectra of organic molecules in helium droplets

In general, dispersed emission spectra of organic molecules in helium droplets exhibit sharp lines with line widths of about 1 cm^{-1} at which the line width is predominantly limited by the spectral resolution of the experimental setup [52]. An additional broad feature ($\sim 50\text{ cm}^{-1}$) occurs on the low-energy side next to each sharp line [8, 52].

According to the ZPL and the PW in the excitation spectra, this experimental result is interpreted as a pure molecular transition in case of the sharp line and as a phonon transition coupled to a pure molecular transition in case of the low-frequency component (cf. figure 3.1). At this, the transition frequency as well as the relative intensity of the weaker signal is independent of the excitation energy and exclusively determined by the Franck-Condon factors [8].

Emission takes place only after any excessive vibrational or other excitation energy of the dopant is dissipated into the droplet environment (see figure 3.1) which causes, similar as for the doping process (cf. chapter 2.2), evaporation of helium atoms from the droplet surface. The dissipation process is proved by the fact that molecules excited into high-energy vibrational transitions solely emit at the same frequencies as those excited at the 0_0^0 -transition [52].

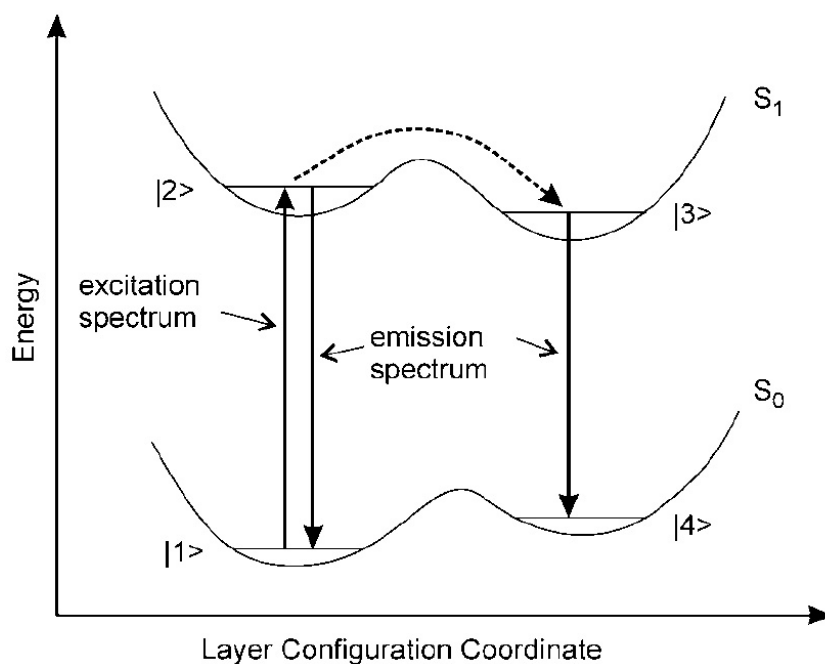


Fig. 3.4: Schematic depiction to explain the line splitting that large organic molecules exhibit in their emission spectra following the relaxation of the surrounding helium solvation shell (taken from reference [27]). For more details see text.

For some molecules, for example phthalocyanine and Mg-phthalocyanine, the emission spectrum reveals a line splitting. Analogous to the excitation spectra, this phenomenon is interpreted by assuming a non-superfluid shell consisting of a defined number of helium atoms around the dopant which exhibits various metastable and one stable configuration [27]. The corresponding scheme of quantized solvation states in helium droplets and their effect on the emission spectrum of a doped molecule is illustrated in figure 3.4. Allowing for stable and metastable configurations of the solvation shell the photocycle displayed in figure 3.4 was deduced from the line doubling in the emission spectra of phthalocyanine. After electronic excitation from the ground state S_0 ($|1\rangle$) into the S_1 state ($|2\rangle$) the system decays either directly back into S_0 ($|1\rangle$) or relaxation of the solvation shell into a second conformation of the solvation shell ($|3\rangle$) (dashed arrow) followed by emission into a metastable state of S_0 ($|4\rangle$) takes place. This interpretation was confirmed by path-integral Monte-Carlo simulations which revealed two configurations of phthalocyanine solvated in helium droplets for S_0 and S_1 [70].

4 Experimental setup and methods of measurement

The experiments for the purpose of this study were performed on two different experimental setups. On the one hand spectra were taken by using an apparatus comprising a continuous nozzle combined with a continuous wave laser, on the other hand an apparatus comprising a pulsed nozzle in combination with a pulsed excitation laser was used.

4.1 Measurements with continuous helium droplet beam

The continuous helium droplet apparatus was mainly used for locating the electronic origin of the majority of substances as well as for recording highly resolved fluorescence excitation spectra of the electronic origins. Furthermore, all of the dispersed emission spectra shown in this work have been acquired with the continuous setup.

4.1.1 Layout of the helium droplet apparatus

The apparatus for the production of a continuous beam of superfluid helium droplets comprises two differentially pumped vacuum chambers (see figure 4.1).

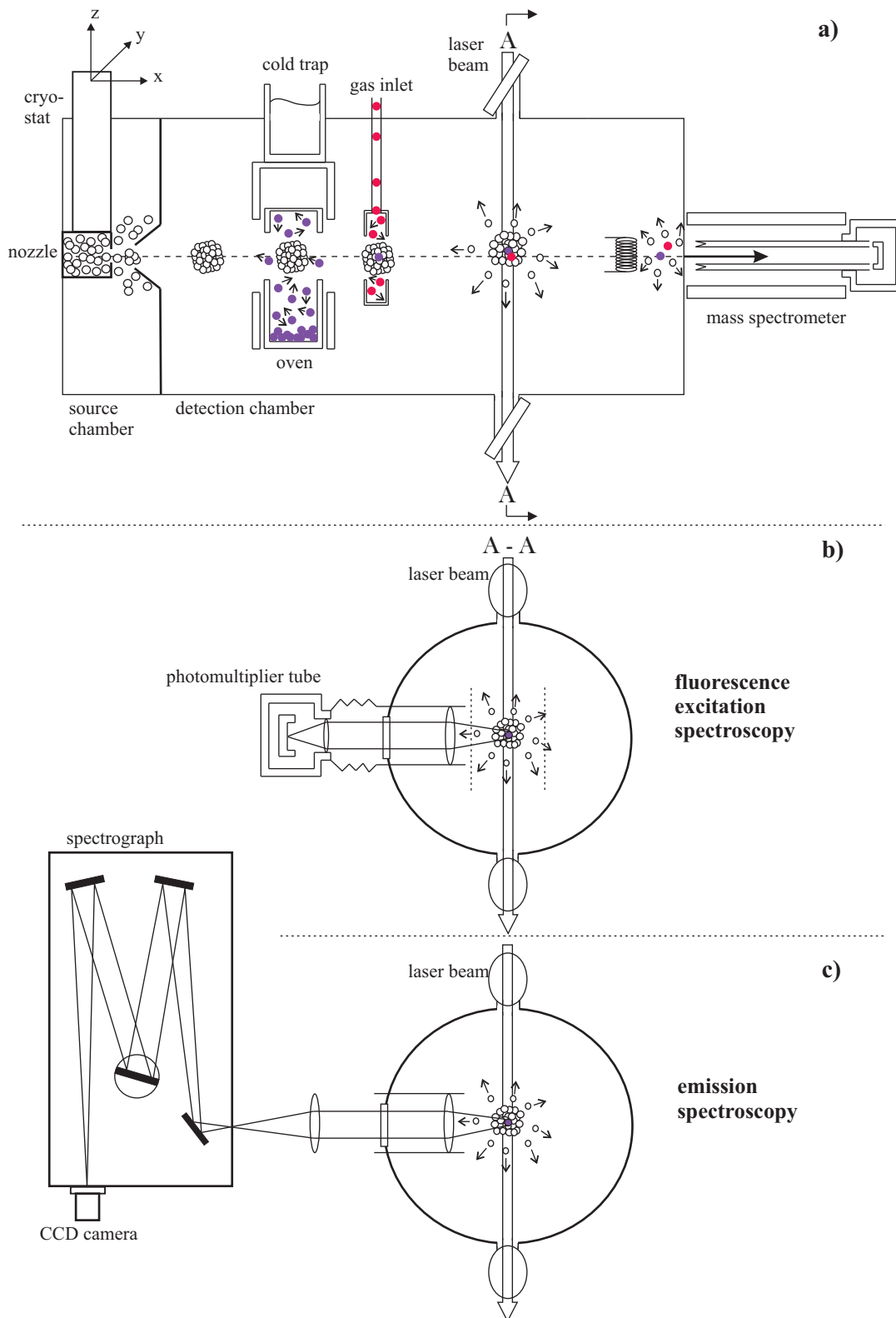


Fig. 4.1: Schematic depiction of the apparatus to record fluorescence excitation and dispersed emission spectra of organic molecules in superfluid helium droplets.

The nozzle or source chamber (at an operating pressure of about $4.6 \cdot 10^{-5}$ mbar) is evacuated by an oil diffusion pump (Leybold DI 6000 E) and a unit consisting of a roots pump (Leybold Ruvac WAU 251) and a rotary vane pump (Leybold Trivac D65B). It contains the continuous flow nozzle with an opening diameter of $5 \mu\text{m}$ which is cooled by a closed-cycle cryostat (Sumitomo cold head RDK-408S2 and compressor unit F-50Hw). The nozzle–cryostat unit can be adjusted in all three dimensions, also during operation. By expansion of highly purified ^4He (purity 99.9999 %) into the vacuum chamber at stagnation pressures of 20 to 30 bar and nozzle temperatures of 10.8 up to 13.5 K ^a, depending on the requirements for the pick-up procedure (see chapter 2.2), a continuous beam of superfluid helium droplets is formed. Approximately 2 cm past the nozzle, the droplet beam passes through the trombone shaped skimmer with an opening diameter of 2 mm which separates the source chamber from the detection chamber.

The detection chamber is evacuated by a turbomolecular pump (Pfeiffer TPU 510) and a rotary vane pump (Edwards RV12) to reach a pressure of about 10^{-7} mbar during operation. Approximately 9 cm past the skimmer, the droplet beam enters into the pick-up cell which consists of a cylindrical stainless steel oven. The oven has an inner diameter of 2 cm and two opposite openings with diameters of 4 mm for the pass through of the droplet beam. The pick-up cell is resistively heatable up to 400 °C via a heating wire which is wound around the outer wall of the oven. A cylindrical copper shield covers the entire pick-up unit. It is in thermal contact with a reservoir of liquid nitrogen. This device serves as a cryopump for background gas, mostly water, and for the dopant species evaporating from the oven. In addition, it shields the photon detectors from thermal radiation. Optionally, a second pick-up cell for gaseous species can be inserted into the droplet beam path. About 8 cm downstream the oven, the helium droplet beam is perpendicularly intersected by the

^aAn accurate determination of the nozzle temperature itself is virtually impossible due to the placement of the temperature sensor, a square-shaped Pt100 (2 x 2 mm), which is mounted close to the nozzle but can not be directly attached to the nozzle itself. Therefore, the expression *system temperature* instead of *stagnation temperature* will be used henceforth.

laser beam which enters the chamber through a Brewster window. At the end of the detection chamber, a quadrupole mass spectrometer (Inficon Transpector H300M) with a detection range of mass to charge $m/z = 1 - 300$ amu is mounted. It is used for two purposes: firstly, to monitor or optimize the droplet beam axis by varying nozzle or oven position, secondly, to observe the amount of substance transported by the droplets in case the molecule's mass or one of its fragments fits into the mass range.

4.1.2 Optical detection unit and laser system

The optical detection unit resides perpendicularly to both the helium droplet beam and the intersecting laser beam. It comprises a PMT (photomultiplier tube) (Hamamatsu R943-02) for the detection of the integrated fluorescence (cf. figure 4.1 b) as well as a CCD-camera (charge coupled device) (Andor DU401-BV) mounted at the exit port of a spectrograph (Spex 1870 C) to register dispersed emission spectra (cf. figure 4.1 c). The emerging fluorescence light is collected by a lens with a focal length of 6 cm and either imaged onto the cathode of the PMT or, by use of a second lens, focussed onto the spectrograph's entrance slit.

To record excitation spectra, a glass color filter which eliminates scattered light from the laser is inserted into the optical path in front of the photomultiplier tube.

The spectrograph in Czerny-Turner configuration has a focal length of 50 cm and is equipped with a 1200 lines/mm grating. The chip of the CCD-camera mounted at the exit slit contains 1024 x 256 pixels with a pixel width of 26 μm .

The laser used for the purpose of this study is a continuously tunable continuous wave dye laser (Coherent Innova 899-29 autoscan) pumped by an Ar^+ ion laser (Coherent Innova Sabre R). In the range of 380 to 750 nm, the line width of the dye laser operated in single mode is about 500 kHz. The laser frequency is determined via a wavemeter.

4.1.3 Methods of measurement

4.1.3.1 Fluorescence excitation

In the case of fluorescence excitation spectra, the principle of measurement is based on tuning the excitation laser over a certain wavelength range. This is accomplished by the so-called burst mode: the laser is kept fixed at a certain wavelength while recording the integrated fluorescence light by the PMT (cf. chapter 3.1) before a new wavelength is set. The PMT is sensitive for the red spectral region and therefore cooled down to $-25\text{ }^{\circ}\text{C}$ to minimize thermal noise. To detect the integrated fluorescence, the PMT's signal is amplified by a factor of five (Stanford Research Systems SR 445) and subsequently recorded by a photon counter (Stanford Research Systems SR 400). As there are two different computers, one for the control of the laser and one for the acquisition and processing of the photon counter data, a synchronization of wavelength change and fluorescence data acquisition has to be implemented: after the elapse of a predefined delay time, the photon counter sends a trigger pulse to the laser control unit which induces a frequency change according to a predefined frequency interval. Subsequently, the laser control unit sends a pulse to the photon counter to start a new acquisition time. Simultaneously to triggering of the laser control unit, the photon counter initiates a readout of the counted events by the data acquisition computer. The latter stores the data and graphically displays them simultaneously. The information about the wavelength change after each frequency step are recorded by the computer controlling the laser. Finally, both files which contain the same number of data points can be merged to match frequency and fluorescence signal intensity.

4.1.3.2 Dispersed emission

Recording of dispersed emission spectra is accomplished by keeping the laser frequency fixed at a molecular resonance and feeding the fluorescence into the spectrograph. The CCD-camera of the spectrograph is cooled down to $-70\text{ }^{\circ}\text{C}$ to reduce

thermal noise. The computer-aided data acquisition was performed in full vertical binning mode which means that the signal of the 256 pixels of a vertical column is integrated prior to readout. Signals from cosmic radiation are eliminated by the camera software (Andor SOLIS for Spectroscopy 4.4.0.0I2C). Finally the spectrum consists of 1024 data points representing the fluorescence intensity I . Since the spectrograph's mechanics for positioning of the grating does not enable to reproducibly approach a specific wavelength, a calibration procedure has to be performed following each new wavelength setting to assign each of the 1024 columns to a specific wavelength. The wavelength calibration is accomplished by recording the spectrum of an Ar/Ne lamp whose emission wavelengths are accurately known and tabulated [71]. A calibration function $\lambda(x)$ is generated where x is the column number of the CCD-chip and λ the respective wavelength. The calibration function is predominantly linear with a minor quadratic term (e.g. $\lambda(x) = -1171.053(8) + 1.411(9) \cdot x - 3.5(7) \cdot 10^{-5} \cdot x^2$ for a position of the grating at 670.000 nm). With help of the fitted equation, the numbers of the data points x are transformed in wavelengths λ . Since all spectra shown in this work feature a wavenumber scale instead of a wavelength scale, finally, a Jakobi transformation of the measured fluorescence intensity values has to be conducted due to the non-linear relationship between wavelength and wavenumber. This conversion is accomplished for each $\Delta\lambda$ by calculating the corresponding $\Delta\bar{\nu}$ as well as the ratio $I/\Delta\bar{\nu}$. Hence, an intensity value per wavenumber interval of 1 cm^{-1} is obtained which can be plotted versus a linear wavenumber scale.

The wavenumber range covered per pixel of the CCD-chip was determined to be approximately 1 cm^{-1} considering the frequency range used in this work [52].

Despite of cooling the CCD-chip, a technically related background signal, differing for each column, is always recorded. Thus, a background spectrum taken with closed entrance slit of the spectrograph is subtracted from any emission spectra.

Be it that emission directly occurs at the excitation wavelength of the laser, a background spectrum without the sample (accomplished by misalignment of the oven apertures relative to the droplet beam axis) needs to be subtracted.

4.2 Measurements with pulsed helium droplet beam

The apparatus operated with a pulsed droplet source as well as the corresponding process of data acquisition has been described in detail in reference [24]. Therefore only a brief description will be given in the following.

The pulsed machine was mainly used for the weakly fluorescent porphyrin molecules in order to gain signal intensity by saturation. This was accomplished by means of a pulsed dye laser which provides a much higher photon flux compared to the continuous wave laser (cf. chapter 3.1.2).

4.2.1 Layout of the pulsed helium droplet apparatus

The layout of the pulsed helium droplet apparatus is essentially the same as the one used for producing a continuous beam of helium droplets concerning its composition of two differentially pumped vacuum chambers – a source chamber and a detection chamber separated by a skimmer – as well as the geometry of the detection unit. The characteristic feature of the pulsed machine is the fact that a pulsed valve (Even-Lavie valve Type E.L.-5-C-2005) is used. A detailed description of this nozzle and its characterization concerning the production of pulses of superfluid helium droplets can be found in reference [72].

Typical operation conditions were a valve repetition rate of either $R = 20$ Hz or $R = 50$ Hz depending on the excitation laser, a stagnation pressure of $p_0 = 80$ bar and a system temperature of $T_0 = 21.5$ K. These values correspond to droplet sizes of $10^4 < N < 10^6$ atoms [72].

4.2.2 Acquisition for fluorescence excitation and pulsed laser system

The data acquisition to record fluorescence excitation spectra requires temporally synchronization of the helium droplet pulse, the pulse of the excitation laser, and

the detection of fluorescence light. Synchronization is achieved by using a home-built trigger pulse generator [73]. This device is internally running on a predefined frequency corresponding to the frequency of the laser and nozzle pulses. Firstly, the pulse generator sends a trigger pulse to initiate the opening of the nozzle. Then, with a given delay, a trigger pulse initiates firing of the laser. The fluorescence light arriving at the PMT is recorded via a boxcar integrator (Stanford Research Systems SR 250). Its gate width and timing are determined via triggering by a photodiode which monitors a reflex of the laser pulse. The output of the boxcar integrator is fed into an analog-to-digital converter (Stanford Research Systems SR 245) to achieve digitized signal transfer to the data acquisition computer.

Pulsed lasers used for this study were a Nd:YAG (Spectron Laser Systems SL803) pumped dye laser (Lambda Physik Scanmate 2E) operated at 20 Hz with a line width of about 0.2 cm^{-1} and a pulse length of 8 ns as well as a XeCl excimer laser (Lambda Physik LEXtra 100) pumped dye laser (Lambda Physik LPD 3002) operated at 50 Hz with a line width of about 0.2 cm^{-1} and a pulse length of 10 ns.

The frequency shifts between fluorescence excitation spectra taken with the pulsed machine and those taken with the continuous machine were calibrated by comparison with the high precision wavemeter of the continuous wave dye laser.

4.3 Chemicals

Chloroaluminiumphthalocyanine (degree of purity 99 %) was purchased from Acros Organics. Free-base phthalocyanine (degree of purity 98 %), 2,9,16,23-tetra-*tert*-butylphthalocyanine (degree of purity 97 %) and 5,10,15,20-tetraphenylporphyrin (degree of purity 95 % with $< 0.1 \%$ of corresponding chlorin) were purchased from Sigma-Aldrich. 5,10,15,20-tetraphenylchlorin (degree of purity 95 %) was purchased from Porphyrin Systems. The other porphyrins (free-base porphyrin, 5,15-diphenylporphyrin, 5,10,15,20-tetramethylporphyrin, 5,10,15,20-tetrapropylporphyrin and etioporphyrin I) were purchased from Frontier Scientific and should have a degree of purity $> 97 \%$.

All chemicals were used as purchased without further purification. High pressure liquid chromatography (HPLC) analyses were performed on free-base porphyrin, 5,15-diphenylporphyrin, 5,10,15,20-tetraphenylchlorin, 5,10,15,20-tetraphenylporphyrin, 5,10,15,20-tetramethylporphyrin, 5,10,15,20-tetrapropylporphyrin and etioporphyrin I to check for impurities [74]. The results of these analyses are presented in the appendix at the end of this work and will be discussed where necessary in the respective sections of chapter 6 and 7.

5 Reflected helium droplet beam

In the course of replacing the formerly used liquid helium flow-through cryostat of our continuous helium droplet source with a closed-cycle cryostat, the whole nozzle-cryostat assembly had to be removed and rebuilt. Due to the new dimensions, the nozzle unit had to be realigned to the geometrical axis of the machine. As the mass-spectrometer was not available at this point of time, the integrated fluorescence of free-base phthalocyanine doped into the helium droplets was used to achieve optimum adjustment. The coordinate system addressed in the following discussion is the same as for figure 4.1 in chapter 4.1.1 with the droplet beam axis being the x-axis while the laser beam defines the z-axis (cf. figure 5.1). During the replacement procedure mainly the positioning along the z-axis, parallel to the plane of detection, was varied while the y-axis was initially kept close to the optimum position. Furthermore, the positioning along the x-axis, i.e. the distance between nozzle and skimmer, was known to be relatively uncritical.

While moving the nozzle up and down in direction of the z-axis, three maxima of the integrated fluorescence of free-base phthalocyanine could be observed whereby the first and the third maximum (called **(2)** in the following) showed the same fluorescence signal intensity which was significantly lower than for the second one (called **(1)** in the following). The positions of the nozzle for case **(2)** were at equal distances (7.5 mm) above and below the position for case **(1)**. The different nozzle positions for case **(1)** and **(2)** are illustrated schematically in figure 5.1.

The expansion conditions to gain maximum fluorescence signal of singly doped droplets differed for case **(1)** and **(2)**. Namely, a lower system temperature T_0 was

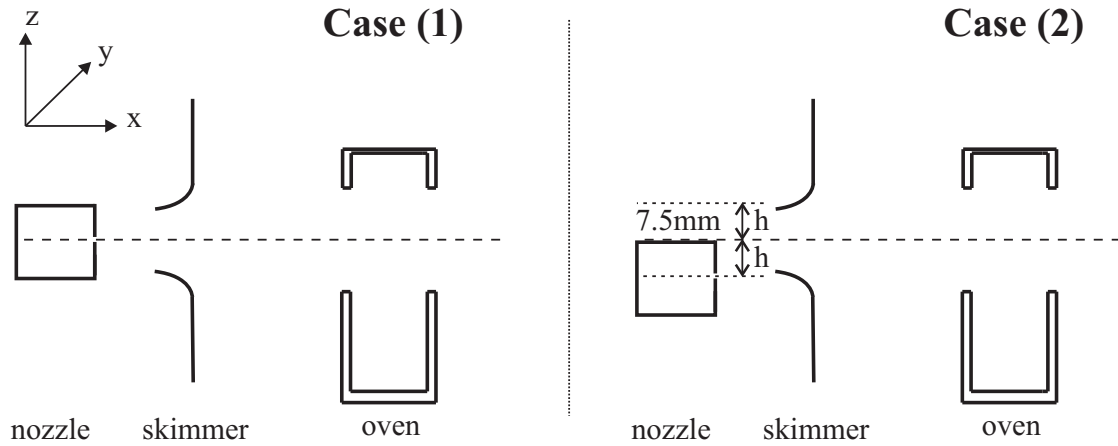


Fig. 5.1: Schematic drawing of the experimental setup illustrating the phenomenon of three maxima for the fluorescence signal of free-base phthalocyanine. Note that this illustration is not to scale.

necessary for case (2) compared to the maximum of integrated fluorescence in case (1) while the stagnation pressure p_0 stayed constant for both cases. This observation is equivalent to a generation of larger helium droplets in case (2) (cf. chapter 2.1).

For the present study fluorescence excitation spectra were recorded with the continuous helium droplet machine using the continuous wave dye laser (Coherent Innova 899-29 autoscan) operated with DCM yielding an average power of 160 mW (measured directly behind the laser). A color glass filter RG695 (Schott) in front of the PMT was used to eliminate laser stray light. The heating voltage of the pick-up cell optimized for single doping of the droplets was 13.5 V corresponding to an oven temperature of approx. 350 °C. The stagnation pressure was $p_0 = 20$ bar.

5.1 ZPL asymmetry and droplet size

As has been observed before, the asymmetry of the ZPL of free-base phthalocyanine as well as the spectral position of the ZPL varied upon changing the expansion conditions [59]. A variation of the line shape with experimental parameters that affect the droplet size distribution indicates an inhomogeneous origin of the observed

line shape. The asymmetry of the ZPL of free-base phthalocyanine with a steep rise on the red side and a tail extending to the blue side is interpreted in terms of a distribution of transition frequencies of the dopant which depend on the droplet size. Generally, the red shift of a resonance frequency originates from long-range dispersive interactions which are the dominating interactions in clusters of rare gas atoms [57]. This, together with the fact that a larger number of rare gas atoms leads to a larger spectral red shift until the frequency shift converges to the upper limit of bulk helium, is the connection between asymmetric line shape and the helium droplet size distribution.

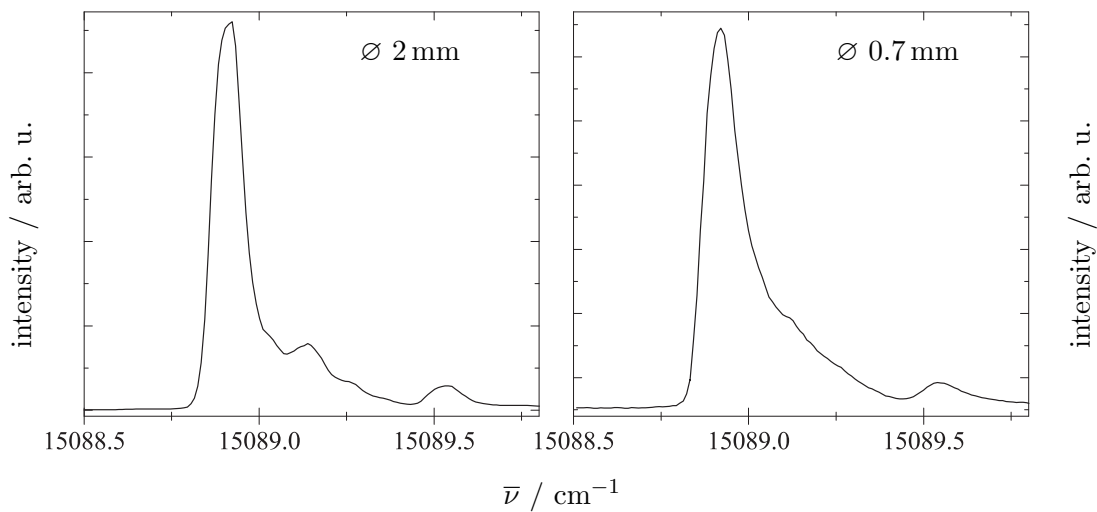


Fig. 5.2: Left panel: ZPL of free-base phthalocyanine recorded using the 2 mm skimmer and the closed-cycle cryostat. Right panel: ZPL of free-base phthalocyanine recorded using the 0.7 mm skimmer and the flow-through cryostat.

Since not only the helium cryostat was replaced but, in a preceding step, also a new skimmer with an opening diameter of 2 mm instead of the formerly used 0.7 mm was mounted, the line shape of the ZPL of free-base phthalocyanine revealed additional fine structures on the blue side when recorded with the new experimental setup. This is exemplarily shown in figure 5.2 where the left panel displays the ZPL of free-base phthalocyanine recorded using the 2 mm skimmer and the closed-cycle cryostat while the right panel displays the ZPL recorded using the 0.7 mm skimmer

and the flow-through cryostat. At this, one should note that for measurements of free-base phthalocyanine using the 2 mm skimmer and the flow-through cryostat the spectral fine structure is identical to that displayed in the left panel of figure 5.2.

Due to the altered line shape in consequence of replacing the skimmer, it was unfortunately not possible to quantitatively simulate the inhomogeneous line shape of the ZPL of free-base phthalocyanine by convolution of a homogeneous with an inhomogeneous contribution taking account of the droplet size distribution as has been demonstrated before [48, 59]. Instead, a qualitative estimation based on the droplet size analysis from reference [40] is given for the mean droplet sizes resulting from a stagnation pressure of $p_0 = 20$ bar and varying system temperatures.

In the following, section 5.2 firstly presents the analyses of mean droplet sizes for the above mentioned data sets for case (1) and (2). Finally, an interpretation of the results for case (2) in terms of a reflected helium droplet beam is suggested (see section 5.3).

5.2 Determination of mean droplet sizes

Since the modification of our nozzle cryostat unit also involved a new placement of the temperature sensor, the reading of temperatures for maximum fluorescence signal of free-base phthalocyanine deviated by approximately 2 K from the formerly derived values with the flow-through cryostat. For example, with $p_0 = 20$ bar an optimum system temperature $T_{0,ft} = 10.5$ K was found using the flow-through cryostat whereas $T_{0,cc} = 12.5$ K was determined using the closed-cycle cryostat. This was considered in the following when determining mean droplet sizes by comparison with the data from reference [40]. The experimental setup used in this reference was essentially the same as our formerly used nozzle-cryostat unit including components, dimensions and, as well, the placement of the temperature sensor. Therefore, comparison of the mean droplet sizes from reference [40] with the data derived in our lab seems reasonable. Since data from reference [40] cover only the temperature range

from 11 K up to 17 K, mean droplet sizes for lower temperatures are estimated from data presented in reference [21].

Producing a certain mean droplet size in order to gain maximum fluorescence signal of singly doped droplets while keeping the particle density in the pick-up cell fixed as well as the stagnation pressure, one has to consider that, on the one hand, the helium droplets need to have a certain minimum size to provide enough helium atoms to incorporate the phthalocyanine molecule and in addition helium atoms that evaporate subsequently after the pick-up process to cool down the guest molecule (cf. chapter 2.2). On the other hand, droplets that exceed a certain size enable multiple doping which obviously reduces the fluorescence signal of single free-base phthalocyanine molecules inside helium droplets. Moreover, considering the range of suitable droplet sizes for single molecule doping one has to take into account that, since the overall flux of helium remains almost constant for a fixed stagnation pressure, variation of the mean droplet size also affects the number of produced helium droplets i.e. creating less but larger droplets at lower temperatures and, accordingly, more but smaller helium droplets at higher temperatures. Carefully balancing the mentioned effects, finally leads to an optimum setting of the system temperature for a preset stagnation pressure and oven temperature.

5.2.1 Case (1)

The following measurements were recorded with the nozzle opening on axis with the opening of the skimmer and the openings of the pick-up cell (cf. figure 5.1).

Fluorescence excitation spectra of the ZPL of free-base phthalocyanine for different system temperatures $T_{0,cc}$ and a constant stagnation pressure $p_0 = 20$ bar are displayed in figure 5.3. All spectra are scaled to the respective peak intensity. Together with the temperature reading $T_{0,cc}$ and the corrected temperature $T_{0,ft}$ the corresponding mean droplet sizes \bar{N} prior to pick-up for every spectrum depicted in figure 5.3 are given in table 5.1 along with the intensities I of the fluorescence signal relative to the maximum signal recorded for $T_{0,cc} = 12.5$ K. It should be no-

ted that the escalating mean droplet sizes between $T_{0,cc} = 12.0$ K and $T_{0,cc} = 11.5$ K are due to a transition from subcritical to supercritical expansion conditions, i.e. producing helium droplets via condensation of gaseous helium and accordingly via fragmentation of the liquid phase (cf. chapter 2.1).

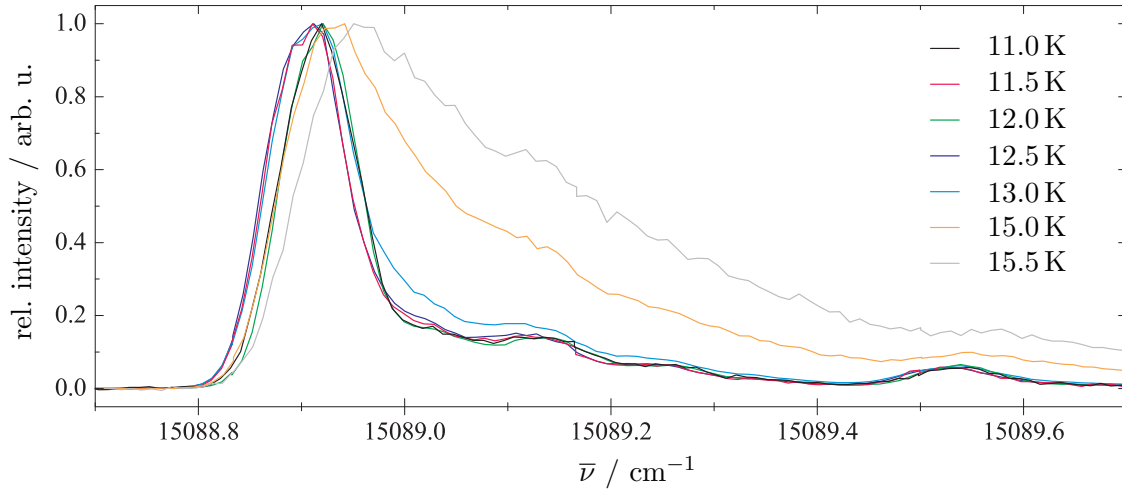


Fig. 5.3: Fluorescence excitation spectra of the ZPL of free-base phthalocyanine for a constant stagnation pressure of $p_0 = 20$ bar and different system temperatures $T_{0,cc}$ of the continuous nozzle as indicated in the panel. All spectra are scaled to the respective peak intensity.

Starting from the lowest temperature $T_{0,cc} = 11.0$ K, the signal intensity increases with increasing $T_{0,cc}$ until the maximum fluorescence signal is reached for $T_{0,cc} = 12.5$ K. The latter corresponds to an initial mean droplet size of $\bar{N} \approx 18000$ atoms (cf. table 5.1). Since the pick-up procedure leads to an approximate loss of 3000 helium atoms [48], the mean droplet size of the finally probed droplets can be estimated to about 15000 atoms.

Within the range of $T_{0,cc} = 11.0 - 12.5$ K, apart from the amplitude, no significant alteration of the ZPL neither regarding line shape nor spectral position is observable. This means that, within the mentioned temperature interval, single molecule doping involves the same fraction of the respective initially generated droplet size distribution. Though, for higher temperatures, $T_{0,cc} \geq 13.0$ K, the ZPL of free-base

Tab. 5.1: List of system temperatures $T_{0,cc}$ of the closed-cycle nozzle-cryostat unit at a constant stagnation pressure of $p_0 = 20$ bar. Also given are the corresponding values $T_{0,ft}$ for the flow-through nozzle-cryostat unit which were calculated using $T_{0,ft} = T_{0,cc} - 2$. The third column lists the corresponding mean droplet sizes \bar{N} prior to pick-up. I gives the fluorescence signal intensity in percent relative to the maximum signal recorded for $T_{0,cc} = 12.5$ K.

$T_{0,cc} / \text{K}$	$T_{0,ft} / \text{K}$	\bar{N}	$I / \%$
11.0	9.0	2000000 ^a	0.9
11.5	9.5	400000 ^a	1.3
12.0	10.0	20000 ^a	36.0
12.5	10.5	18000 ^a	100.0
13.0	11.0	15363 ^b	59.0
15.0	13.0	7987 ^b	3.2
15.5	13.5	6000 ^a	0.7

^aEstimated from data presented in ref. [21].

^bData taken from ref. [40].

phthalocyanine begins to broaden. This phenomenon along with a blue shift of the line maximum is exemplarily shown in figure 5.3 for $T_{0,cc} = 15.0$ K and $T_{0,cc} = 15.5$ K. Combined with the corresponding mean droplet sizes (cf. table 5.1) this observation fits to the interpretation of a spectral blue shift in terms of smaller clusters surrounding the fluorescing molecule [57]. However, the frequency shift is not linearly dependent on the droplet size. This can easily be deduced from the spectra given in figure 5.3 for $11.0 \leq T_{0,cc} \leq 13.0$ K since the droplet sizes for the given temperature range vary between about 15400 and 2000000 helium atoms (cf. table 5.1) while the spectral position of the ZPL maximum remains constant.

5.2.2 Case (2)

The measurements described in the following were recorded with the nozzle opening displaced vertically, along the z-axis, by 7.5 mm above (or below) the geometrical axis of the machine given by the skimmer and the apertures of the pick-up cell (cf. figure 5.1).

Fluorescence excitation spectra of the ZPL of free-base phthalocyanine for different system temperatures $T_{0,cc}$ and a constant stagnation pressure $p_0 = 20$ bar are displayed in figure 5.4. Contrary to case (1), maximum fluorescence signal is gained for $T_{0,cc} = 11.0$ K while the fluorescence signal has already almost disappeared at $T_{0,cc} = 12.0$ K. One should note that the signal level of the data sets depicted in figure 5.4 is significantly lower than for those in figure 5.3 as can be seen from the respective signal-to-noise ratio. The peak intensity for $T_{0,cc} = 11.0$ K, for example, is only 0.6 % compared to $T_{0,cc} = 12.5$ K for case (1) although it reaches 75.6 % compared to $T_{0,cc} = 11.0$ K for case (1). Considering the spectral shape of the ZPL recorded for case (1) and (2) at $T_{0,cc} = 11.0$ K, the close similarity indicates equivalent conditions for both cases.

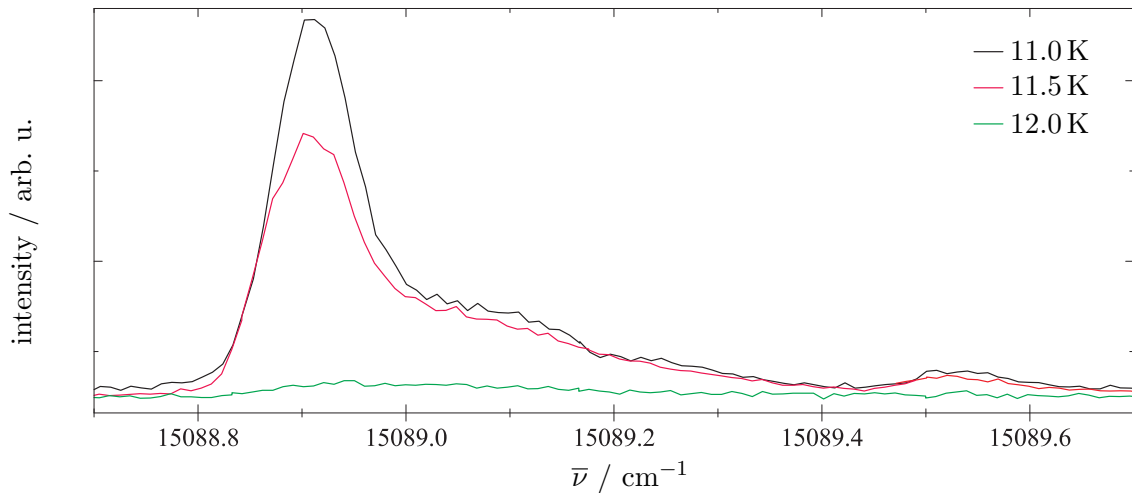


Fig. 5.4: Fluorescence excitation spectra of the ZPL of free-base phthalocyanine for a constant stagnation pressure of $p_0 = 20$ bar and different system temperatures $T_{0,cc}$ of the continuous nozzle as indicated in the panel.

The corresponding initially produced mean droplet sizes \bar{N} for every spectrum depicted in figure 5.4 are as a matter of course the same as in case **(1)** (cf. table 5.1). Thus, considering the mean droplet sizes given in table 5.1, maximum fluorescence signal is gained for an initial mean droplet size of $\bar{N} \approx 2000000$ atoms. This value is by two orders of magnitude larger than the previously estimated mean droplet size of 18000 atoms derived in case **(1)** for optimum fluorescence signal (cf. section 5.2.1 table 5.1).

5.3 Interpretation of case **(2)** as reflected beam

To explain the significantly larger mean droplet sizes to gain maximum fluorescence signal in case **(2)** (cf. section 5.2.2), we look at the reflection of the droplet beam. Such a reflection of superfluid helium droplets has been observed before by intentionally directing a helium droplet beam onto a polished stainless steel target [75]. In our case, the reflected beam is imagined as originating from one portion of the initially produced spatial distribution of helium droplets that hits the conically shaped skimmer and is subsequently reflected into the beam axis defined by the openings of the skimmer and the pick-up cell. Thus, we assume that a certain fraction of the initially produced helium clusters survives the collision with the skimmer surface at a helium droplet beam velocity of about 260 m/s [19] and results in droplet sizes that are still large enough to host one phthalocyanine molecule.

5.3.1 Geometric examination

A geometric view of the reflected droplet beam is given in figure 5.5. The top part of figure 5.5, labeled as **a)**, shows the entire experimental setup relevant for the path of the droplet beam. Exemplary droplet trajectories for reflection at the skimmer surface close to the orifice in the limiting cases of the largest and smallest possible reflection angle γ_{max} and γ_{min} , respectively, are marked by dashed blue lines. The bottom part, labeled as **b)**, depicts an enlarged view of the skimmer close to its

displacement d of doped droplets from the ideal droplet beam axis at the position of the laser beam is 5 mm if the droplets should contribute to the recorded integrated fluorescence signal. For case **(1)** the angle for the maximum possible beam cone is 1.4° .

In case **(2)** the maximum beam cone is restricted by γ_{max} which in turn depends on the incident angle γ_{inc} of the droplet beam on the skimmer surface which is calculated by $\gamma_{inc} = \alpha - \beta$ where α is the angle between incident beam and geometrical axis of the machine and β is the angle between geometrical axis of the machine and a tangent line to the skimmer curvature close to the orifice (cf. bottom panel of figure 5.5). $\alpha = 25.3^\circ$ can be deduced from the height h of the nozzle compared to the regular droplet beam axis (7.5 mm) plus the radius r_s of the skimmer (1 mm) and the distance between nozzle and skimmer ns (18 mm) by first calculating $\tan(\alpha) = \frac{h+r_s}{ns}$. Thus, if the droplet beam hits the skimmer very close to the orifice, the incident angle of the droplet beam on the skimmer surface is $\gamma_{inc} = 12.8^\circ$. Assuming specular reflection, i.e. that the angle of the reflected droplet beam equals the incident angle, the droplets are obviously reflected close to parallel (with an angle of 0.3°) to the geometrical axis of the machine. Consequently, $\gamma_{max} = 12.8^\circ$ as well while γ_{min} is derived by first calculating $\tan(\gamma) = \frac{p-r_s}{s+so+o_r}$ where p is the radius of the oven apertures (2 mm), s is the length of the skimmer (25.4 mm), so the distance between skimmer and oven (75 mm) and o_r the inner radius of the oven (10 mm). The minimum angle γ between the emergent beam that can still pass the second oven aperture and the geometrical axis of the machine is therefore 0.5° . This finally results in $\gamma_{min} = \beta - \gamma = 12.0^\circ$ and gives a maximum beam cone of $\gamma_{max} - \gamma_{min} = 0.8^\circ$ for case **(2)**. However, the calculations given above have to be considered as rough estimations since deviations of dimensions within the magnitude of one millimeter would significantly change the derived angles.

5.3.2 Examination of peak intensities

Generally, information on droplet size distributions and accordingly intensity distributions is only available for the beam center. Since case (2) involves a fraction of the droplet beam that is $\sim 25^\circ$ outside the regular droplet beam center, one can assume that, in analogy to supersonic jet expansions where temperatures in the outer parts of the beam are higher, the droplet size distribution in this spatial region comprises smaller droplet sizes than in the center of the droplet beam. While angular intensity distributions for effusive beams are described by a $\cos(\alpha)$ relation (cf. for example [76]), in the case of supersonic jet expansions a sharper distribution is expected like e.g. a $\cos^2(\alpha)$ relation. Thus, calculating peak intensities for $T_{0,cc} = 11.0$ K for $\alpha = 25^\circ$, expected intensities for case (2) would be 91 % ($\cos(\alpha)$) or 82 % ($\cos^2(\alpha)$) of the intensity observed in case (1). However, the observed peak intensity for $T_{0,cc} = 11.0$ K in case (2) was 75.6 % (cf. section 5.2.2 and figure 5.6). Assuming an even sharper $\cos^3(\alpha)$ relation for the droplet beam provides 74 % which approximately corresponds to the experimental value. But, for $T_{0,cc} = 11.5$ K in case (2) a signal reduction to 36.1 % of the level recorded for case (1) is observed. This larger decrease in the peak intensity can be explained by the loss of helium atoms due to inelastic collision of the initially generated droplets with the skimmer surface which finally leads to significantly shrunk droplets. At this, droplets that initially comprise about 400000 atoms (cf. table 5.1) are expected to result in a smaller number of droplets that are finally suitable for single doping than what can be expected for fragmented droplets initially consisting of about 2000000 atoms (cf. table 5.1).

Fluorescence excitation spectra with similar signal level recorded for case (1) and (2) are juxtaposed in figure 5.6. The blue graph shows the spectrum recorded for case (2) with $T_{0,cc} = 11.0$ K, the system temperature at which maximum fluorescence signal was observed. For comparison, the spectra of case (1) at $T_{0,cc} = 11.0$ K (black) and $T_{0,cc} = 15.5$ K (red) with similar peak intensity are depicted as well. Although all spectra exhibit approximately similar peak intensity, the ZPL for case (1) $T_{0,cc} = 15.5$ K is clearly broadened (for an explanation see section 5.2.1). Com-

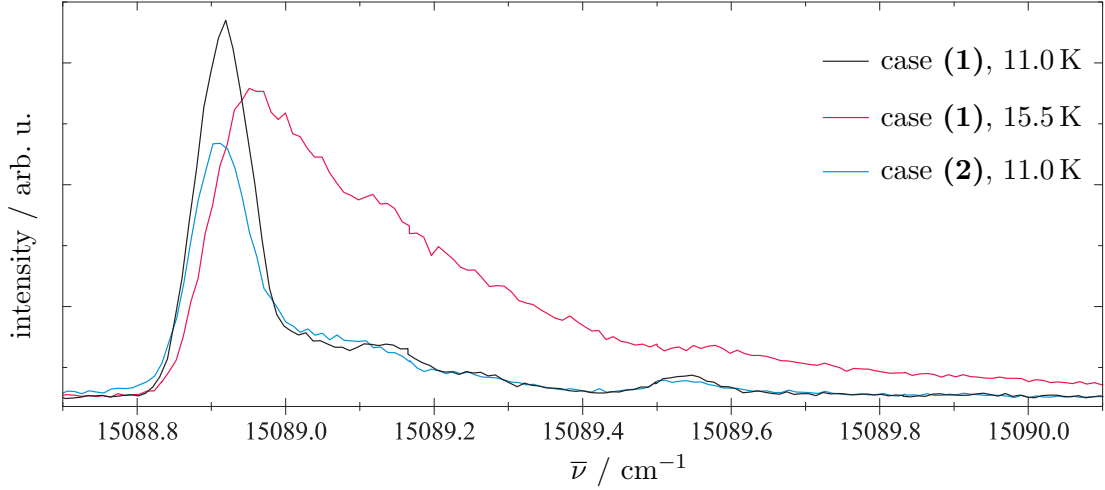


Fig. 5.6: Fluorescence excitation spectra of the ZPL of free-base phthalocyanine for case **(1)** (black, red) and **(2)** (blue) at a constant stagnation pressure of $p_0 = 20$ bar. System temperatures $T_{0,cc}$ are given for each spectrum. The blue spectrum illustrates the maximum fluorescence signal level recorded in case **(2)** while the spectra for case **(1)** are those with comparable signal level to the blue spectrum.

pared to the optimum signal for case **(1)** \bar{N} is either too large (for $T_{0,cc} = 11.0$ K) or too small (for $T_{0,cc} = 15.5$ K) to allow for the absolute maximum of singly doped droplets (cf. introduction of section 5.2). Considering the similar line shapes observed for $T_{0,cc} = 11.0$ K in case **(1)** and **(2)**, the droplet sizes which finally contribute to the fluorescence signal of single phthalocyanine molecules are obviously in a regime that has no effect on the frequency shift of the molecular dopant. Together with the observation that almost no fluorescence signal is recorded in case **(2)** for $T_{0,cc} = 12.0$ K (cf. figure 5.4), equivalent with an initial mean droplet size of about 20000 atoms (cf. table 5.1), one can finally conclude that initially generated droplets are reduced by more than 50% of their size via collision with the skimmer surface.

6 Phthalocyanine species

Phthalocyanines are aromatic compounds in which four benzopyrrole units are connected via nitrogen (aza) bridges (cf. compound 1 in figure 6.1).

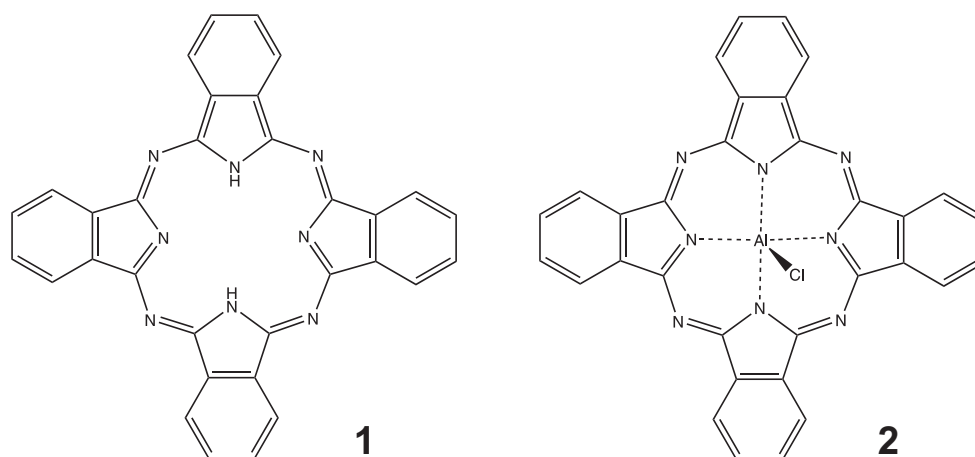


Fig. 6.1: Chemical structure of free-base phthalocyanine (1) and chloroaluminiumphthalocyanine (2).

This class of chromophores comes with intense absorption in the visible region as well as high chemical and thermal stability. The endocyclic hydrogen atoms of the macrocycle are easily substituted by various metal atoms to form stable complexes (see for example ref. [77] and references therein).

The various applications of phthalocyanines range from their use as dyes, photosensitizers in photodynamic therapy (see for example references [78, 79, 80]), electrode material in fuel cells (see for example references [81, 82]), red emitters in OLEDs (organic light emitting device) (see for example ref. [83]) and optical limiting devices

(see for example [84] and references therein) to photoconductors in laser printers (see for example ref. [85]).

Phthalocyanines can be considered as synthetical model systems of the biologically relevant porphyrins (see chapter 7) because of their structural similarities (cf. figures 6.1 and 7.1). Since they exhibit satisfactorily high fluorescence quantum yields (e.g. for free-base phthalocyanine $\Phi_f=0.7$ [86]), phthalocyanines are excellent spectroscopic probes.

At present, fluorescence excitation as well as dispersed emission spectra of free-base phthalocyanine in supersonic jet experiments as well as in helium nanodroplets are published [87, 88, 89, 90]. Moreover, excitation spectra of chloroaluminiumphthalocyanine, Mg-phthalocyanine and Zn-phthalocyanine in supersonic jet experiments and helium droplets have been recorded while for Mg-phthalocyanine also dispersed emission spectra were measured in the helium droplet experiment [8, 27, 52, 91, 92]. Furthermore, by using helium nanodroplet spectroscopy, fluorescence excitation spectra of chlorogalliumphthalocyanine and hydroxyaluminiumphthalocyanine were taken [92, 93].

6.1 Chloroaluminiumphthalocyanine (AlClPc)

Chloroaluminiumphthalocyanine (AlClPc) is a phthalocyanine derivative where the endocyclic hydrogen atoms are substituted by a metal atom, namely aluminium. Moreover, the aluminium atom coordinates a chlorine atom as additional ligand. The structural formula is depicted in figure 6.1 (compound 2). AlClPc belongs to the point group C_{4v} and, due to the Al-Cl-bond, possesses a permanent dipole moment of about 4 debye [92]. In contrast to the planar macrocycle of free-base phthalocyanine AlClPc is, according to experimental results and quantum chemical calculations [94], assumed to be distorted from planarity in the electronic ground state while the aluminium atom is displaced from the center of the macrocycle towards its axial chlorine ligand. The isoindole groups of the chromophore are believed to form a bowl tilted away from the Al-Cl group [91] resulting in a molecular structure like an inverted umbrella.

Fluorescence excitation of AlClPc has been investigated in Shpol'skii matrices [95] and, as already mentioned in the introduction to chapter 6, also in supersonic jet experiments [91] and superfluid helium droplets [92].

For the present study fluorescence excitation and dispersed emission spectra were recorded with the continuous helium droplet machine using the continuous wave dye laser (Coherent Innova 899-29 autoscan) operated with DCM yielding an average power of 200 mW (measured directly behind the laser). A color glass filter RG695 (Schott) in front of the PMT was used to eliminate laser stray light. The heating voltage of the pick-up cell optimized for single doping of the droplets was 14.0 V corresponding to an oven temperature of approx. 390 °C. The expansion parameters were $p_0 = 20$ bar and $T_0 = 10.5$ K. To record the dispersed emission spectra of the AlClPc-Ar₁ complexes and for excitation at the various signals at the electronic origin of AlClPc the spectrograph was equipped with an 2400 lines/mm grating instead of the 1200 lines/mm grating which is used by default. Therefore, according to [52] an absolute accuracy in the determination of the wavenumbers of 0.3 cm⁻¹ can be achieved.

6.1.1 Fluorescence excitation of AlClPc

The fluorescence excitation spectrum of AlClPc is depicted in figure 6.2. The inset shows the spectral region of the vibrational modes magnified by a factor of 10. Sharp lines are present throughout the entire spectrum.

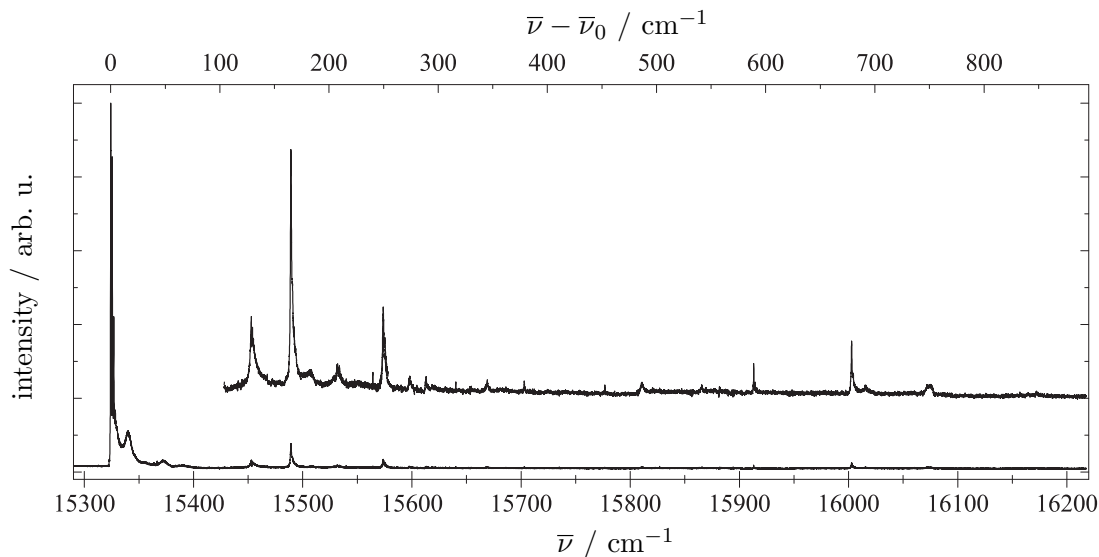


Fig. 6.2: Fluorescence excitation spectrum of AlClPc normalized to the electronic origin at $\bar{\nu}_0 = 15324.1 \text{ cm}^{-1}$. The inset shows the spectral region of the vibrational transitions magnified by a factor of 10.

A list of all transitions $\bar{\nu}$ observed in the fluorescence excitation spectrum is given in table 6.1. The line positions $\bar{\nu}_{rel} = \bar{\nu} - \bar{\nu}_0$ relative to the most intense fluorescence signal at $\bar{\nu}_0 = 15324.1 \text{ cm}^{-1}$ which is assigned to the electronic origin are compared to the respective values derived from the previously conducted helium droplet measurement ($\bar{\nu}_{dr}$) [92] as well as the supersonic jet experiment ($\bar{\nu}_{jet}$) [91]. Regarding the two data sets obtained from droplet experiments, they are in good accordance with each other. Although, the weak mode at $\bar{\nu}_{rel} = 124.2 \text{ cm}^{-1}$ was not observed in the experiment described in reference [92]. This is presumably by virtue of the significantly lower signal-to-noise ratio in that experiment. In general, one can state that apart from a solvent shift of $49 \pm 5 \text{ cm}^{-1}$ to the red by switching from the isolated molecule to the superfluid helium matrix, good agreement can be

found for the vibrational mode pattern of the electronically excited state taking into account the different accuracies in determining the laser wavelength (cf. table 6.1). This finding indicates minor disturbance effects caused by the matrix environment. Within the spectral range covered by the gas phase experiment (cf. ref. [91]), exceptions are only the three weak modes at $\bar{\nu}_{rel} = 183.0 \text{ cm}^{-1}$, $\bar{\nu}_{rel} = 207.6 \text{ cm}^{-1}$ and $\bar{\nu}_{rel} = 273.8 \text{ cm}^{-1}$ which were not reported for the supersonic jet measurement. At this, the mode at $\bar{\nu}_{rel} = 207.6 \text{ cm}^{-1}$ also shows a triple structure comparable to the electronic origin of AlClPc while a spectral fine structure for the other two modes can not be determined due to their rather low intensity. Therefore the three signals may either not be visible in the supersonic jet experiment due to the lower signal-to-noise ratio (cf. ref. [91]) or two of the signals may stem from complexes of AlClPc with residual gas molecules.

For some vibrational modes a Lorentzian fit was possible. In those cases the life times τ which are also listed in table 6.1 were calculated from the Lorentzian line widths $\Delta\bar{\nu}_L$ by using $\tau = \frac{1}{2\pi c\Delta\bar{\nu}_L}$. The resulting data indicate that the life times of the vibrational transitions increase with increasing excitation energy.

The fine structure of the electronic origin of AlClPc at $\bar{\nu}_0 = 15324.1 \text{ cm}^{-1}$ is depicted in the top panel of figure 6.3. A triple structure is observed with three major signals of which each is accompanied by a weaker one. As is exemplarily shown in figure 6.3 for four vibrational modes, the spectral fine structure of the electronic origin (top panel) recurs with differing line widths in the vibronic transitions (bottom panels). Wavenumber axes are relative to the most intense signal of the corresponding transition. The spectral positions $\bar{\nu}_{rel,0}$ of the vibrational modes relative to the electronic origin at $\bar{\nu}_0 = 15324.1 \text{ cm}^{-1}$ are given in each panel.

In summary, the fluorescence excitation spectrum of AlClPc exhibiting sharp lines, a solvent shift within the order of magnitude as observed before for other organic molecules (cf. for example ref. [21]) and almost no shift of the vibrational transitions with regard to the isolated molecules seems quite undisturbed by the superfluid helium environment.

Tab. 6.1: List of vibronic transitions obtained from the fluorescence excitation spectrum of AlClPc in superfluid helium droplets. Absolute line positions $\bar{\nu}$ could be determined with an accuracy of 0.05 cm^{-1} . $\bar{\nu}_{rel}$ indicates the frequency shift relative to the electronic origin at $\bar{\nu}_0 = 15324.1 \text{ cm}^{-1}$. $\Delta\bar{\nu}_L$ are the respective Lorentzian line widths. τ gives the resulting life times. $\bar{\nu}_{dr}$ are the values available for $\bar{\nu}_{rel}$ from reference [92] measured in helium droplets while $\bar{\nu}_{jet}$ are the corresponding data from reference [91] recorded in a supersonic jet. The last column gives the shift between the vibrational energies deduced from the helium droplet experiment relative to the supersonic jet measurements. Unless otherwise noted, all data are given in cm^{-1} .

$\bar{\nu}$	$\bar{\nu}_{rel}$	$\Delta\bar{\nu}_L$	τ / ps	$\bar{\nu}_{dr}$ ^a	$\bar{\nu}_{jet}$ ^b	$\bar{\nu}_{shift}$
15324.1	0	-	-	0	0	0
15339.9	15.8	-	-	16	16	0
15448.3	124.2	3.03(9)	1.75	-	126	-2
15489.2	165.1	1.18(2)	4.50	165	165	0
15507.1	183.0	-	-	-	-	-
15531.7	207.6	-	-	-	-	-
15573.8	249.6	1.32(4)	4.02	-	250	0
15598.0	273.8	-	-	-	-	-
15613.2	289.1	-	-	-	290	-1
15669.0	344.9	-	-	-	345	0
15811.0	486.9	-	-	-	489	-2
15913.0	588.9	0.41(2)	12.9	-	592	-3
16002.8	678.7	0.89(3)	16.8	-	-	-
16015.6	691.4	-	-	-	-	-
16071.6	747.5	-	-	-	-	-
16074.6	750.5	-	-	-	-	-

^aData taken from ref. [92].

^bData taken from ref. [91]. Accuracy of the frequencies relative to the electronic origin is $\pm 5 \text{ cm}^{-1}$.

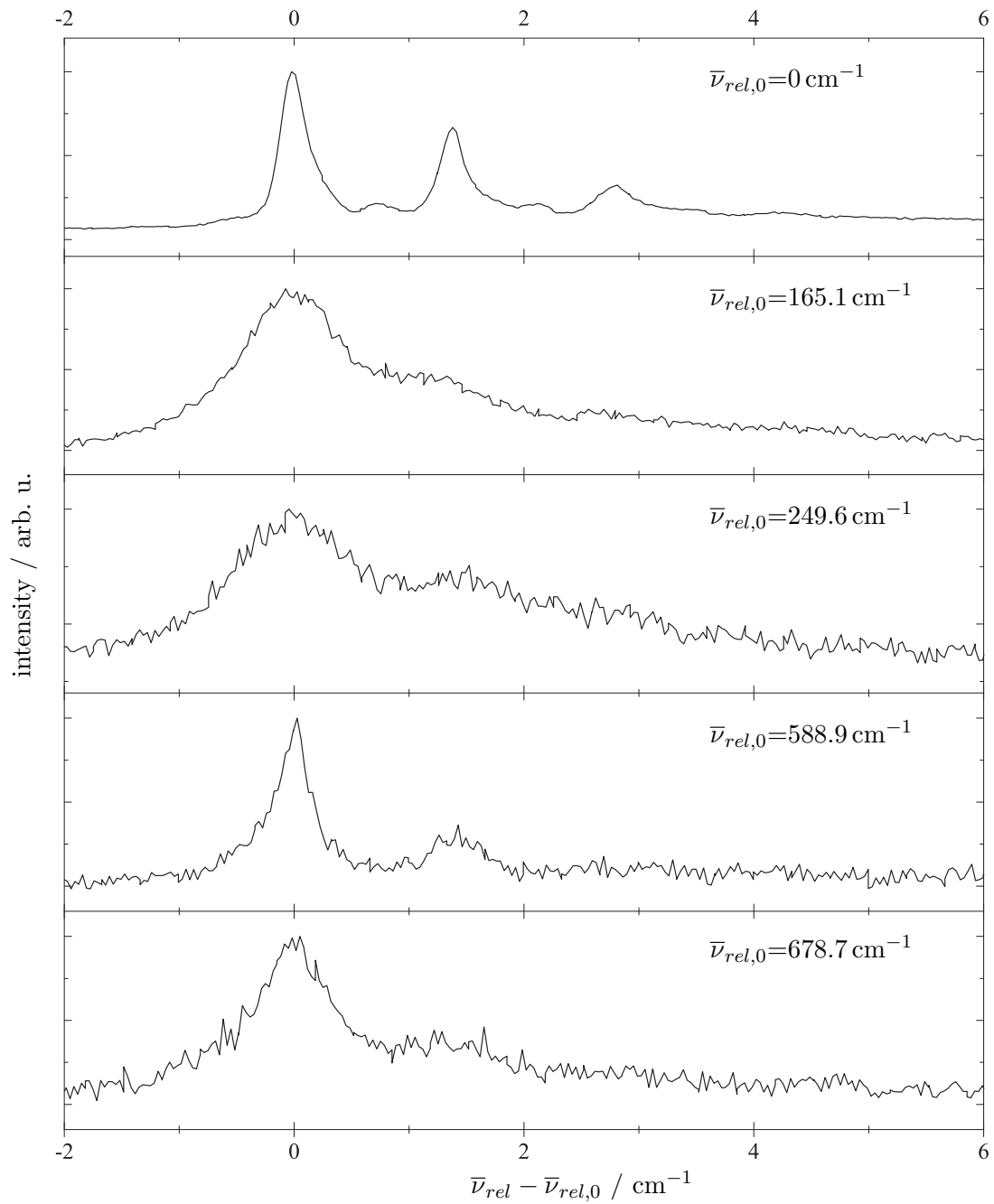


Fig. 6.3: Fine structure of vibronic transitions of AlClPc in helium droplets. The wavenumber axis is relative to the respective transition frequency. Frequencies relative to the electronic origin at $\bar{\nu}_0 = 15324.1 \text{ cm}^{-1}$ are given in each panel.

6.1.2 Dispersed emission of AlClPc

The dispersed emission spectrum of AlClPc recorded upon excitation at the electronic origin at $\bar{\nu}_{exc} = 15324.1 \text{ cm}^{-1}$ is displayed in figure 6.4. The spectrum was corrected for laser stray light at the excitation frequency (cf. chapter 4.1.3.2) and is normalized to the most intense signal at 15315 cm^{-1} . Although AlClPc was excited at the most intense signal of the electronic origin in the fluorescence excitation spectrum, only weak emission occurs at the excitation wavelength while the most intense signal in dispersed emission is found spectrally shifted to the red by 9 cm^{-1} . In general, one can state that sharp transitions are present throughout the dispersed emission spectrum. Moreover, dispersed emission spectra upon excitation at vibrational transitions are, apart from the signal level, identical to those recorded upon excitation at the electronic origin. However, no emission coinciding with the electronic origin of the fluorescence excitation spectrum at 15324.1 cm^{-1} but only red shifted emission at 15315 cm^{-1} was observed upon excitation of vibronic transitions.

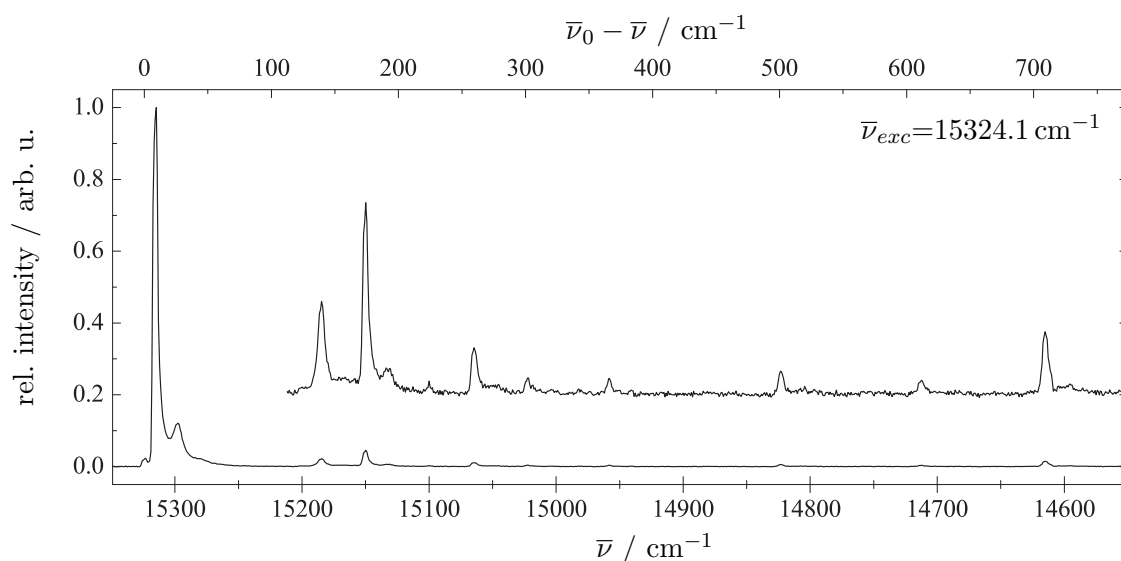


Fig. 6.4: Dispersed emission spectrum of AlClPc for excitation at $\bar{\nu}_{exc} = 15324.1 \text{ cm}^{-1}$. The spectrum is normalized to the most intense signal at 15315 cm^{-1} . The inset shows the spectral region of the vibrational transitions magnified by a factor of 10.

Listing the transitions $\bar{\nu}$ extracted from the dispersed emission spectrum, table 6.2 also compares $\bar{\nu}_{rel}(S_0) = \bar{\nu}_0 - \bar{\nu}$, the frequencies relative to the dominating signal of the emission spectrum at 15315 cm^{-1} which correspond to the vibrational modes of S_0 , with the corresponding values of the electronically excited state $\bar{\nu}_{rel}(S_1^x)$ derived from the fluorescence excitation spectrum. The deviation in percent between the vibrational transitions of S_0 and S_1 , taking $\bar{\nu}_{rel}(S_0)$ as reference value, is tabulated too in the last column. In principle, good agreement is found for the vibrational modes of S_0 and S_1 .

Tab. 6.2: Vibronic transitions $\bar{\nu}$ obtained from the dispersed emission spectrum of AlClPc in superfluid helium droplets by excitation at the electronic origin ($\bar{\nu}_{exc} = 15324.1 \text{ cm}^{-1}$). The frequencies could be determined with an accuracy of 1 cm^{-1} (cf. chapter 4.1.3.2). $\bar{\nu}_{rel}(S_0)$ gives the frequencies relative to the emission origin at $\bar{\nu}_0 = 15315 \text{ cm}^{-1}$ corresponding to the vibrational transitions of the electronic ground state S_0 . For comparison, the vibrational transitions $\bar{\nu}_{rel}(S_1^x)$ of the electronically excited state S_1^x are listed. $\Delta\bar{\nu}_{rel}(S_0 \text{ to } S_1^x)$ is the deviation in percent between the two values taking $\bar{\nu}_{rel}(S_0)$ as reference value.

$\bar{\nu} / \text{cm}^{-1}$	$\bar{\nu}_{rel}(S_0) / \text{cm}^{-1}$	$\bar{\nu}_{rel}(S_1^x) / \text{cm}^{-1}$	$\Delta\bar{\nu}_{rel}(S_0 \text{ to } S_1^x) / \%$
15315	0	0.0	0.0
15298	17	16	-5.9
15185	130	124.2	-4.5
15150	165	165.1	-0.1
15133	182	183.0	+0.5
15065	250	249.6	-0.2
15023	292	289.1	-1.0
14958	357	344.9	-3.4
14823	492	486.9	-1.0
14713	602	588.9	-2.2
14607	708	691.4	-2.3
14530	785	-	-

Emission shifted to the red by $10.3 \pm 0.4 \text{ cm}^{-1}$ and $12.5 \pm 0.4 \text{ cm}^{-1}$ has already been observed for phthalocyanine derivatives, namely free-base phthalocyanine and Mg-phthalocyanine respectively [27, 52, 90, 96]. However, for both molecules two emission spectra were observed. At this, one spectrum coincides with the excitation spectrum while the second spectrum is shifted to the red as mentioned above. Although, the vibrational energies and Franck-Condon factors were identical for both spectra. Upon excitation at the electronic origin, in the case of free-base phthalocyanine, the first emission spectrum clearly dominates over the second while for Mg-phthalocyanine the split spectra occur with an intensity ratio of 1:9 (first to second). Additional vibronic excitation shifts the intensity (even further) in favor to the red shifted emission spectrum. Following these observations for two phthalocyanine derivatives, the double peak of the emission origin of AlClPc is interpreted as the emission spectrum coincident with the excitation and a significantly more intense emission spectrum shifted to the red by 9 cm^{-1} . The intensity ratio without additional vibrational excitation is 1:43 in favor of the red shifted spectrum. Due to the signal-to-noise ratio, the vibronic lines of the first emission spectrum of AlClPc are not identifiable.

As has been discussed previously (see chapter 3.2), the explanation for the split emission spectra of free-base phthalocyanine and Mg-phthalocyanine considering different configurations of the helium solvation shell directly attached to the dopant involves a four level system with a double minimum potential of the helium configuration coordinate for both the S_0 and S_1 state. Since for AlClPc the red shifted emission spectrum is already strongly favored for excitation at the electronic origin of the fluorescence excitation spectrum one can conclude that the relaxation rate for AlClPc is larger than in the case of free-base phthalocyanine.

Carefully investigating the dispersed emission spectra (cf. figure 6.5 right panel) recorded upon excitation at different frequencies within the spectral fine structure of the electronic origin of the fluorescence excitation spectrum (cf. figure 6.5 left panel) revealed that the three prominent transitions indicated by red arrows in the left panel have a common emission spectrum shown as red lines in the right panel

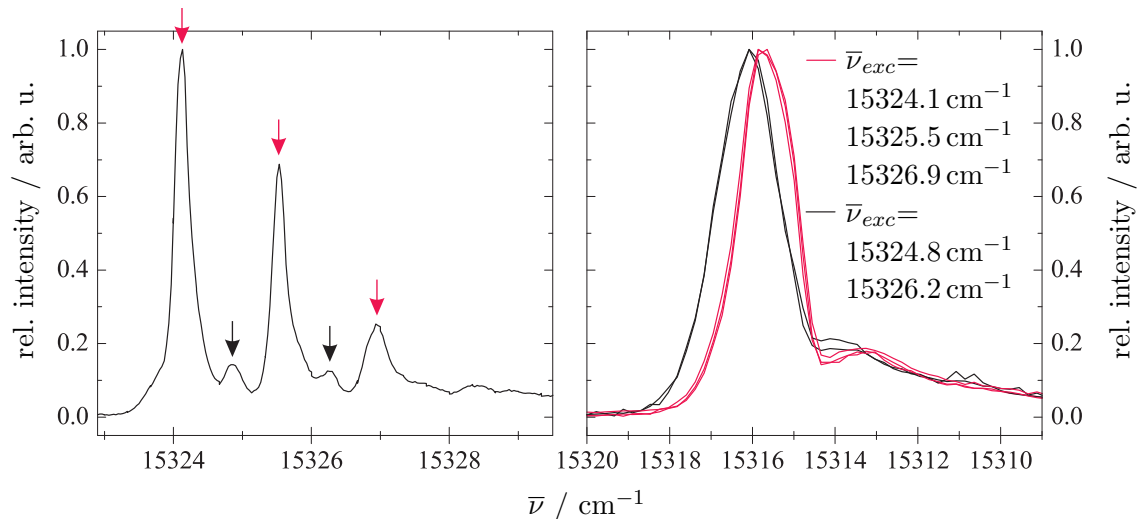


Fig. 6.5: Left panel: Electronic origin of the fluorescence excitation spectrum of AlClPc. Right panel: Dispersed emission spectra resulting from excitation at the frequencies indicated by red and black arrows in the left panel.

while the two tiny peaks marked by black arrows in the left panel show a common emission spectrum shifted to the blue which is shown as black lines in the right panel. Within the limits of the spectral resolution in the emission spectra, the frequency shift of the two systems is identical in excitation and emission and amounts to about 0.8 cm^{-1} . Most likely, the two systems represent isomers of an AlClPc-He_n solvation complex. They differ in the configuration of the helium solvation layer and, therefore, exhibit a different solvent shift. According to the emission spectrum the first of the red marked and the first of the black marked transitions represent the origin in excitation. These findings are another indicator for the extreme sensitivity of electronic spectroscopy on the interaction between dopant and helium environment.

6.1.3 Fine structure in emission spectra of AlClPc-Ar₁ complexes

In order to gain further insight into the interactions between the guest molecule and its immediate surrounding helium solvation layer, van der Waals clusters of AlClPc with argon atoms were investigated pursuing the idea of only causing minor perturbances by replacing a defined number of helium atoms of the solvation shell by another rare gas atom. At this, as has been demonstrated earlier, in the case of heteromolecular clusters the doping order has great influence on the resulting complex configuration [15]. Choosing a pick-up order with first doping the helium droplets with single AlClPc molecules and subsequently with argon (cf. chapter 4.1.1 figure 4.1) warrants for consecutive complexation with single argon atoms which leads to formation of global minimum complex configurations with high probability (cf. ref. [15]). For the inverted pick-up sequence the AlClPc molecule would be attached to the surface of an Ar_n cluster. Argon doping was achieved by use of a gas inlet system fed by argon gas (purity 99.996 %) at which the argon pressure could be tuned by a leak valve.

The fluorescence excitation spectrum of AlClPc without argon (black spectrum) and with argon (red spectrum) is depicted in figure 6.6. The amount of argon was monitored via the current signal of the mass spectrometer at $m/z = 40$ amu which is proportional to the particle density of argon n_{Ar} [12, 52] and is noted in figure 6.6 for the presented spectra. Both spectra are normalized to the signal at the electronic origin of AlClPc at $\bar{\nu}_0 = 15324.1 \text{ cm}^{-1}$. Signals marked by a comb were identified to belong to the complex stoichiometry which is noted above the respective comb. The additional signals resulting from argon doping are presented as sharp lines, however, accompanied by a broad unstructured background signal in the case of AlClPc-Ar₁ complexes. Obviously, the electronic origins of AlClPc-Ar_n complexes are red shifted with respect to the bare molecule. This observation fits to earlier experiments in helium droplets regarding complexes of argon with free-base phthalocyanine, tetracene or pentacene as well as complexes consisting of oxygen and perylene [15,

27, 97, 98]. Consistently with those previous experiments, the spectral red shift of signal groups belonging to a certain number of argon atoms within the van der Waals cluster increases with increasing number of argon atoms.

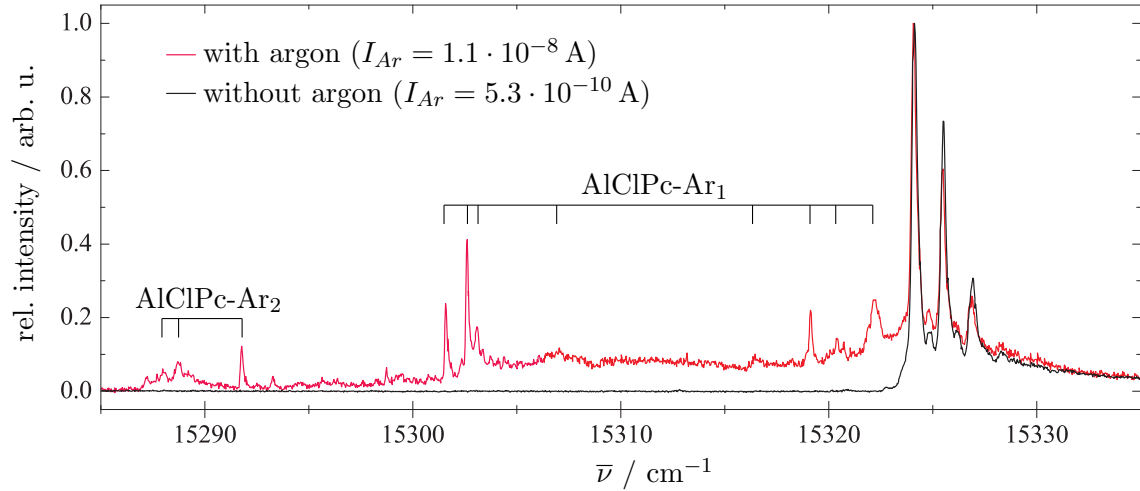


Fig. 6.6: Fluorescence excitation spectra of AlClPc (black) and AlClPc-Ar complexes (red) normalized to the respective signal intensity at the electronic origin of AlClPc at 15324.1 cm^{-1} . The two combs mark fluorescence signals which have been assigned to complexes of AlClPc with one or two argon atoms, respectively.

The assignment of the AlClPc-Ar₁ complex stoichiometry to the respective signals of the fluorescence excitation spectrum was in the case of the sharp lines at $\bar{\nu} = 15301.6 \text{ cm}^{-1}$, $\bar{\nu} = 15302.6 \text{ cm}^{-1}$, $\bar{\nu} = 15303.1 \text{ cm}^{-1}$ and $\bar{\nu} = 15320.4 \text{ cm}^{-1}$ as well as for the AlClPc-Ar₂ complexes conducted by performing a Poisson analysis of the integral signal intensity depending on the particle density of argon n_{Ar} (cf. references [12, 43]). The signals at $\bar{\nu} = 15307.0 \text{ cm}^{-1}$, $\bar{\nu} = 15317.8 \text{ cm}^{-1}$, $\bar{\nu} = 15319.1 \text{ cm}^{-1}$ and $\bar{\nu} = 15322.2 \text{ cm}^{-1}$ on the other hand were assigned to AlClPc-Ar₁ complexes according to their agreement with the other four emission spectra of AlClPc-Ar₁ complexes (cf. figure 6.7 and table 6.3).

The dispersed emission spectra of AlClPc-Ar₁ complexes recorded upon excitation at the eight frequencies marked by the comb in figure 6.6 are displayed in figure 6.7. As a guide to the eye, the dotted vertical lines mark the emission frequency for ex-

citation at $\bar{\nu}_{exc} = 15301.6 \text{ cm}^{-1}$. For each excitation wavelength the corresponding emission splits up into multiplets. This spectral fine structure recurs for each vibronic transition. The frequencies of all signals within the emission origin are listed in table 6.3 where the top row gives the respective excitation frequencies in cm^{-1} . Consequently, within one column one finds the signals displayed in the corresponding emission spectrum (as indicated in the top row) while examining the rows gives a picture of the occurrence of a certain transition.

Upon excitation at $\bar{\nu}_{exc} = 15301.6 \text{ cm}^{-1}$ three lines appear in the emission origin at which the first dominating one, which is slightly asymmetric and seems to have a tail to the red, coincides with the excitation frequency. Emission spectra congruent with the first in the left row of figure 6.7, are those upon excitation at $\bar{\nu}_{exc} = 15303.1 \text{ cm}^{-1}$ and $\bar{\nu}_{exc} = 15322.2 \text{ cm}^{-1}$ although two additional signals in the blue are present in the latter spectrum. Consequently, these three signals can be identified as one system with a small contribution of a second system in the case of excitation at $\bar{\nu}_{exc} = 15322.2 \text{ cm}^{-1}$. Another system of AlClPc-Ar₁ complexes is obviously displayed in the second ($\bar{\nu}_{exc} = 15302.6 \text{ cm}^{-1}$) and fourth ($\bar{\nu}_{exc} = 15307.0 \text{ cm}^{-1}$) panel of the left row of figure 6.7 where the first emission signal is present at the excitation wavelength of the second spectrum ($\bar{\nu}_{exc} = 15302.6 \text{ cm}^{-1}$). The pattern of the second panel in the left row also recurs within the first three spectra in the right row. However, for the latter spectra three additional signals with strongly varying intensity are present at 15319 cm^{-1} , 15311 cm^{-1} and 15289 cm^{-1} which are present as well in the bottom panel of the right row of figure 6.7. To summarize, at least three different systems within the eight examined AlClPc-Ar₁ complexes can be identified by analyzing the dispersed emission spectra.

Splitting of transitions in the dispersed emission spectrum of van der Waals clusters has been observed before in the case of a complex consisting of free-base phthalocyanine and one argon atom [15, 27]. At this, a splitting into three lines was presented. The explanation of this spectral characteristic involves, similarly as for the doubly split dispersed emission spectra of free-base phthalocyanine and Mg-phthalocyanine

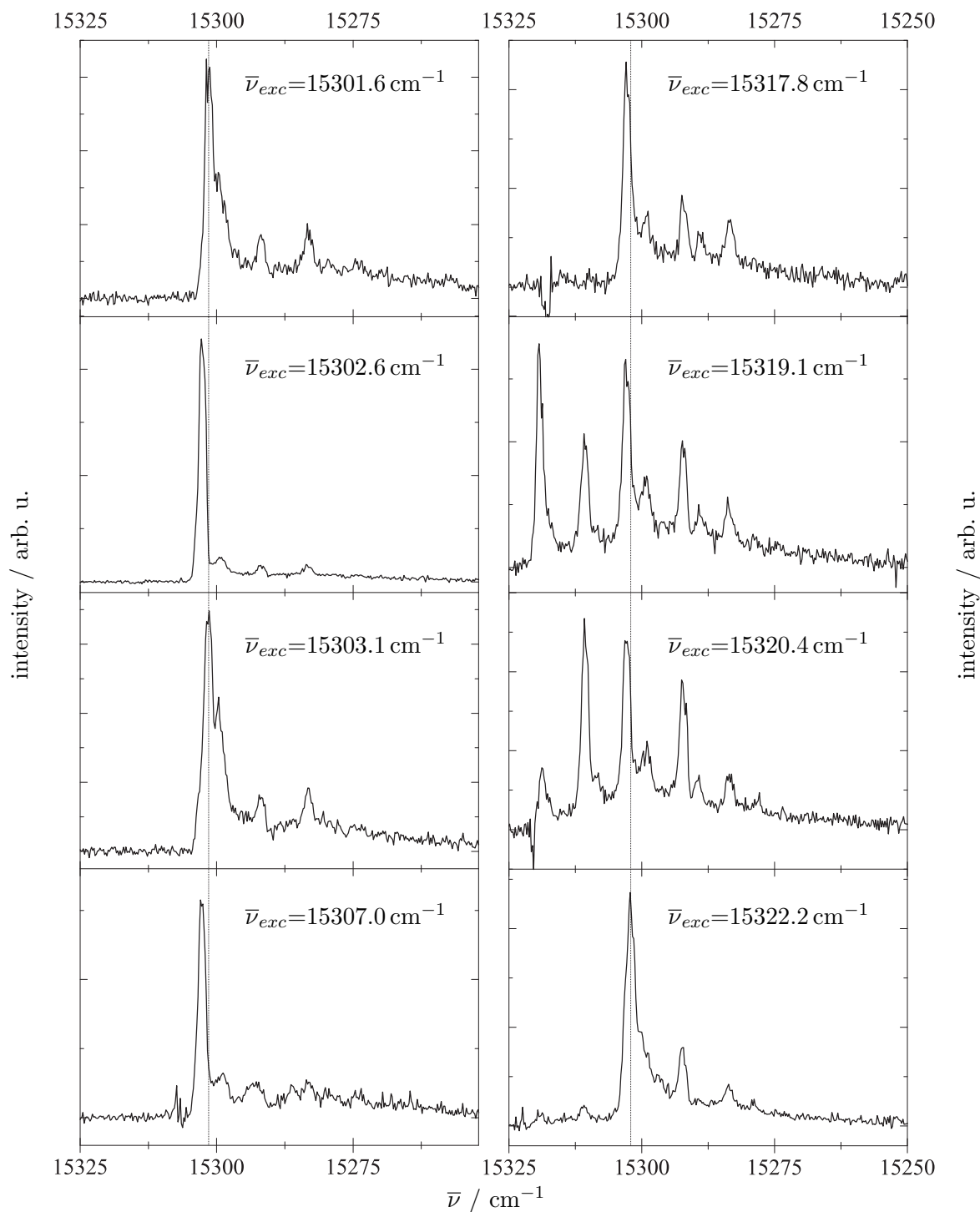


Fig. 6.7: Dispersed emission spectra of AlClPc-Ar₁ complexes excited at the eight frequencies marked by the comb in figure 6.6. The respective excitation wavenumbers are given in each panel. The dotted vertical lines mark the frequency of the emission origin resulting from excitation upon $\bar{\nu}_{exc} = 15301.6 \text{ cm}^{-1}$.

Tab. 6.3: List of emission frequencies of AlClPc-Ar₁ complexes observed for excitation at the frequencies given in the top row. The excitation frequencies correspond to the signals marked by the comb in figure 6.6. The values in every row correspond within the error of 0.3 cm⁻¹ to one emission signal of AlClPc-Ar₁ complexes. For further details see text. All values are given in cm⁻¹.

15301.6	15302.6	15303.1	15307.0	15317.8	15319.1	15320.4	15322.2
-	-	-	-	-	15319.1	15318.8	15319.0
-	-	-	-	-	15310.5	15310.6	15310.8
-	15302.6	-	15302.6	15302.7	15302.6	15302.3	15301.7
15301.3	-	15301.5	-	-	-	-	-
-	15299.4	-	15299.1	15299.2	15299.3	15299.3	-
15291.9	15291.9	15292.0	-	15292.1	15292.0	15292.2	15292.2
-	-	-	-	15288.9	15288.9	15289.2	-
15283.2	15283.3	15283.2	-	15283.4	15283.4	15283.4	15283.4

(see above), a multiple level system representing different solvation configurations of the first helium layer around the dopant [15, 27]. Thus, the split transitions of the AlClPc-Ar₁ complexes can be interpreted as emission without or with relaxation of the first helium layer upon electronic excitation of the dopant (cf. ref. [27]). Yet, due to the consistent broad background signal within the spectral range of the AlClPc-Ar₁ complexes (cf. figure 6.6), unambiguous discrimination of sharp lines from underlying broad spectral contributions is not possible. It should be noted that for excitation energies differing by more than ~ 10 cm⁻¹ relaxation processes within the droplets solvation shell are likely as a cause of red shifted emission. But, coinciding emission origins for excitation energies that differ within a range of up to ~ 6 cm⁻¹ can be interpreted as mating ZPL and PW in the fluorescence excitation spectrum (cf. chapter 3.1.2). Thus, dissipation of excess excitation energy following the electronic excitation prior to radiative decay may be responsible for identical emission spectra. Another possibility to explain several favourite emission frequen-

cies of AlClPc-Ar₁ complexes is by assuming different stable and metastable sites for the argon atom in vicinity of the AlClPc molecule which may relax into each other upon electronic excitation.

In summary, regarding the general behaviour of AlClPc in superfluid helium droplets considering the solvation shift and minor variation of vibronic transitions compared to the isolated molecule, it can be assumed to be a rather rigid molecule whose spectroscopic properties are rather independent of the superfluid helium environment. However, closely investigating high-resolution dispersed emission spectra of the bare molecule as well as van der Waals complexes with argon, reveals tiny details of the interactions with the helium environment and in particular with the first solvation layer.

6.2 2,9,16,23-Tetra-*tert*-butylphthalocyanine (TTBPc)

2,9,16,23-Tetra-*tert*-butylphthalocyanine (TTBPc) is an alkyl substituted phthalocyanine belonging to the point group D_{2h} .

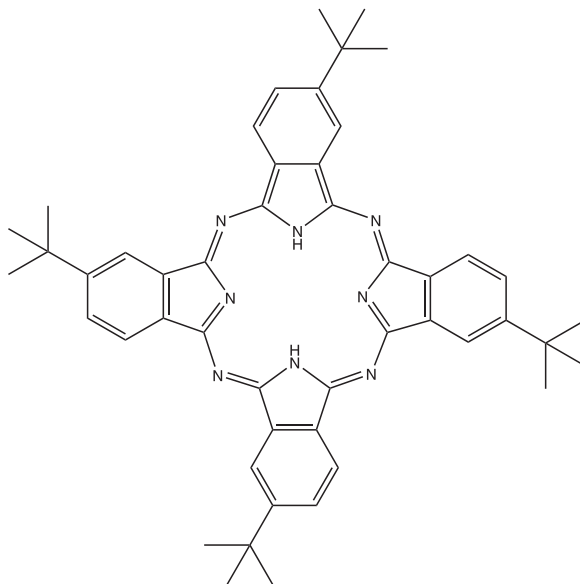


Fig. 6.8: Chemical structure of 2,9,16,23-tetra-*tert*-butylphthalocyanine (TTBPc).

For this study fluorescence excitation and dispersed emission spectra were recorded with the continuous helium droplet machine using the continuous wave dye laser (Coherent Innova 899-29 autoscan) operated with DCM yielding an average power of 200 mW (measured directly behind the laser). A color glass filter RG695 (Schott) in front of the PMT was used to eliminate laser stray light. The heating voltage of the pick-up cell optimized for single doping of the droplets was 12.7 V corresponding to an oven temperature of approx. 294 °C. The expansion parameters were $p_0 = 30$ bar and $T_0 = 11.6$ K. In order to record an overview excitation spectrum, the TTBPc sample was investigated in the pulsed machine using the Nd:YAG pumped dye laser (Lambda Physik Scanmate 2E) operated at 20 Hz with DCM yielding an average power of 1.3 mJ/pulse. The dye laser was operated with resonator and preamplifier

but without amplifier. Stagnation conditions for the pulsed valve were $p_0 = 80$ bar and $T_0 = 21.5$ K. The color glass filter in front of the PMT and the heating voltage of the pick-up oven were the same as in the continuous experiment.

6.2.1 Fluorescence excitation of TTBPc

The fluorescence excitation spectrum of TTBPc recorded with the pulsed helium droplet setup is displayed in the top panel of figure 6.9 in comparison with that of free-base phthalocyanine recorded in the continuous droplet source (bottom panel) taken from reference [52]. Sharp lines accompanied by weak PWs are present throughout the TTBPc spectrum since the excitation laser was attenuated by inserting two lens cleaning tissues into the laser beam path. The most intense spectral feature in the upper panel around 14982 cm^{-1} is assigned to the electronic origin of TTBPc. Obviously, the vibrational modes of free-base phthalocyanine appear with

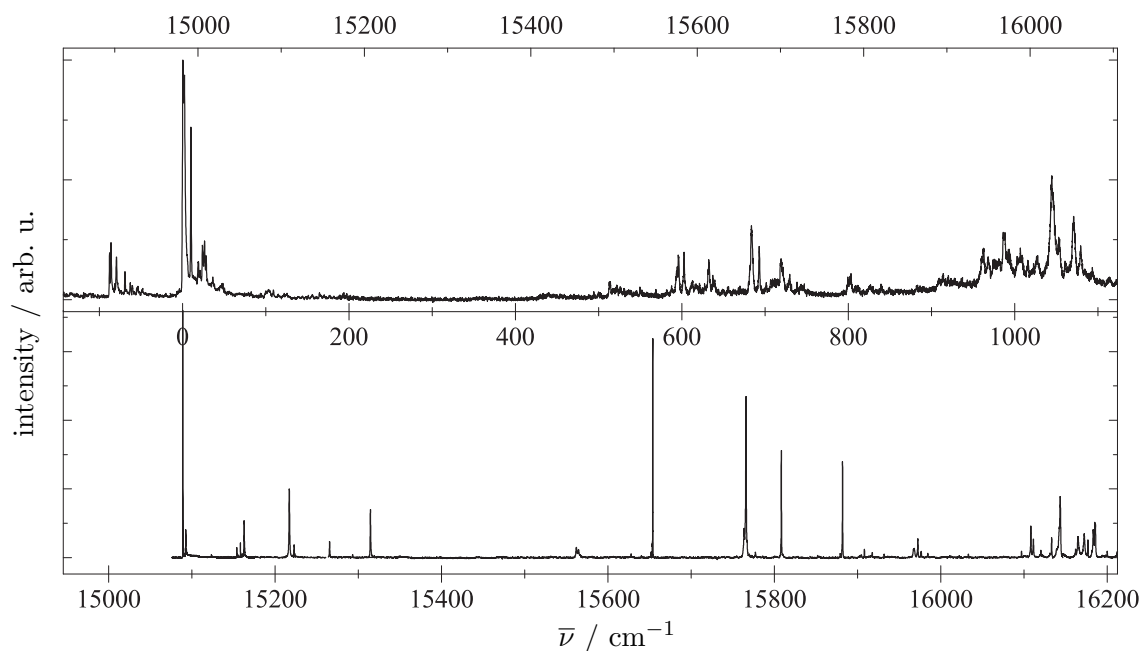


Fig. 6.9: Fluorescence excitation spectra of TTBPc (top panel) recorded with the pulsed setup and free-base phthalocyanine (bottom panel) measured by using the continuous machine.

similar frequencies for the substituted species. However, the low-energy modes below $\bar{\nu} = 300 \text{ cm}^{-1}$ are significantly reduced in intensity which may be due to intramolecular vibrational redistribution of the vibrational energy to torsional or bending modes of the *tert*-butyl groups. The signals in the fluorescence excitation spectrum of TTBPc which are spectrally shifted to the red of the most intense signal group are probably due to complexes of TTBPc with residual gas atoms or alternatively impurities within our TTBPc sample. At this, different TTBPc species may originate from the two equivalent positions for each alkyl substituent at the benzopyrrole unit which finally leads to four possible structural isomers.

High-resolution fluorescence excitation spectra of TTBPc recorded with the continuous helium droplet source showing the spectral region of electronic origins (top panel) compared to the corresponding vibronic transitions (bottom panel) are displayed in figure 6.10. The spectral structure of the top panel in figure 6.10 is, with approximately 684 cm^{-1} of excess energy, repeated quite similarly. Although, the line widths of the vibrational modes are increased by approximately one order of

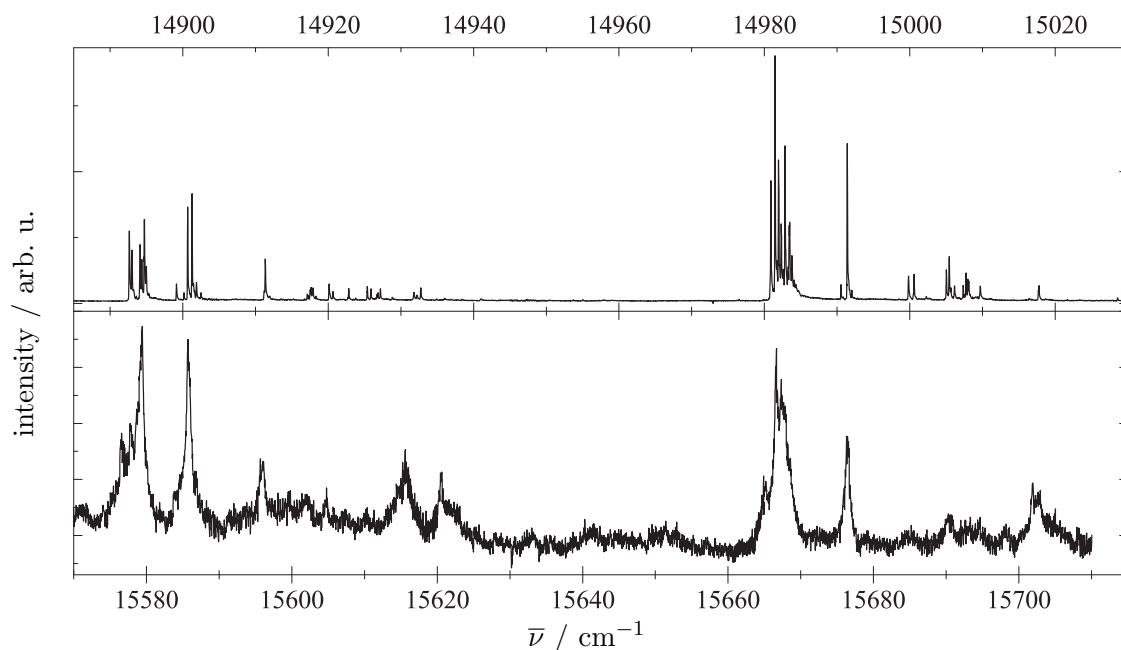


Fig. 6.10: Fluorescence excitation spectra of TTBPc displaying electronic origins (top panel) and the corresponding vibronic transitions (bottom panel).

magnitude compared to a width of $\sim 0.1 \text{ cm}^{-1}$ for signals within the region of the electronic origins. For example, the signal at 14991.4 cm^{-1} (cf. top panel of figure 6.10) exhibits a line width of $0.08(1) \text{ cm}^{-1}$ while the signal at 15676.5 cm^{-1} (cf. bottom panel of figure 6.10) possesses a Lorentzian width of $0.7(1) \text{ cm}^{-1}$. These line widths correspond to life times of 66.4 ps and 7.6 ps respectively and their difference is presumably due to fortunate intramolecular vibrational redistribution of the vibrational energy via the *tert*-butyl substituents.

Investigating the most intense signal group of the fluorescence excitation spectrum which is assigned to the electronic origin of TTBPc in the continuous helium droplet setup results in the fluorescence excitation spectrum which is shown in figure 6.11. Several dominating sharp lines accompanied by weaker sharp spectral features are present. Although the spectral fine structure resembles that of the electronic origin of etioporphyrin I (cf. chapter 7.6.1), a porphyrin derivative substituted with four methyl and four ethyl groups, the different sharp signals displayed in figure 6.11 belong to at least four different systems as will be proven in section 6.2.2 by analyzing the dispersed emission spectra upon excitation at the seven most intense signals present in figure 6.11. This would also fit to the existence of four configurational

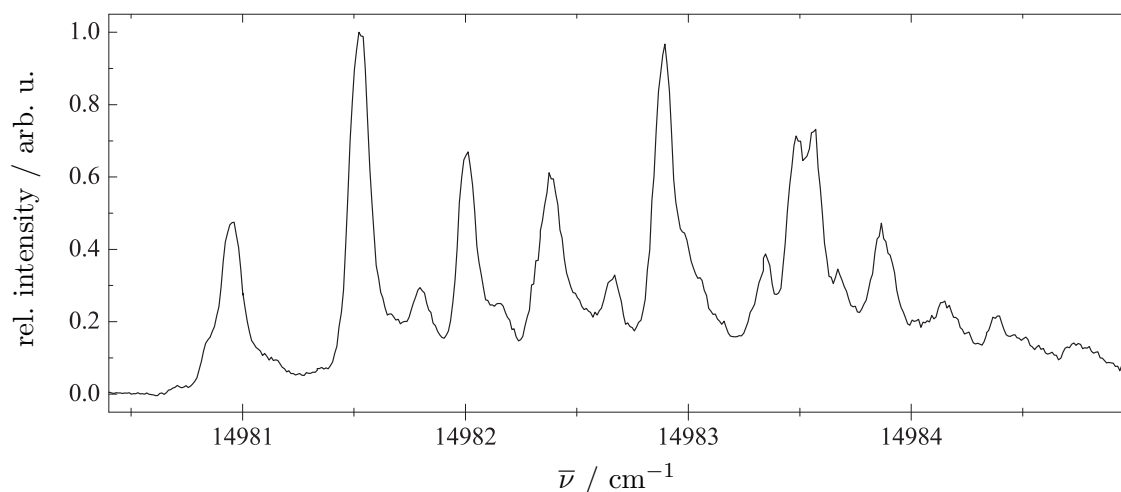


Fig. 6.11: Normalized fluorescence excitation spectrum of the electronic origin of TTBPc recorded with the continuous helium droplet setup.

isomers of TTBPc within our sample, but, since obviously more than four sharp signals are present within the spectral structure displayed in figure 6.11, only additional combination with different solvation configurations of the surrounding helium could fully account for the observed fine structure.

Although, due to the presence of several species within our TTBPc sample a final assignment of all signals present in the fluorescence excitation spectrum is not possible, one can state that the existence of floppy substituents like *tert*-butyl groups still enables sharp transitions upon electronic excitation and does not necessarily cause massive line broadening effects as has been observed before for alkyl substituents [11, 64].

6.2.2 Dispersed emission of TTBPc

Dispersed emission spectra of TTBPc upon excitation at the seven most prominent signals within the spectral feature around 14982 cm^{-1} (cf. figure 6.11) are depicted in figure 6.12. The respective origin is plotted separately as thick black line for each spectrum. The overall spectral structure presenting sharp lines throughout the dispersed emission spectrum with dominating signal groups around 14850 cm^{-1} and 14300 cm^{-1} is obviously similar for all seven spectra and resembles that of the fluorescence excitation spectrum displayed in the top panel of figure 6.9. Although, closer investigation reveals that clear deviations are recognizable, namely the presence of additional modes or varying intensity ratios of certain vibrational modes. This is also confirmed by the data extracted from the dispersed emission spectra shown in figure 6.12 which is presented in table 6.4. For the four different species present within the seven spectra of figure 6.12 absolute frequencies $\bar{\nu}$ of the observed transitions are given along with $\bar{\nu}_{rel}(S_0) = \bar{\nu}_0 - \bar{\nu}$, the wavenumbers relative to the emission origin corresponding to the vibrational modes of the electronic ground state. Indicated on top of two corresponding columns are the respective excitation frequencies $\bar{\nu}_{exc}$. All data are given in cm^{-1} . For excitation at $\bar{\nu}_{exc} = 14982.4\text{ cm}^{-1}$, $\bar{\nu}_{exc} = 14982.5\text{ cm}^{-1}$ and $\bar{\nu}_{exc} = 14983.9\text{ cm}^{-1}$ the transition frequencies are identi-

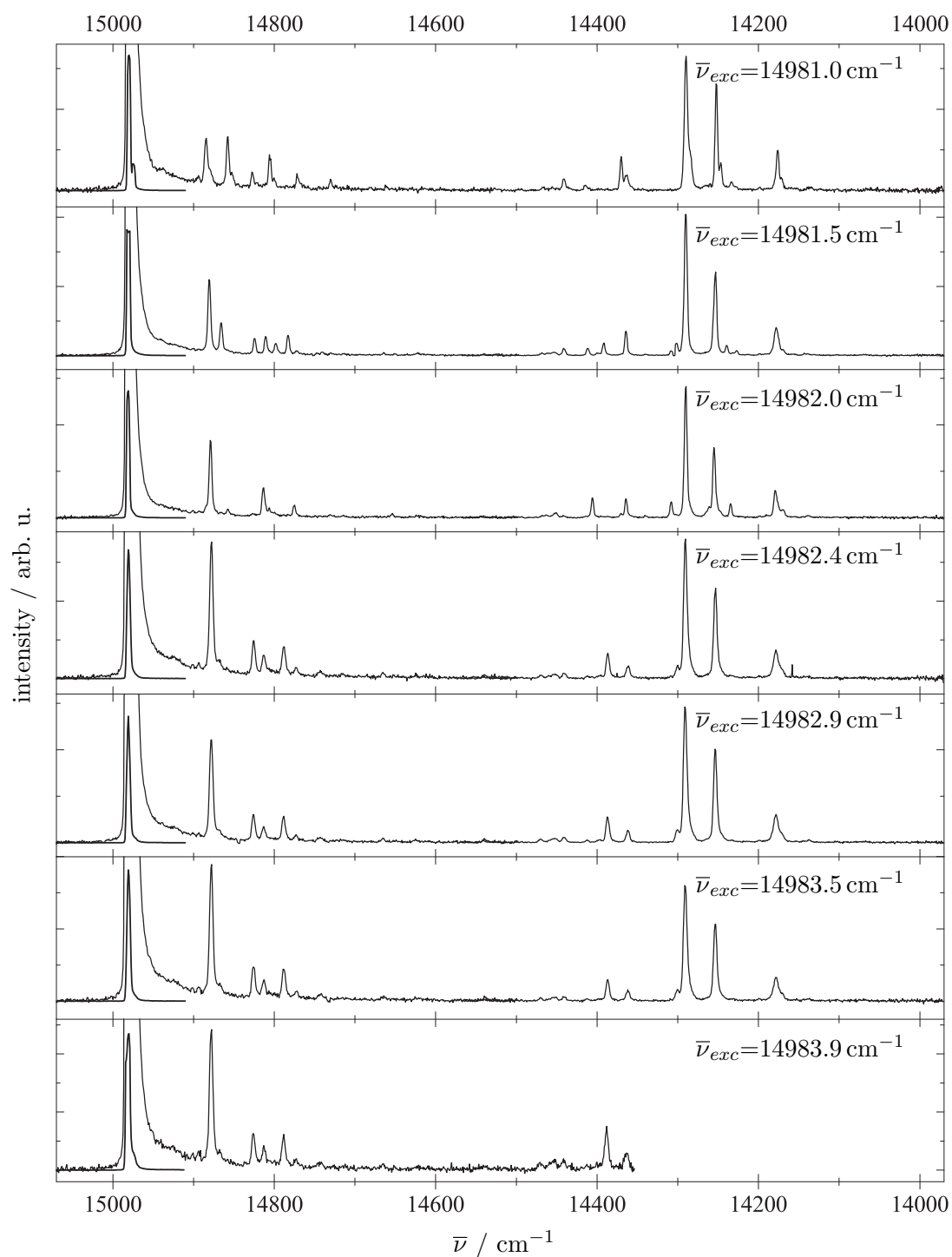


Fig. 6.12: Dispersed emission spectra of TTBPc for excitation at the seven most intense signals of the spectral feature displayed in figure 6.12. The emission origin is plotted separately as thick black line for each spectrum. The excitation frequency is given in each panel.

Tab. 6.4: List of vibronic transitions $\bar{\nu}$ obtained from the dispersed emission spectra of TTBPc in superfluid helium droplets by excitation at the seven most intense signals displayed in figure 6.11 which are given in the top row. The frequencies could be determined with an accuracy of 1 cm^{-1} (cf. chapter 4.1.3.2). $\bar{\nu}_{rel} (S_0) = \bar{\nu}_0 - \bar{\nu}$ gives the frequencies relative to the respective emission origin corresponding to the vibrational modes of the electronic ground state S_0 . All data are given in cm^{-1} .

14981.0		14981.5		14982.0		14982.9 ^a	
$\bar{\nu}$	$\bar{\nu}_{rel} (S_0)$	$\bar{\nu}$	$\bar{\nu}_{rel} (S_0)$	$\bar{\nu}$	$\bar{\nu}_{rel} (S_0)$	$\bar{\nu}$	$\bar{\nu}_{rel} (S_0)$
14981	0	14982	0	14982	0	14982	0
14885	96	14881	101	14879	103	14878	104
14858	123	14866	116	14858	124	14826	156
14827	154	14824	157	14814	168	14813	169
14806	175	14811	171	14775	207	14788	194
14771	210	14798	184	14451	531	14773	209
14730	251	14783	199	14406	576	14470	512
14441	540	14441	541	14364	618	14453	529
14414	567	14412	570	14308	674	14441	541
14370	611	14392	590	14290	692	14412	570
14290	691	14364	618	14255	727	14387	595
14252	729	14305	677	14235	747	14362	620
14233	748	14290	692	14179	803	14300	682
14176	805	14253	729			14291	691
		14239	743			14253	729
		14178	804			14178	804

^aNote that the dispersed emission spectra of all four bottom panels of figure 6.12 are identical.

cal to those observed upon excitation at $\bar{\nu}_{exc} = 14982.9 \text{ cm}^{-1}$. Consequently, only the four bottom panels show identical spectra while the three top graphs present three

differing dispersed emission spectra. This observation corresponds to an assignment of four different systems within the most intense signal group of the fluorescence excitation spectrum of TTBPc and fits to a possible existence of four different TTBPc configurational isomers within our sample as was already mentioned in section 6.2.1. Comparing all seven spectra displayed in figure 6.12, the first panel stands out since excitation at $\bar{\nu}_{exc} = 14981.0 \text{ cm}^{-1}$ leads to a second emission spectrum which is red shifted by 6 cm^{-1} , a phenomenon which was also observed for three other phthalocyanines (free-base phthalocyanine, Mg-phthalocyanine [27, 52, 90, 96] and AlClPc) and discussed in chapter 6.1.2. However, comparing all four phthalocyanines, TTBPc exhibits the smallest red shift of the second emission spectrum which is equivalent to the lowest energy difference between the metastable and global minimum configuration of the helium solvation shell around the dopant.

For excitation of the TTBPc sample at eight different signal groups shown in the top panel of figure 6.10 the origins of the resulting dispersed emission spectra are pictured in figure 6.13. All spectra of figure 6.13 were corrected for stray light of the excitation laser (cf. chapter 4.1.3.2), however, stray light correction for the third and fourth panel of the left row did not work properly. Differing numbers of

Tab. 6.5: List of emission frequencies of TTBPc observed for excitation at the frequencies given in the top row. The values in every row correspond to one emission signal of TTBPc. For further details see text. All values are given in cm^{-1} .

14981.0	14990.6	14991.4	14995.7	14999.9	15007.4	15017.8	15028.6
-	-	-	-	-	-	-	15029
-	-	-	-	-	-	15018	15020
-	-	-	-	-	15007	15008	15008
-	-	-	-	15000	14997	15000	15000
-	14991	14991	14992	14992	14992	14992	14992
14981	14982	14981	14982	14982	14982	14982	14982
14975	-	14976	14977	-	-	-	-

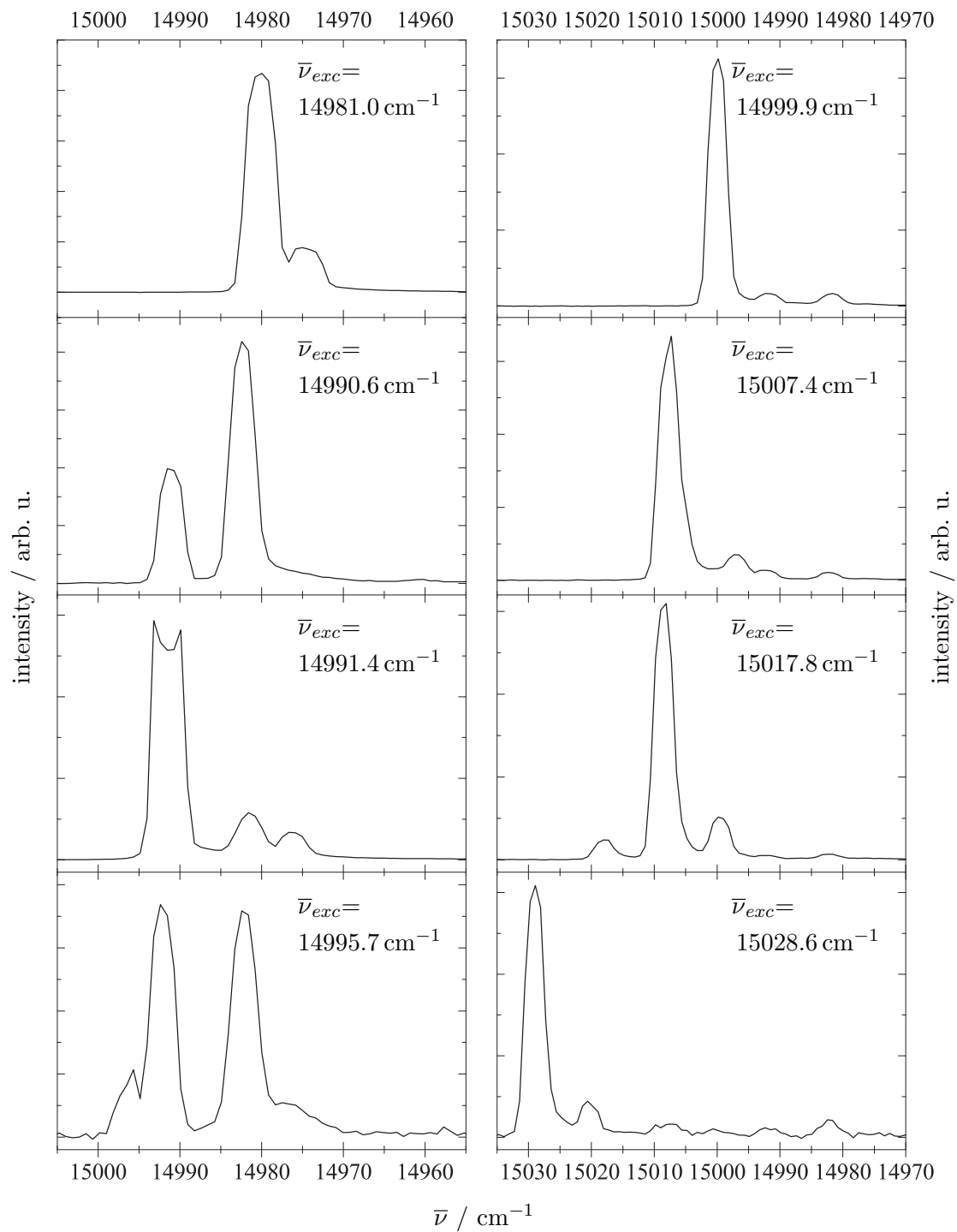


Fig. 6.13: Split origins of the dispersed emission spectra of TTBPc. The excitation frequency is given for each panel. For details see text.

sharp emission lines with varying intensity ratios indicate several systems present in the fluorescence excitation spectrum. Though, comparing the emission frequencies within all pictured emission origins reveals recurring favourite spectral positions differing by $8 - 10 \text{ cm}^{-1}$ (cf. table 6.5). Yet, a final interpretation of these findings remains difficult since it is unclear whether the signals in the excitation spectrum originate from complexes of TTBPc with residual gas molecules or different phthalocyanine species like e.g. tri-*tert*-butylphthalocyanine or different structural isomers of TTBPc. Furthermore, because of the significantly lower signal intensity of the vibronic transitions one cannot determine whether the fine structure exhibited in the emission origin recurs for the vibronic transitions. But, in analogy to free-base phthalocyanine, Mg-phthalocyanine (see references [27, 52, 90, 96]) and the AlClPc-Ar₁ complexes (see chapter 6.1.3), it is very likely.

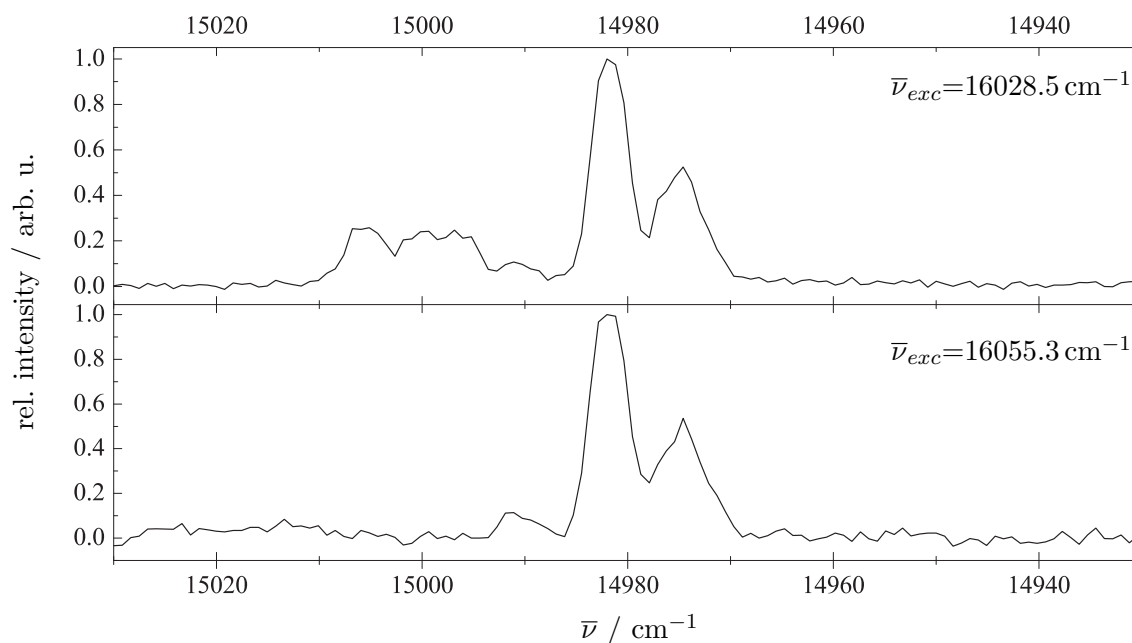


Fig. 6.14: Dispersed spectra of TTBPc recorded upon excitation at vibronic transitions. The respective excitation wavelength is given for each panel. The spectra are normalized to the most intense emission signal.

Upon excitation of vibronic transitions, dispersed emission spectra of TTBPc reveal an at least triply split emission origin with sharp signals at 14991 cm^{-1} , 14982 cm^{-1}

and 14975 cm^{-1} (see figure 6.14). In the case of $\bar{\nu}_{exc} = 16028.5\text{ cm}^{-1}$ an additional blue shifted signal contribution is present although its fine structure is not unambiguously identifiable.

All in all, TTBPc presents sharp lines in its electronic spectra and also mirror symmetry of the fluorescence excitation and the dispersed emission spectra although a final assignment of the different species remains impossible. Hence, despite substitution with four presumably floppy *tert*-butyl groups, electronic spectra of TTBPc show characteristics of a rigid molecule which indicates that electronic excitation leaves the molecular structure unaffected.

7 Porphyrin species

Porphyrins are aromatic compounds which consist of four pyrrole units connected via methine bridges (cf. compound 1 in figure 7.1). They are important chromophores in biological light harvesting systems and photoreaction centers. Similar to the phthalocyanines, the four inner nitrogen atoms form complexes with various metal atoms like for example in the well known molecules heme (Fe) and chlorophyll (Mg). Common derivatives of porphyrins are chlorins, in which one of the four pyrrole units is replaced by a pyrroline unit where one double bond is hydrogenated (cf. compound 2 in figure 7.1).

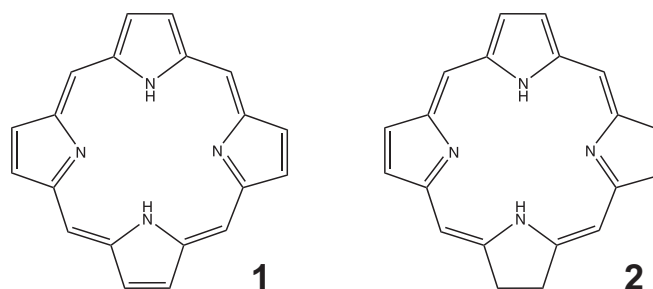


Fig. 7.1: Chemical structure of free-base porphyrin (1) and free-base chlorin (2).

Apart from their fundamental biological functions in photosynthesis, oxidation and reduction reactions, and oxygen transport, porphyrins are, like phthalocyanines (cf. chapter 6), used as photosensitizers in photodynamic therapy [99, 100] and as red emitters in OLEDs (see for example references [83, 101]).

In contrast to the phthalocyanines, porphyrins generally exhibit rather poor fluorescence quantum yields due to efficient decay of the excited state via intersystem

crossing. In the case of free-base porphyrin for example, approximately 90 % of the excited molecules decay into the triplet state from where phosphorescence takes place with a very low quantum yield of $\Phi_P = 0.00014$ [102, 103].

The substituted porphyrin derivatives investigated for this study differ in position (methine or pyrrole substituted), number (two or four), and type (alkyl or aryl) of their substituents. In order to separate the substituent modes from the vibrational mode pattern of the macrocyclic backbone free-base porphyrin was studied too.

7.1 Free-base porphyrin (FBP)

Regarding its structural formula (cf. fig. 7.1 compound 1), free-base porphyrin (FBP) belongs to the point group D_{2h} .

As already mentioned in the introduction of chapter 7, FBP exhibits a very low fluorescence quantum yield due to a large intersystem crossing rate. This is equally supported by the low oscillator strength of $f = 0.01$ for the $S_0 \rightarrow S_1$ transition [104] compared to $f = 0.10$ for the corresponding chlorin [105].

At present, fluorescence excitation spectra of FBP in supersonic jet experiments are published [56, 106]. Moreover, the fluorescence excitation spectrum of FBP in a continuous helium droplet beam with a pulsed laser has been measured [7, 55]. In this case, the electronic origin as well as a low-resolution excitation spectrum including the first two vibrational transitions were documented. Both experiments reveal the electronic origin as the most intense transition followed by two less intense vibrations, one around 150 cm^{-1} and one around 300 cm^{-1} . Though, the relative intensities of those modes differ in both experiments. Precisely, the vibronic transitions display relative intensities compared to the electronic origin of less than 40% in the supersonic jet experiment [56, 106] and less than 80% in the helium droplet experiment [55] respectively. This is due to the fact that, contrary to the supersonic jet spectra, the spectra in helium droplets were not corrected for the laser intensity profile. In addition, saturation was not controlled in the latter experiment.

All data presented in the following were recorded with the continuous wave dye laser (Coherent Innova 899-29 autoscan) operated with rhodamine 6G yielding an average power of 220 mW (measured directly behind the dye laser). A color glass filter RG630 (Schott) in front of the PMT was used to eliminate laser stray light. The heating voltage of the pick-up cell optimized for single doping of the droplets was 7.5 V corresponding to an oven temperature of approx. $145 \text{ }^\circ\text{C}$. Typical expansion conditions were $p_0 = 25 \text{ bar}$ and $T_0 = 12.8 \text{ K}$.

7.1.1 Fluorescence excitation of FBP

The fluorescence excitation spectrum of FBP in superfluid helium droplets is displayed in figure 7.2. The spectrum is scaled to the most intense signal, the 0_0^0 -transition of FBP at $\bar{\nu}_0 = 16312.4 \text{ cm}^{-1}$. Throughout the spectrum one observes sharp lines as expected for a rigid molecule in helium droplets.

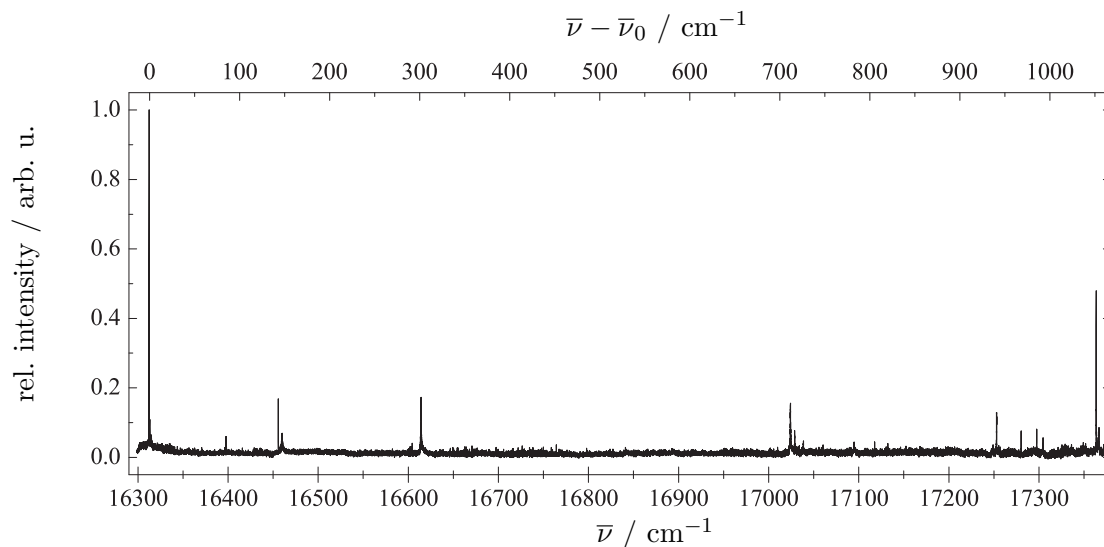


Fig. 7.2: Fluorescence excitation spectrum of FBP normalized to the fluorescence intensity of the electronic origin at $\bar{\nu}_0 = 16312.4 \text{ cm}^{-1}$.

The vibrational transition frequencies of the first excited singlet state relative to the electronic origin $\bar{\nu}_{rel} = \bar{\nu} - \bar{\nu}_0$ are given in table 7.1 where they are compared to the supersonic jet experiment ($\bar{\nu}_{jet}$) as well as to the previous measurements of FBP in helium droplets ($\bar{\nu}_{dr}$). Comparing the transition energies for the electronic origin, just a minor solvent shift of $8 \pm 4 \text{ cm}^{-1}$ to the red is observed by switching from the isolated molecules into the superfluid helium droplet matrix. It should be noted that, as far as an assignment is provided in reference [106], the vibrational modes presented in helium droplets correspond to fundamental vibrations of FBP. Taking into account the different experimental accuracies in determining the laser wavelength (see footnotes of table 7.1), the vibrational energies are in good agreement.

Tab. 7.1: List of vibronic transitions obtained from the fluorescence excitation spectrum of FBP in superfluid helium droplets. The line positions $\bar{\nu}$ could be determined with an accuracy of 0.05 cm^{-1} . $\bar{\nu}_{rel} = \bar{\nu} - \bar{\nu}_0$ indicates the frequency shift relative to the electronic origin at $\bar{\nu}_0 = 16312.4 \text{ cm}^{-1}$. $\Delta\bar{\nu}_L$ are the respective Lorentzian line widths. τ gives the resulting life times. $\bar{\nu}_{dr}$ are the values available for $\bar{\nu}_{rel}$ from references [7, 55] measured in helium droplets while $\bar{\nu}_{jet}$ are the corresponding data from reference [106] recorded in a supersonic jet. The last column gives the shift between the vibrational energies deduced from the helium droplet experiment relative to the supersonic jet measurements. Unless otherwise noted, all data are given in cm^{-1} .

$\bar{\nu}$	$\bar{\nu}_{rel}$	$\Delta\bar{\nu}_L$	τ / ps	$\bar{\nu}_{dr}$ ^a	$\bar{\nu}_{jet}$ ^b	$\bar{\nu}_{shift}$
16312.4	0	-	-	0	0	0
16397.8	85.4	-	-	-	-	-
16455.8	143.4	-	-	-	140	+3
16459.9	147.5	1.5(1)	3.5	147	148	-1
16614.1	301.7	0.76(6)	7.0	302	304	-2
17024.2	711.8	0.66(4)	8.0	-	712	0
17028.8	716.4	0.28(3)	19.0	-	714	+2
17038.5	726.1	0.40(9)	13.3	-	719	+7
17094.8	782.4	0.9(2)	5.9	-	783	-1
17249.0	936.6	0.20(7)	26.5	-	936	+1
17252.9	940.5	0.30(2)	17.7	-	940	+1
17280.2	967.8	0.25(2)	21.2	-	961	+7
17297.5	985.1	0.16(1)	33.2	-	984	+1
17304.5	992.1	0.15(2)	35.4	-	996	-4
17363.5	1051.1	0.18(1)	29.5	-	1049	+2
17366.6	1054.2	0.18(2)	29.5	-	1051	+3

^aData taken from ref. [55]. Accuracy of the frequencies relative to the electronic origin is $\pm 1 \text{ cm}^{-1}$.

^bData taken from ref. [106]. Accuracy of the frequencies relative to the electronic origin is $\pm 2 \text{ cm}^{-1}$.

One exception is the lowest energy mode with 85.4 cm^{-1} which appears neither in the supersonic jet nor in the formerly performed helium experiment. Although, in the excitation spectrum recorded in a supersonic jet a weak vibrational transition appears at $\bar{\nu}_{jet} = 105\text{ cm}^{-1}$ [106]. In case of the helium droplet experiment described in reference [55], the rather weak mode (cf. fig. 7.2) may not be visible due to the low signal-to-noise ratio of the low resolution spectrum.

The electronic origin of FBP in helium droplets is displayed in figure 7.3. The top panel shows the excitation spectrum measured for the purpose of this study using a continuous nozzle and a continuous wave laser while the bottom panel, adapted from reference [7], was measured with a pulsed laser using an energy of 2.0 mJ/pulse .

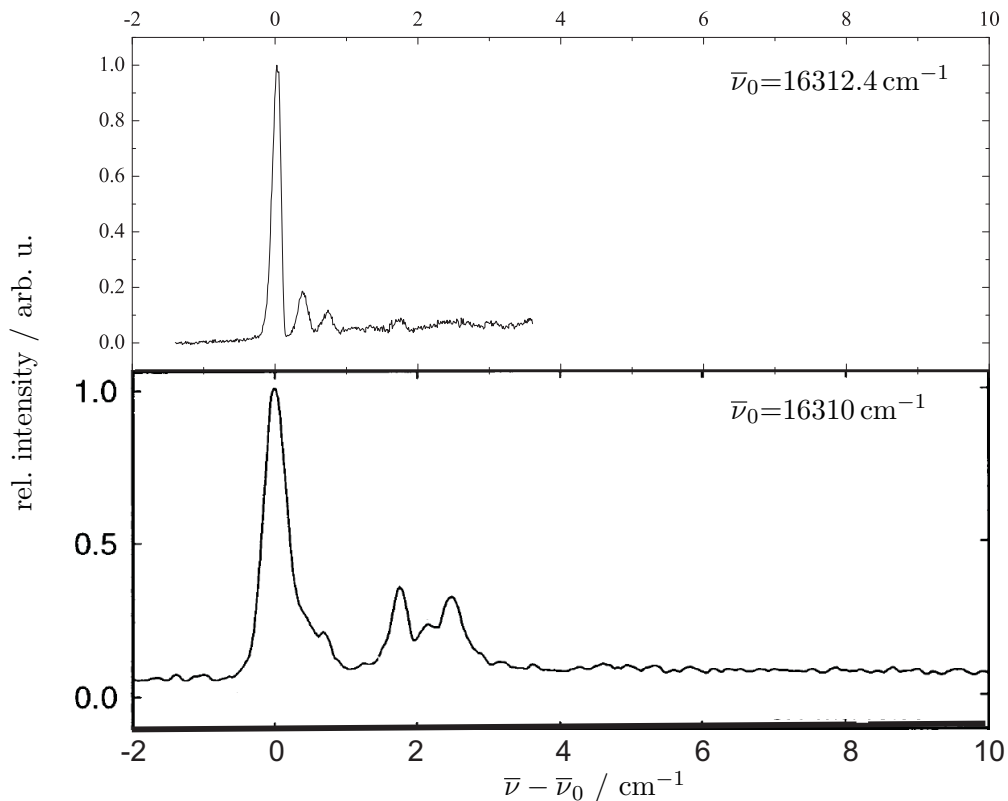


Fig. 7.3: Fluorescence excitation spectrum of FBP in helium droplets at the electronic origin. Comparison of excitation with continuous wave laser (top panel) and pulsed laser (bottom panel). The bottom panel is adapted from ref. [7]. Wave-numbers are given relative to the electronic origin.

Both spectra are normalized to the ZPL. The wavenumber axis is relative to the frequency of the ZPL. In the top panel three sharp lines are displayed. The first most intense signal with a width of about 0.2 cm^{-1} is followed within distances of $\bar{\nu}_{rel} = 0.4 \text{ cm}^{-1}$ and 0.7 cm^{-1} by two signals with relative intensities of 0.19 and 0.12. This group of signals is followed by a weak spectral feature that is blue-shifted by approximately 2 cm^{-1} . Apart from the larger line widths exhibited throughout the spectrum in the bottom panel – due to the band width of 0.25 cm^{-1} for the pulsed laser used in [7] – the intensity of this spectral structure is significantly amplified. This kind of dependence of the fluorescence signals of the electronic origin on the laser intensity argues for assigning the three sharp signals to the ZPL while the structure which is 2 cm^{-1} blue-shifted corresponds to the PW (cf. chapter 3.1.2).

An overview of the fine structures of several vibronic transitions of FBP in helium droplets is given in figure 7.4. The first panel in the left column displays the electronic origin. As can be seen, the first two vibrational transitions, at $\bar{\nu}_{rel} = 85.4 \text{ cm}^{-1}$ and 143.4 cm^{-1} , exhibit the same spectral structure of a three-membered signal group as the electronic origin. This observation supports the assignment of the lowest frequency mode belonging to a vibrational mode of FBP instead of belonging to an impurity. Interestingly, both low-energy vibrations show a triplet substructure in the first intense signal. This splitting was thought to be due to rotational fine structure and, thus, was tried to simulate by means of the PGOPHER software [107].

Assuming a symmetric top with D_{4h} symmetry, a rotational spectrum that roughly reproduces the experimental was simulated by manually changing parameters, namely the rotational constants and the rotational line width. The initial values for the rotational constants B_C and $B_A = B_B$ used for this simulation were calculated from the moment of inertia $I = 1.1 \cdot 10^{-37} \text{ g cm}^2$ [108] by using $B = \frac{h}{8\pi^2 c I}$. This resulted in $B = 2.54 \cdot 10^{-2} \text{ cm}^{-1}$. To account for the droplet environment, B_C , the rotational constant parallel to the symmetry axis of the molecule was modified to $B_C = 1/3 \cdot B = 8.47 \cdot 10^{-3} \text{ cm}^{-1}$ considering the reduction of rotational constants that has previously been observed for large rigid rotors in helium dro-

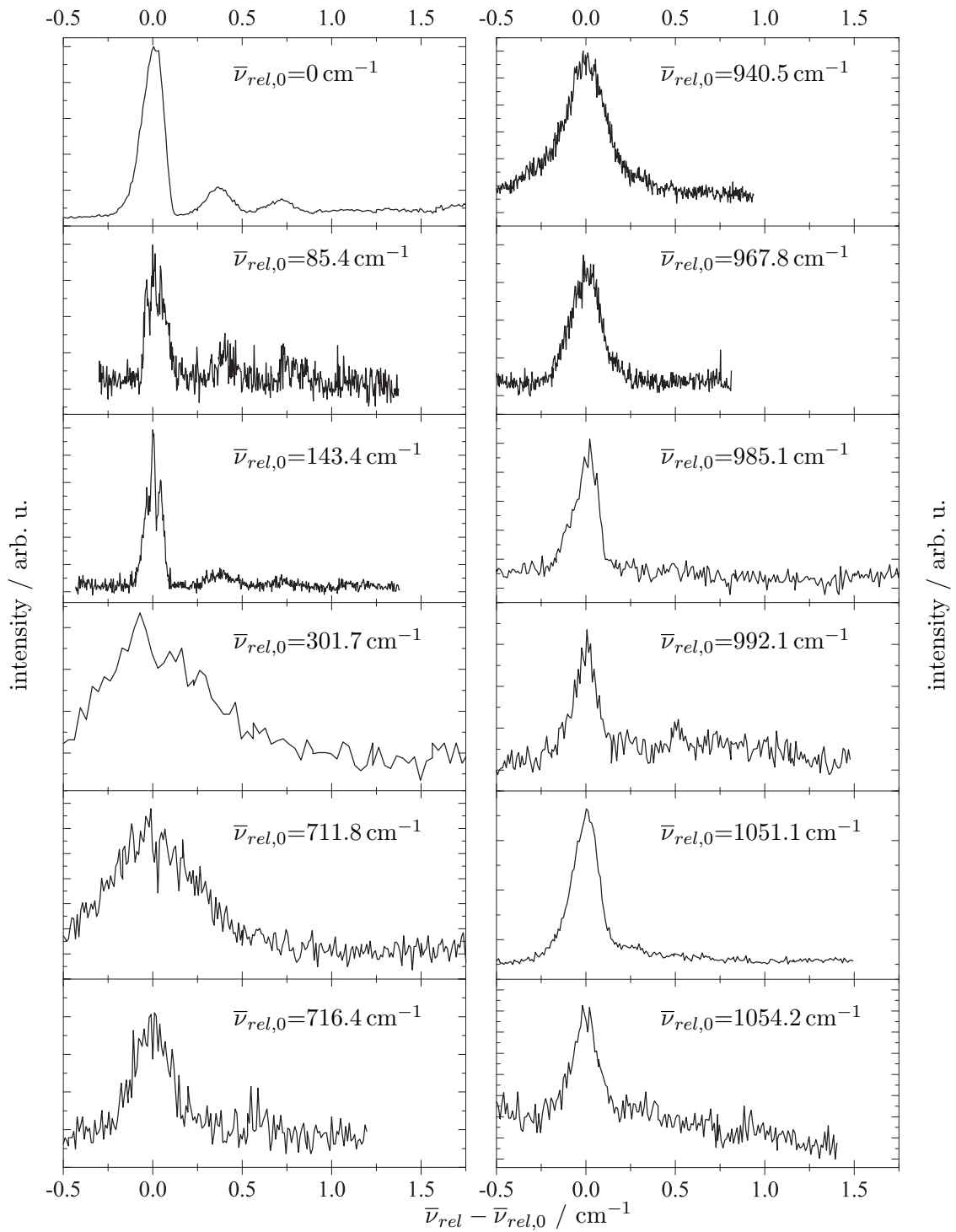


Fig. 7.4: Fine structure of vibronic transitions of the fluorescence excitation spectrum of FBP in helium droplets. The wavenumber axes are relative to the respective transition frequency. Frequencies relative to the electronic origin at $\bar{\nu}_0 = 16312.4 \text{ cm}^{-1}$ are noted in each panel.

plets (this is equivalent to an increased effective moment of inertia by a factor of about 3 and explained by a fraction of non-superfluid helium that adiabatically follows the molecular rotation) [1, 20, 109, 110, 111, 112]. Furthermore, as initial value for the rotational constant perpendicular to the molecule’s symmetry axis $B_A = B_B = 2 \cdot B_C = 1.69 \cdot 10^{-2} \text{ cm}^{-1}$ was assumed. The rotational temperature $T_{rot} = 0.38 \text{ K}$ was kept fixed throughout the whole simulation procedure. This was also the case for the maximum rotational quantum number $J_{max} = 11$ which was estimated by a Boltzmann population distribution. The other parameters were kept at their default values throughout the simulation procedure. In order to approximate the width of the entire rotational structure as well as the intensity distribution, manually changing the rotational constants B_B and B_C as well as the Lorentzian width of a single rotational line $\Delta\bar{\nu}_L$ always led to a significantly changed top symmetry which has never been observed in helium droplets before and has no physical justification. Therefore the origin for the substructure can not be explained with a rotational fine structure.

Comparable to the two lowest energy modes with their similar fine structure with respect to the electronic origin and the triplet substructure of the first line, the vibrational transitions at $\bar{\nu}_{rel} = 301.7 \text{ cm}^{-1}$ and 711.8 cm^{-1} stand out concerning their rather large line widths of 0.76 cm^{-1} and 0.66 cm^{-1} respectively. Except for the first two vibrational transitions, all lines were fitted with a Lorentzian confirming the dominance of homogeneous effects. The results for the line widths $\Delta\bar{\nu}_L$ are given in table 7.1. The respective life times τ were calculated by using $\tau = \frac{1}{2\pi c \Delta\bar{\nu}_L}$ and listed in table 7.1 as well. Overall, the line widths range from 0.15 cm^{-1} to 1.5 cm^{-1} corresponding to life times $35.4 \text{ ps} \geq \tau \geq 3.5 \text{ ps}$. At this, a general trend of increasing life times with increasing excitation energy can be noticed.

In summary, the fluorescence excitation spectrum of FBP, exhibiting sharp lines, just a minor solvent shift and almost no shift of the vibrational transitions with regard to the isolated molecules, seems quite undisturbed by the superfluid droplet environment.

7.1.2 Dispersed emission of FBP

Figure 7.5 displays the dispersed emission spectrum of FBP which was recorded by excitation at the 0_0^0 -transition at 16312.4 cm^{-1} . Since this spectrum was corrected with a background spectrum taken with closed entrance slit of the spectrograph, an intense stray light signal is visible at the excitation frequency. Sharp lines are present throughout the dispersed emission spectrum.

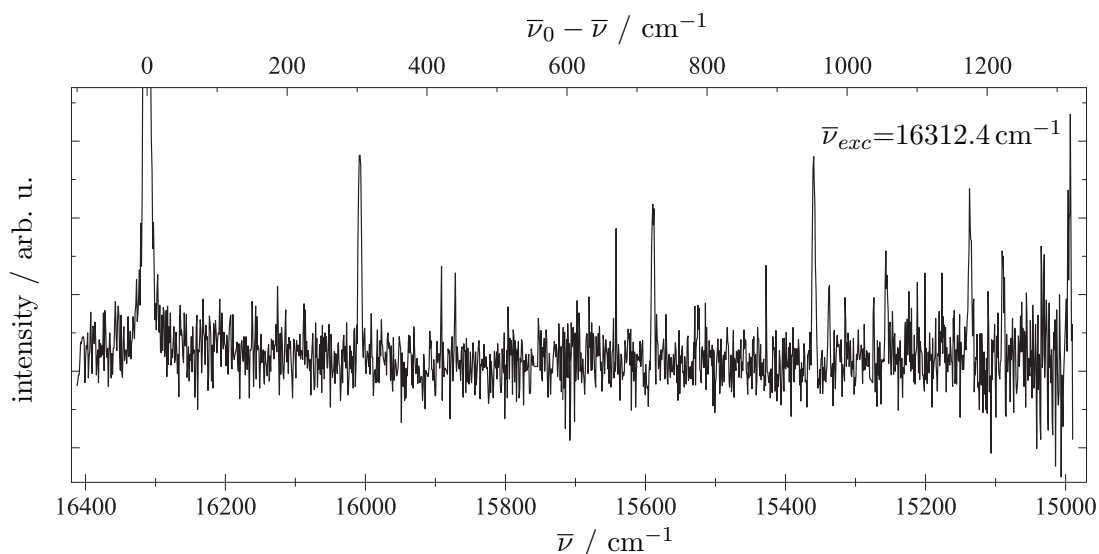


Fig. 7.5: Dispersed emission spectrum of FBP for excitation at 16312.4 cm^{-1} . The intense signal at the excitation frequency is predominantly due to laser stray light.

The vibronic transitions of FBP relative to the electronic origin $\bar{\nu}_{rel}(S_0) = \bar{\nu}_0 - \bar{\nu}$, corresponding to the vibrational modes of the electronic ground state, are listed in table 7.2. They are compared to the vibrational energies of the excited state $\bar{\nu}_{rel}(S_1^x) = \bar{\nu} - \bar{\nu}_0$. The deviation of the vibrational energies between S_0 and S_1^x in percent is listed in the last column of the table. As can be readily seen, there are only minor deviations within the magnitude of one percent. However, comparing the entirety of vibrational modes of S_0 (see table 7.2) with those of S_1^x (see table 7.1), several modes of the excitation spectrum are missing in the dispersed emission spectrum. Due to the rather poor signal-to-noise ratio of the emission spectrum, transitions with low

Tab. 7.2: List of vibronic transitions $\bar{\nu}$ obtained from the dispersed emission spectrum of FBP in superfluid helium droplets by excitation at the electronic origin ($\bar{\nu}_{exc} = 16312.4 \text{ cm}^{-1}$). The frequencies could be determined with an accuracy of 1 cm^{-1} (cf. chapter 4.1.3.2). In the second column $\bar{\nu}_{rel} (S_0)$ gives the frequencies relative to the electronic origin $\bar{\nu}_0 = 16312.4 \text{ cm}^{-1}$ corresponding to the vibrational transitions of the electronic ground state S_0 . For comparison, column three lists the vibrational transitions $\bar{\nu}_{rel} (S_1^x)$ of the electronically excited state S_1^x . $\Delta\bar{\nu}_{rel} (S_0 \text{ to } S_1^x)$ is the deviation in percent between the two values taking $\bar{\nu}_{rel} (S_0)$ as reference value.

$\bar{\nu} / \text{cm}^{-1}$	$\bar{\nu}_{rel} (S_0) / \text{cm}^{-1}$	$\bar{\nu}_{rel} (S_1^x) / \text{cm}^{-1}$	$\Delta\bar{\nu}_{rel} (S_0 \text{ to } S_1^x) / \%$
16312	0	0.0	0.0
16008	304	301.7	-0.8
15589	723	711.8	-1.5
15360	952	940.5	-1.2
15338	974	967.8	-0.6
15256	1056	1051.1	-0.5
15137	1175	[1162] ^a	-1.1
15089	1223	[1209] ^a	-1.1

^aGas phase data taken from ref. [106]. Accuracy of the frequencies relative to the electronic origin is $\pm 2 \text{ cm}^{-1}$.

intensity in the fluorescence excitation spectrum will obviously not be visible in the dispersed emission.

To summarize, the close similarity of the vibrational modes in S_0 and S_1^x (so-called: mirror symmetry) as observed for FBP indicates that only minor changes of the nuclear arrangement take place upon electronic excitation. Thus, FBP is a rather rigid molecule and therefore its spectroscopy is quite independent of the surrounding superfluid cryomatrix.

7.2 5,15-Diphenylporphyrin (DPP)

5,15-Diphenylporphyrin is a symmetrically methine substituted porphyrin (cf. fig. 7.6) which belongs to the point group S_4 .

As to our knowledge neither supersonic jet nor helium droplet experiments concerning DPP have been published. The same holds for low-temperature measurements of DPP in solid matrices.

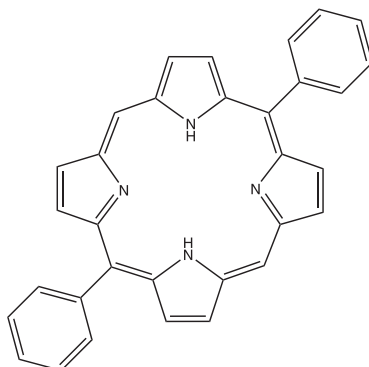


Fig. 7.6: Chemical structure of 5,15-diphenylporphyrin (DPP).

Fluorescence excitation of DPP was performed in the continuous helium droplet machine as well as with the pulsed source. The high-resolution investigation at the electronic origin was performed with the continuous setup using the continuous wave dye laser (Coherent Innova 899-29 autoscan) operated with DCM yielding an average power of 380 mW (measured directly behind the laser). A color glass filter RG665 (Schott) in front of the PMT was used to eliminate laser stray light. The heating voltage of the pick-up cell optimized for single doping of the droplets was 9.5 V corresponding to an oven temperature of approx. 245 °C. The expansion parameters were $p_0 = 30$ bar and $T_0 = 11.5$ K. Due to the lower laser power of the continuous wave dye laser, the vibronic transitions could not be recorded with the continuous source. Therefore, the excitation spectrum containing the vibronic transitions of DPP was recorded in the pulsed machine using the Nd:YAG pumped dye laser (Lambda Physik Scanmate 2E) operated at 20 Hz with rhodamine B yielding

an average power of 1.0 mJ/pulse. The dye laser was operated with resonator and preamplifier but without amplifier. Stagnation conditions for the pulsed valve were $p_0 = 80$ bar and $T_0 = 21.5$ K. The color glass filter in front of the PMT and the heating voltage of the pick-up oven were the same as in the continuous experiment.

7.2.1 Fluorescence excitation of DPP

The fluorescence excitation spectrum of DPP recorded with the pulsed helium droplet source is shown in figure 7.7. All signals are normalized to the most intense signal at $\bar{\nu}_0 = 15979.7$ cm⁻¹ which is assigned to the electronic origin. Sharp transitions dominated by the ZPLs are present throughout the spectrum.

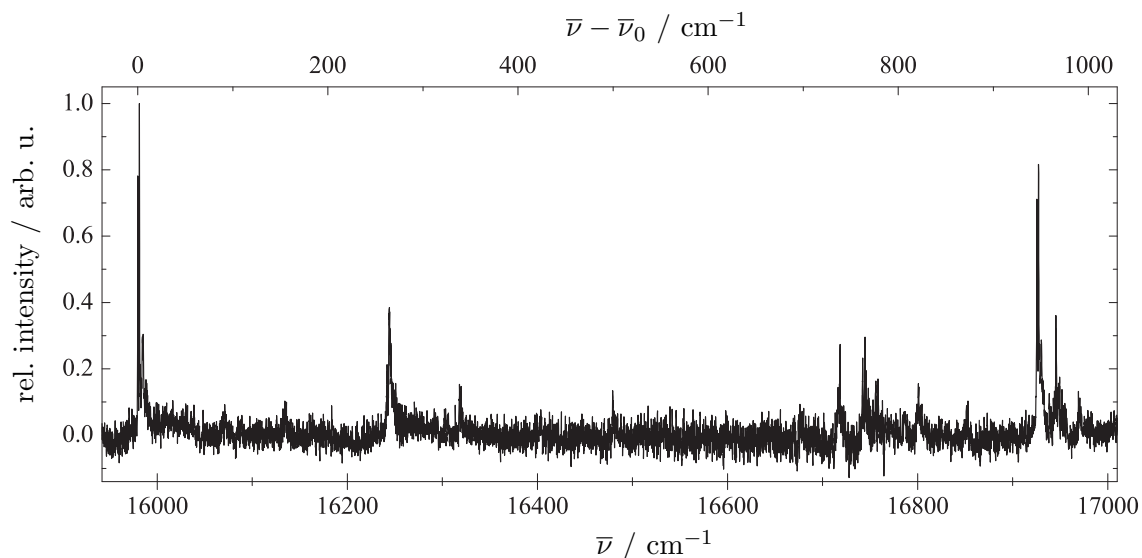


Fig. 7.7: Fluorescence excitation spectrum of DPP measured with the pulsed helium droplet source normalized to the most intense signal of the electronic origin at $\bar{\nu}_0 = 15979.7$ cm⁻¹.

The electronic origin of DPP is displayed in figure 7.8 (top panel) along with the electronic origin of FBP (bottom panel). Both spectra were measured with the continuous helium droplet setup. Apart from a doubling of all lines and slightly decreased line widths, DPP exhibits the same spectral structure of the electronic origin, an

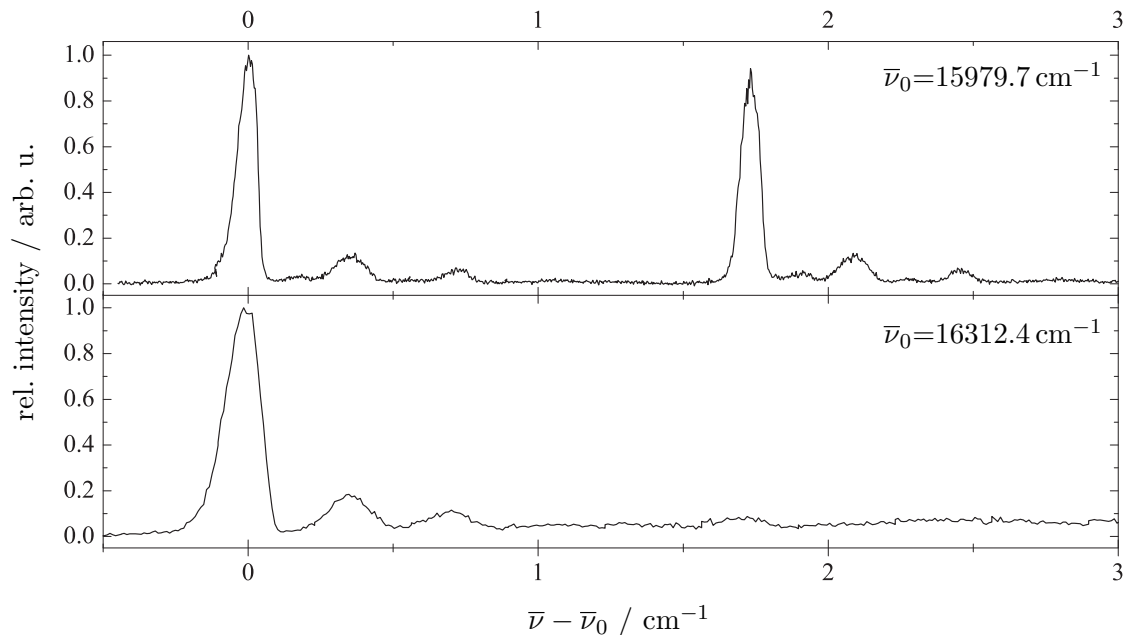


Fig. 7.8: Normalized fluorescence excitation spectra of DPP (top panel) and FBP (bottom panel) displaying the respective electronic origin.

intense line followed by two rather weak signals, as was observed for FBP in helium droplets (see chapter 7.1.1). However, in the case of DPP, additional, though very weak signals are recognizable between the three signals defining the porphyrin origin. The similarity of the electronic origins of both, DPP and FBP, leads to the conclusion that this spectral feature is a signature mark of the porphyrin core system solvated in superfluid helium droplets which is upon pure electronic excitation only slightly perturbed by adding two phenyl substituents to the porphyrin macrocycle.

Comparing the electronic origin of DPP recorded with different laser intensities (see figure 7.9), namely in the pulsed source (red spectrum) and with the continuous setup (black spectrum), reveals that apart from the already discussed splitting into two sharp signal groups a weaker spectral feature covering approximately 3 cm^{-1} within the range of $\bar{\nu}_{rel} = \bar{\nu} - \bar{\nu}_0 = 4 \text{ cm}^{-1}$ up to $\bar{\nu}_{rel} = 7 \text{ cm}^{-1}$ exists. Both spectra are normalized to the first intense signal respectively. It becomes apparent that while the two sharp signals seem independent of the laser intensity, the broad and structureless signal clearly depends on the laser intensity. The obviously different saturation

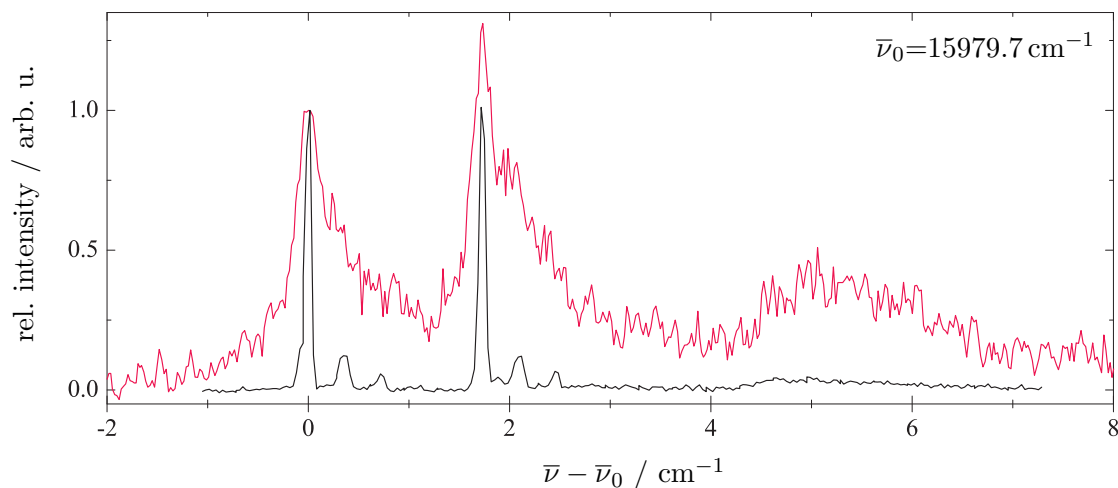


Fig. 7.9: Normalized fluorescence excitation spectra of the electronic origin of DPP measured with different laser intensities: with the continuous wave laser in the continuous helium droplet machine (black) and with the pulsed laser in the pulsed setup (red).

behaviour leads to assignment of the sharp signals belonging to the ZPL whereas the weaker signal belongs to the PW (cf. chapter 3.1.2).

The doubling of the ZPL of DPP with a line distance of $\sim 1.8 \text{ cm}^{-1}$, not only displayed in the electronic origin but also in various vibronic transitions (cf. table 7.3 and figure 7.10), is tentatively assigned to the excitation of different conformers of DPP. Taking into account the crystal structure of 5,10,15,20-tetraphenylporphyrin where the phenyl substituents were determined to be rotated out of the porphyrin plane by about 60° [113], those two conformers are imagined to have, in one case, the same torsional angle of both phenyl groups respective to the porphyrin macrocycle, i.e. the phenyl groups are parallel to each other, while the other case features tilted phenyl groups with respect to each other. To test for these stable ground state configurations dispersed emission spectra would provide helpful information. Unfortunately, although many attempts were made to record dispersed emission spectra of DPP by excitation at any of the intense signals at the electronic origin, these efforts remained unsuccessful. This may be due to the very weak fluorescence quantum yield as can be estimated from the signal-to-noise ratio in figure 7.7.

Table 7.3 gives an overview of the vibronic transitions $\bar{\nu}$ of the fluorescence excitation spectrum of DPP. Listed are the vibrational energies $\bar{\nu}_{rel}$ which are compared

Tab. 7.3: List of vibronic transitions obtained from the fluorescence excitation spectrum of DPP in superfluid helium droplets. Absolute line positions $\bar{\nu}$ could be determined with an accuracy of 1 cm^{-1} . $\bar{\nu}_{rel}$ indicates the frequency shift relative to the electronic origin at $\bar{\nu}_0 = 15979.7 \text{ cm}^{-1}$ (determined by measurements with the continuous setup). (s) denotes a clearly resolved splitting with a line distance of about 1.8 cm^{-1} as observed for the electronic origin. $\Delta\bar{\nu}_L$ are the Lorentzian line widths. τ gives the corresponding life times. $\bar{\nu}_{rel,FBP}$ are the transition frequencies of FBP relative to the electronic origin in helium droplets at 16312.4 cm^{-1} accompanied by the life times τ_{FBP} of the respective vibrational modes (cf. section 7.1.1 table 7.1).

$\bar{\nu} / \text{cm}^{-1}$	$\bar{\nu}_{rel} / \text{cm}^{-1}$	$\Delta\bar{\nu}_L / \text{cm}^{-1}$	τ / ps	$\bar{\nu}_{rel,FBP} / \text{cm}^{-1}$	τ_{FBP} / ps
15979.7	0 (s)	-	-	0	-
16069	89 (s)	-	-	85.4	-
16135	155	1.8(8)	2.9	147.5	3.5
16242	262	1.4(6)	3.8	301.7	7.0
16244	264	-	-	-	-
16318	338 (s)	1.7(5)	3.1	-	-
16479	499	0.7(3)	7.6	-	-
16718	738	-	-	726.1	13.3
16742	762	1.0(3)	5.3	-	-
16745	765	-	-	-	-
16756	776 (s)	1.0(3)	5.3	782.4	5.9
16801	821	-	-	-	-
16926	946 (s)	0.7(1)	7.6	940.5	17.7
16946	966	-	-	967.8	21.2
16970	990	-	-	992.1	35.4

with the respective vibrational energies of FBP $\bar{\nu}_{rel,FBP}$ in helium droplets (cf. section 7.1.1 table 7.1) given in the last column. An (s) accompanying the vibrational energy indicates that the transition shows a line splitting similar as observed for the electronic origin (cf. figure 7.8). $\Delta\bar{\nu}_L$ are the line widths resulting from a Lorentzian fit. The corresponding life times τ are given as well. Also the life times for vibrational modes of FBP τ_{FBP} are listed for comparison.

Regarding the vibrational energies of DPP compared to those of FBP, one finds that in the low frequency region up to 300 cm^{-1} as well as for higher vibrational modes with vibrational energies $\bar{\nu}_{rel} > 780\text{ cm}^{-1}$ good agreement can be found. Contrarily, additional signals appear for DPP between 300 cm^{-1} and 780 cm^{-1} compared

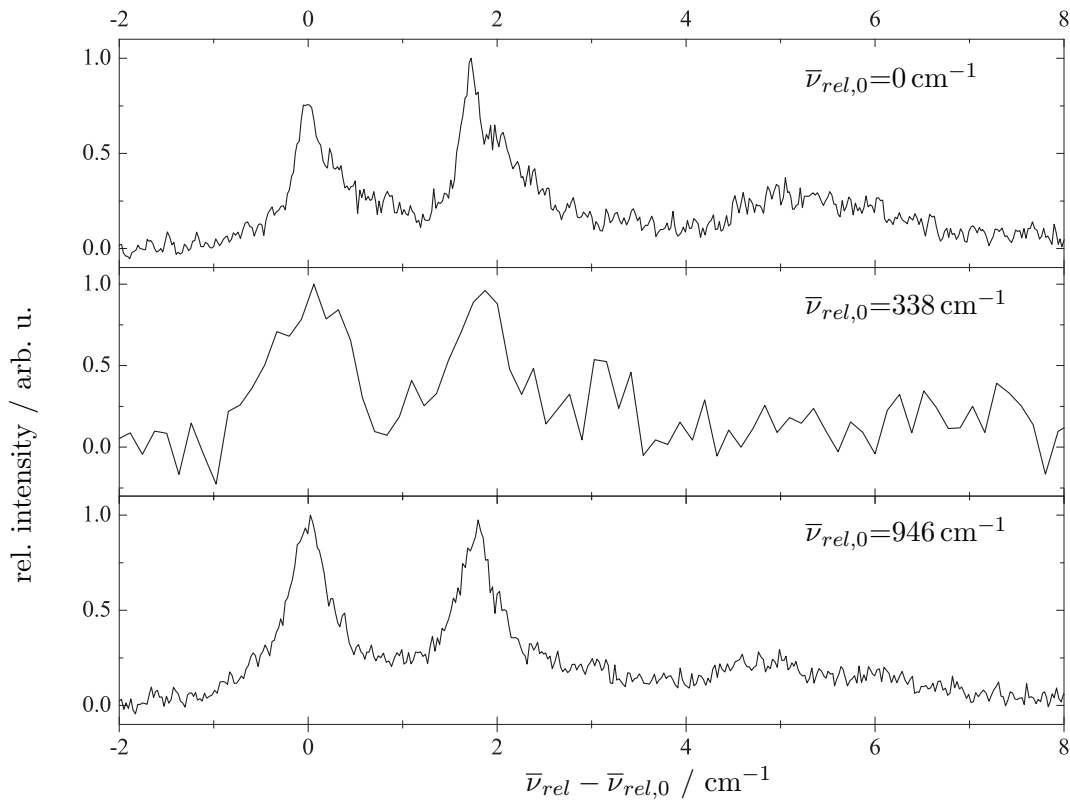


Fig. 7.10: Fluorescence excitation spectra of DPP showing the electronic origin at 15979.7 cm^{-1} (top panel) and two vibrational transitions at $\bar{\nu}_{rel} = 338\text{ cm}^{-1}$ and 946 cm^{-1} (middle and bottom panel). All graphs are normalized to the respective transition intensity.

to the bare chromophore system of FBP. This finding is presumably due to the lower symmetry of DPP (S_4) compared to FBP (D_{2h}) and these modes are therefore tentatively assigned to be related with the phenyl substituents and accordingly the meso carbon atoms. Comparing the life times of DPP and FBP results in systematically shorter life times for the phenyl-substituted porphyrin (cf. table 7.3). This finding can be explained by faster internal vibrational redistribution facilitated by the phenyl groups.

In contrast to previous investigations on phenyl-substituted anthracene [11], DPP shows no drastic line broadening in its fluorescence excitation spectrum although torsional motion of the phenyl groups which were thought to be causing the line broadening in the case of the substituted anthracene should be present as well.

7.3 5,10,15,20-Tetraphenylchlorin (TPC)

As depicted in figure 7.11, 5,10,15,20-tetraphenylporphyrin (compound 1) is a methine substituted porphyrin with D_{2h} symmetry. It is shown along with its reduced derivative, the corresponding chlorin with one hydrogenated bond within the pyrrole macrocycle compared to the porphyrin, namely 5,10,15,20-tetraphenylchlorin (fig. 7.11 compound 2) which possesses C_{2v} symmetry.

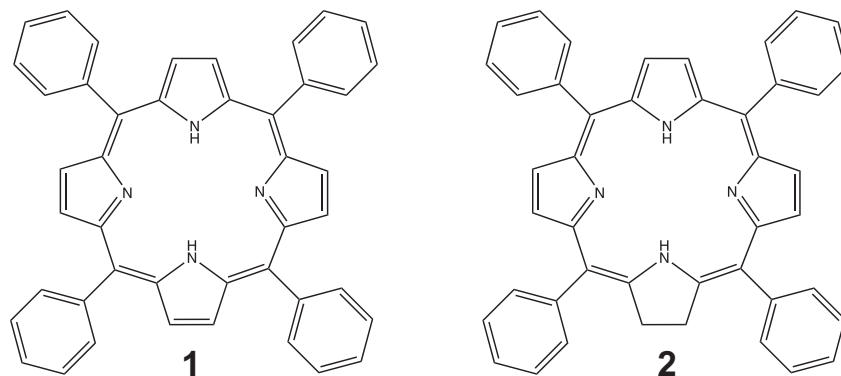


Fig. 7.11: Chemical structure of 5,10,15,20-tetraphenylporphyrin (TPP) (compound 1) and 5,10,15,20-tetraphenylchlorin (TPC) (compound 2).

For 5,10,15,20-tetraphenylporphyrin an oscillator strength of $f = 0.029$ is reported [114] while the values for the fluorescence quantum yield in the literature range from $\Phi_f = 0.11 - 0.13$ [114, 115, 116] along with a triplet quantum yield of 0.39 [117]. Using the statement that free-base porphyrins are usually six times less fluorescent than the corresponding chlorins [118], one can readily calculate the fluorescence quantum yield of 5,10,15,20-tetraphenylchlorin as $\Phi_f \approx 0.7 - 0.8$.

It should be noted that, although the initial aim was the investigation of 5,10,15,20-tetraphenylporphyrin (TPP), the recorded data point to the conclusion that excitation and emission spectra of 5,10,15,20-tetraphenylchlorin (TPC) were taken. This assumption will be discussed in detail in the following section. Additionally, HPLC analyses were performed on our TPP and TPC samples [74] and revealed that both samples consist of two species which can be identified as TPP and TPC according to their UV-VIS absorption spectra (cf. appendix).

Fluorescence excitation of TPC and TPP samples was performed in the continuous helium droplet machine as well as with the pulsed source. Additionally, dispersed emission spectra were recorded in the continuous droplet beam. The high-resolution investigation at the electronic origin was performed with the continuous setup using the continuous wave dye laser (Coherent Innova 899-29 autoscan) operated with DCM yielding an average power of 270 mW (measured directly behind the laser). A color glass filter RG665 (Schott) in front of the PMT was used to eliminate laser stray light. The heating voltage of the pick-up cell optimized for single doping of the droplets was 10.5 V corresponding to an oven temperature of approx. 260 °C. The expansion parameters were $p_0 = 30$ bar and $T_0 = 11.5$ K. Due to the lower laser power of the continuous wave dye laser, the vibronic transitions could not be recorded with the continuous source. Therefore, the excitation spectrum containing the vibronic transitions of TPC was recorded in the pulsed machine using the XeCl excimer laser pumped dye laser (Lambda Physik LPD 3002) operated at 50 Hz with sulforhodamine B yielding an average power of 1.5 mJ/pulse. Stagnation conditions for the pulsed valve were $p_0 = 80$ bar and $T_0 = 23$ K. The color glass filter in front of the PMT and the heating voltage of the pick-up oven were the same as in the continuous experiment.

7.3.1 Fluorescence excitation of TPC

The fluorescence excitation spectrum of TPC obtained with the pulsed helium droplet source is displayed in figure 7.12. Apart from the higher signal level it is identical to that obtained with our TPP sample. All signals are normalized to the most intense signal at 15586.4 cm^{-1} . Sharp ZPLs accompanied by intense PWs are present throughout the spectrum. The intense PW signals are due to saturation effects in the ZPLs. However, the excitation laser was not attenuated on purpose to gain enough laser power to record the weak vibronic transitions of TPC.

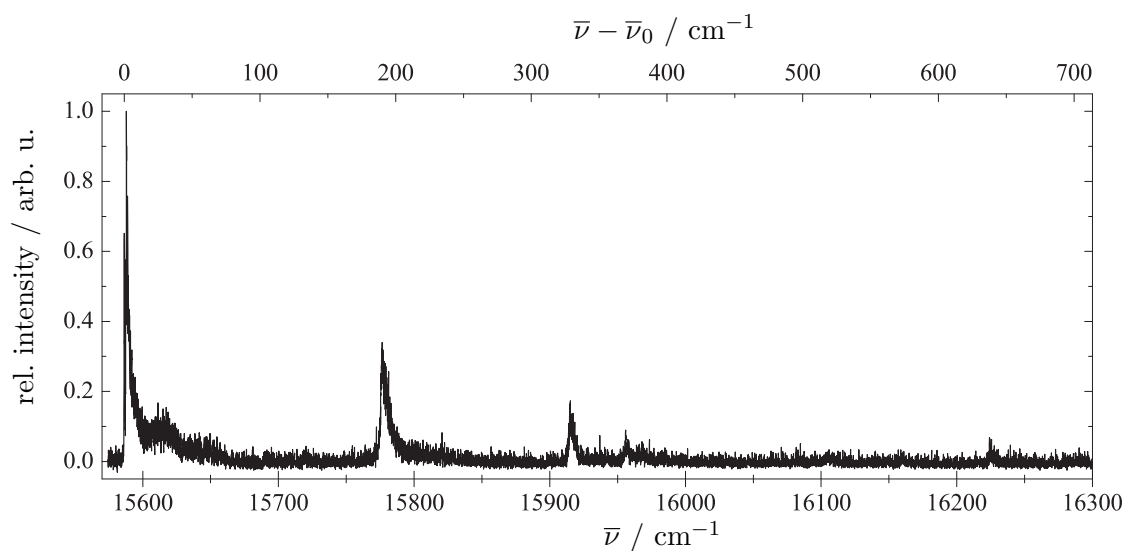


Fig. 7.12: Fluorescence excitation spectrum of TPC measured with the pulsed helium droplet source.

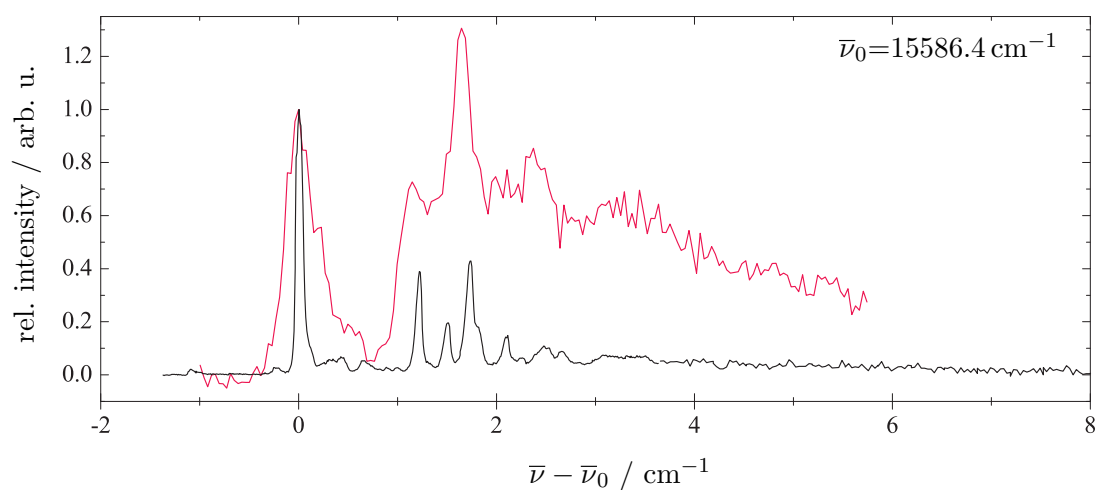


Fig. 7.13: Normalized fluorescence excitation spectra of the electronic origin of TPC measured with different laser intensities: with the continuous wave laser in the continuous helium droplet machine (black) and with the pulsed laser in the pulsed setup (red).

The most intense signal of the fluorescence excitation spectrum at $\bar{\nu}_0 = 15586.4 \text{ cm}^{-1}$ is assigned to the electronic origin of TPC. The high-resolution spectrum recorded with the continuous helium droplet beam is displayed in figure 7.13 (black) along with the corresponding highly saturated spectrum measured with the pulsed source (red). Both spectra are normalized to the most intense signal. The spectral fine structure of the electronic origin comprises one single intense line at $\bar{\nu}_0 = 15586.4 \text{ cm}^{-1}$. This is accompanied by two weak red shifted signals which are probably due to complexes with residual gas molecules. Moreover, blue shifted by $\bar{\nu}_{rel} = \bar{\nu} - \bar{\nu}_0 \approx 1 \text{ cm}^{-1}$ up to $\bar{\nu}_{rel} \approx 3 \text{ cm}^{-1}$ arises a group of sharp signals with different saturation behaviour than the most intense line. Thus, one can conclude that the single sharp signal belongs to the ZPL while the spectrally blue shifted group of sharp signals represents the PW.

A list of signals $\bar{\nu}$ extracted from the fluorescence excitation spectrum is given in table 7.4. The frequencies relative to the electronic origin of TPC $\bar{\nu}_{rel}$ are listed and compared to the respective vibrational modes $\bar{\nu}_{jet}$ relative to the electronic origin of TPP at $\bar{\nu}_{0,jet} = 15617 \pm 6 \text{ cm}^{-1}$ received in a supersonic jet experiment [119]. The shift $\bar{\nu}_{shift}$ between helium droplet and gas phase measurements is tabulated for each vibrational mode as well. Compared with the supersonic jet experiment [119] a solvent shift of 31 cm^{-1} to the red is observed by switching from the isolated molecule to the helium droplet environment. Apart from this solvent shift, taking into account the different accuracies in determining the laser wavelength (cf. footnote in table 7.4), good agreement is found between gas phase and helium droplet experiment. However, the two vibrational modes at $\bar{\nu}_{rel} = 370 \text{ cm}^{-1}$ and $\bar{\nu}_{rel} = 638 \text{ cm}^{-1}$ are absent in the supersonic jet experiment. Though they are present in the dispersed emission spectrum of TPC (cf. section 7.3.2 table 7.5). Moreover, the broad spectral signal in the helium droplet spectrum covering the spectral range from approximately $\bar{\nu}_{rel} = 19 \text{ cm}^{-1}$ up to $\bar{\nu}_{rel} = 44 \text{ cm}^{-1}$ is represented by four single lines in the supersonic jet (see table 7.4). These low-energy modes have been assigned to torsional excitations of the phenyl groups [119].

Tab. 7.4: List of vibronic transitions obtained from the fluorescence excitation spectrum of TPC in superfluid helium droplets. The line positions $\bar{\nu}$ could be determined with an accuracy of 1 cm^{-1} . $\bar{\nu}_{rel}$ indicates the frequency shift relative to the electronic origin at $\bar{\nu}_0 = 15586.4 \text{ cm}^{-1}$. $\bar{\nu}_{jet}$ are the corresponding data from reference [119] recorded in a supersonic jet. The last column gives the shift between the vibrational energies derived from the helium droplet experiment relative to the supersonic jet measurements.

$\bar{\nu} / \text{cm}^{-1}$	$\bar{\nu}_{rel} / \text{cm}^{-1}$	$\bar{\nu}_{jet}^a / \text{cm}^{-1}$	$\bar{\nu}_{shift} / \text{cm}^{-1}$
15586.4	0	0	0
15605 – 15630	19 – 44 (b) ^b	18, 22, 40, 43 (l) ^c	-
15775	189	191	-2
15915	329	331	-2
15956	370	-	-
15966	380	380	0
16224	638	-	-

^aData taken from ref. [119]. Accuracy of the frequencies relative to the electronic origin is $\pm 2 \text{ cm}^{-1}$.

^b(b) denotes a broad spectral feature.

^c(l) denotes single lines.

The fact that there is no obvious correlation with the FBP spectrum regarding the vibrational modes (cf. table 7.1) points – additionally to the result that spectra of our samples of TPP and TPC were identical and taking into account that the fluorescence quantum yield of chlorins is usually significantly higher than that of the corresponding porphyrin (cf. for example section 7.1) – to the conclusion that TPC instead of TPP was subject of investigation during this study as well as in the supersonic jet experiment reported in reference [119]. Following this interpretation the disturbance of vibrational modes is a result of the lower symmetry of TPC compared to FBP. But then, one could also explain the drastically changed vibrational mode structure caused by four additional phenyl substituents attached

to the porphyrin macrocycle which significantly increases the molecular mass.

However, investigating the sample of TPP in the continuous droplet beam revealed apart from the intense electronic origin a group of two weak and sharp signals which was also observed from the TPC sample. In figure 7.14 these signals (top panel) are compared to the electronic origin of DPP (bottom panel). Both spectra are normalized to the most intense signal. Although the distance of 2.8 cm^{-1} between the two signals is larger than in the case of DPP (cf. chapter 7.2.1) the spectral structure seems similar as far as can be judged due to the poor signal-to-noise ratio in the TPP spectrum. Another fact to support the assignment of the weak signal group to the electronic origin of TPP is a comparison of the red shift of the electronic origins relative to FBP. By adding two phenyl substituents to FBP ($\bar{\nu}_0 = 16312.4\text{ cm}^{-1}$) in order to obtain DPP ($\bar{\nu}_0 = 15979.7\text{ cm}^{-1}$) a spectral red shift of the electronic origin of $\bar{\nu}_{redshift} = 333\text{ cm}^{-1}$ is observed. Adding again two phenyl groups to end up with TPP, a red shift of the electronic origin of approximately

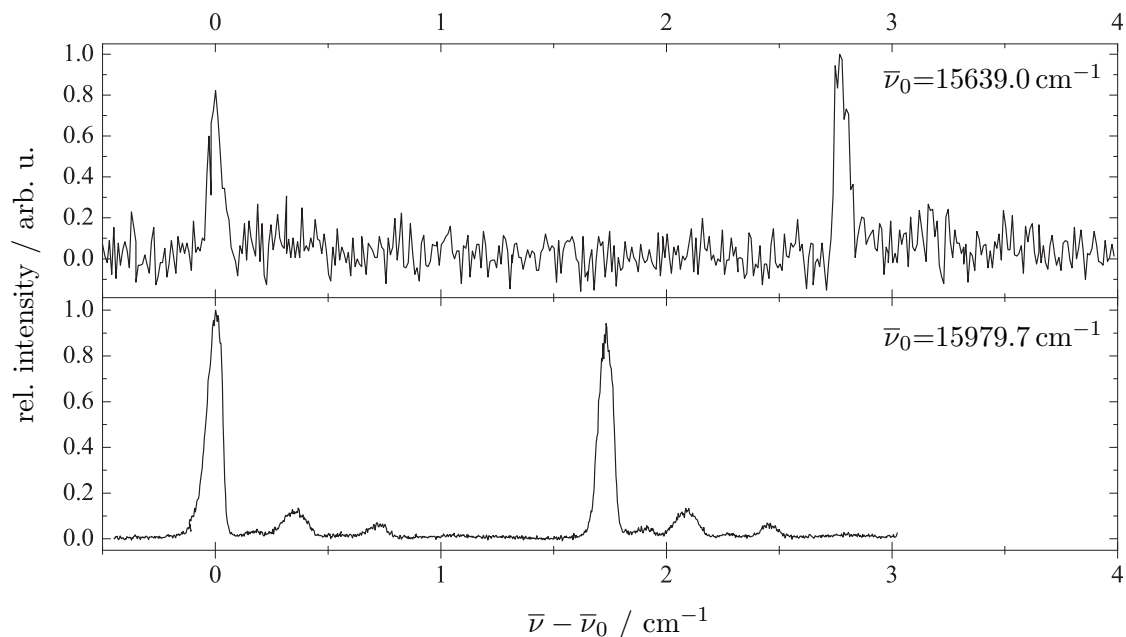


Fig. 7.14: Normalized fluorescence excitation spectra of TPP (top panel) and DPP (bottom panel) displaying the electronic origin of DPP and a similar signal group found in the spectrum of TPP. For details see text.

$\bar{\nu}_{redshift} = 666 \text{ cm}^{-1}$ would be expected. This fits quite well if one assumes that the signal group at $\bar{\nu}_0 = 15639.0 \text{ cm}^{-1}$ (cf. top panel of figure 7.14), corresponding to $\bar{\nu}_{redshift} = 673 \text{ cm}^{-1}$, represents the electronic origin of TPP.

7.3.2 Dispersed emission of TPC

The dispersed emission spectrum of TPC excited at the most intense signal of the electronic origin at 15586.4 cm^{-1} is displayed in figure 7.15. It is normalized to the most intense signal. The inset shows the region of the vibrational transitions magnified by a factor of 7. Since the spectrum was generated by subtracting a background spectrum that takes account of the laser stray light it can be readily seen that the fluorescence coincides with the excitation frequency. Furthermore, excitation at the different lines blue shifted by $\bar{\nu}_{rel} = 1 \text{ cm}^{-1}$ up to $\bar{\nu}_{rel} = 3 \text{ cm}^{-1}$ (see figure 7.13) results, apart from the signal level, in the same emission spectrum as shown in figure 7.15. This is expected for signals that belong to one species (cf. chapter 3.2) and confirms the assignment of ZPL and PW of the electronic origin (cf. section 7.3.1).

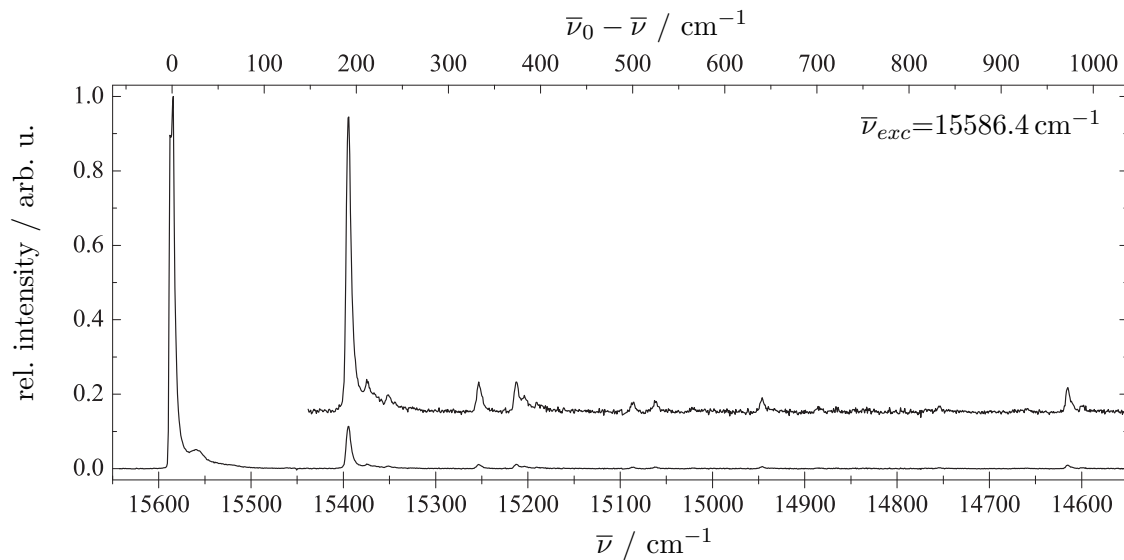


Fig. 7.15: Dispersed emission spectrum of TPC for excitation at 15586.4 cm^{-1} . The inset shows the region of the vibronic transitions magnified by a factor of 7.

Tab. 7.5: Vibronic transitions $\bar{\nu}$ obtained from the dispersed emission spectrum of TPC in superfluid helium droplets by excitation at the electronic origin ($\bar{\nu}_{exc} = 15586.4 \text{ cm}^{-1}$). The frequencies could be determined with an accuracy of 1 cm^{-1} (cf. chapter 4.1.3.2). $\bar{\nu}_{rel} (S_0)$ gives the frequencies relative to the electronic origin corresponding to the vibrational transitions of S_0 . For comparison, column three lists the vibrational transitions of the electronically excited state $\bar{\nu}_{rel} (S_1^x)$. $\Delta\bar{\nu}_{rel} (S_0 \text{ to } S_1^x)$ is the deviation in percent between the two values taking $\bar{\nu}_{rel} (S_0)$ as reference value.

$\bar{\nu} / \text{cm}^{-1}$	$\bar{\nu}_{rel} (S_0) / \text{cm}^{-1}$	$\bar{\nu}_{rel} (S_1^x) / \text{cm}^{-1}$	$\Delta\bar{\nu}_{rel} (S_0 \text{ to } S_1^x) / \%$
15586	0	0	0.0
15561	25	19 – 44 (b) ^a	-
15395	191	189	-1.1
15374	212	[208] ^b	-1.9
15352	234	[236] ^b	+0.8
15253	333	329	-1.2
15213	373	370	-0.8
15205	381	380	-0.3
15191	395	[398] ^b	+0.8
15087	499	[507] ^b	+1.6
15062	524	[530] ^b	+1.1
14946	640	638	-0.3
14885	701	[700] ^b	-0.1
14754	832	[824] ^b	-1.0
14615	971	[971] ^b	0.0
14600	986	[986] ^b	0.0

^a(b) denotes a broad spectral feature (cf. figure 7.12 and table 7.4)

^bGas phase data taken from ref. [119]. Accuracy of the frequencies relative to the electronic origin is $\pm 2 \text{ cm}^{-1}$.

Table 7.5 lists all signals $\bar{\nu}$ derived from the dispersed emission spectrum along with the vibrational energies of the electronic ground state $\bar{\nu}_{rel}(S_0) = \bar{\nu}_0 - \bar{\nu}$. For comparison, the third column gives the vibrational energies of the excited state $\bar{\nu}_{rel}(S_1^x)$. The deviation of the vibrational energies between S_0 and S_1^x in percent is listed in the last column of the table. As can be readily seen, there are only minor deviations within the magnitude of less than two percent.

Throughout the dispersed emission spectrum sharp lines are present with the electronic origin dominating in the intensity followed by an intense vibrational mode at $\bar{\nu}_{rel} = 191 \text{ cm}^{-1}$ (cf. figure 7.15). The energetically higher modes up to $\bar{\nu}_{rel} \approx 1000 \text{ cm}^{-1}$ are comparably weak. Due to the fact that the intensity of transitions in the emission spectrum reflects the respective Franck-Condon factors one can conclude that the molecule's geometry change following the electronic excitation is negligible since the electronic origin is the dominating signal.

To summarize, the close similarity of the vibrational modes in S_0 and S_1^x (so-called: mirror symmetry) which is observed for TPC indicates that only minor changes of the nuclear arrangement take place upon electronic excitation. In contrast to previous investigations on phenyl-substituted anthracene [11], TPC shows no drastic line broadening in its fluorescence excitation spectrum although torsional motion of the phenyl groups should be allowed. Thus, by comparing with the respective supersonic jet experiment, the spectroscopy of TPC is found to be quite independent of the surrounding superfluid cryomatrix.

7.4 5,10,15,20-Tetramethylporphyrin (TMP)

5,10,15,20-tetramethylporphyrin (TMP) is, as the previously discussed TPP, a methine substituted porphyrin with D_{2h} symmetry. Its structural formula is depicted in figure 7.16. As to our knowledge neither supersonic jet nor helium droplet experiments concerning TMP have been published. The same holds for low-temperature measurements of TMP in solid matrices.

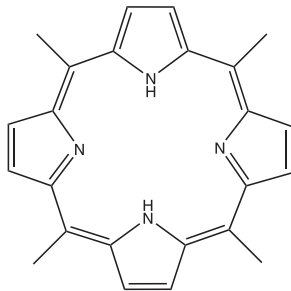


Fig. 7.16: Chemical structure of 5,10,15,20-tetramethylporphyrin (TMP).

Fluorescence excitation of TMP was performed in the continuous helium droplet machine as well as with the pulsed source. Additionally, dispersed emission spectra were recorded in the continuous droplet beam. The high-resolution investigations at the electronic origin were performed with the continuous setup using the continuous wave dye laser (Coherent Innova 899-29 autoscan) operated with DCM yielding an average power of 200 mW (measured directly behind the laser). A color glass filter RG695 (Schott) in front of the PMT was used to eliminate laser stray light. The heating voltage of the pick-up cell optimized for single doping of the droplets was 10.0 V corresponding to an oven temperature of approx. 256 °C. The expansion parameters were $p_0 = 25$ bar and $T_0 = 11.6$ K. Due to the lower laser power of the continuous wave dye laser, the vibronic transitions could not be recorded with the continuous source. Therefore, the excitation spectrum containing the vibronic transitions of TMP was recorded in the pulsed machine using the Nd:YAG pumped dye laser (Lambda Physik Scanmate 2E) operated at 20 Hz with DCM yielding an average power of 12 mJ/pulse. Stagnation conditions for the pulsed valve were

$p_0 = 80$ bar and $T_0 = 21.5$ K. The color glass filter in front of the PMT and the heating voltage of the pick-up oven were the same as in the continuous experiment.

7.4.1 Fluorescence excitation of TMP

The fluorescence excitation spectrum of TMP recorded with the pulsed source is displayed in figure 7.17. It is normalized to the most intense signal at 15046 cm^{-1} . The spectrum is dominated by intense PWs with sharp ZPLs at the rising side. Even with substantial attenuation of the excitation laser the PWs clearly dominate over the signal intensity of the ZPLs. However, the spectrum shown in figure 7.17 was measured without attenuating the excitation laser to ensure that as many vibrational modes as possible become visible in the fluorescence excitation spectrum.

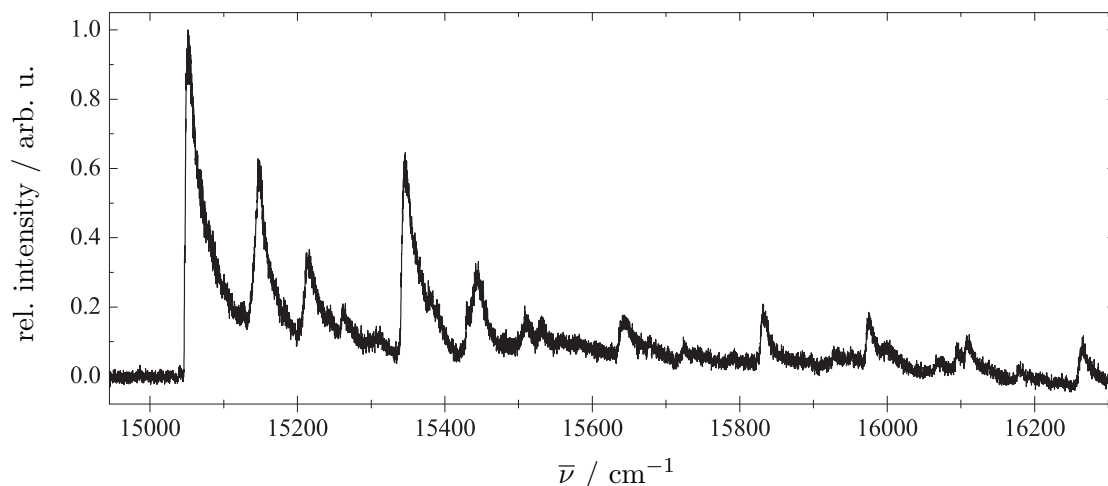


Fig. 7.17: Fluorescence excitation spectrum of TMP measured with the pulsed helium droplet source. The spectrum is normalized to the most intense signal at 15046 cm^{-1} .

As will be discussed further in section 7.4.2 two electronic origins could be identified within the excitation spectrum of the TMP sample. High-resolution measurements of the two origins recorded in the continuous helium droplet beam are displayed in figures 7.18 and 7.19. The spectral structure originating at $\bar{\nu}_0 = 15429.4\text{ cm}^{-1}$ (see

figure 7.18) shows two sharp intense lines accompanied by a couple of weak and also sharp signals. It presents a similar fine structure as found for the electronic origins of FBP, DPP and TPC (cf. chapters 7.1.1, 7.2.1 and 7.3.1).

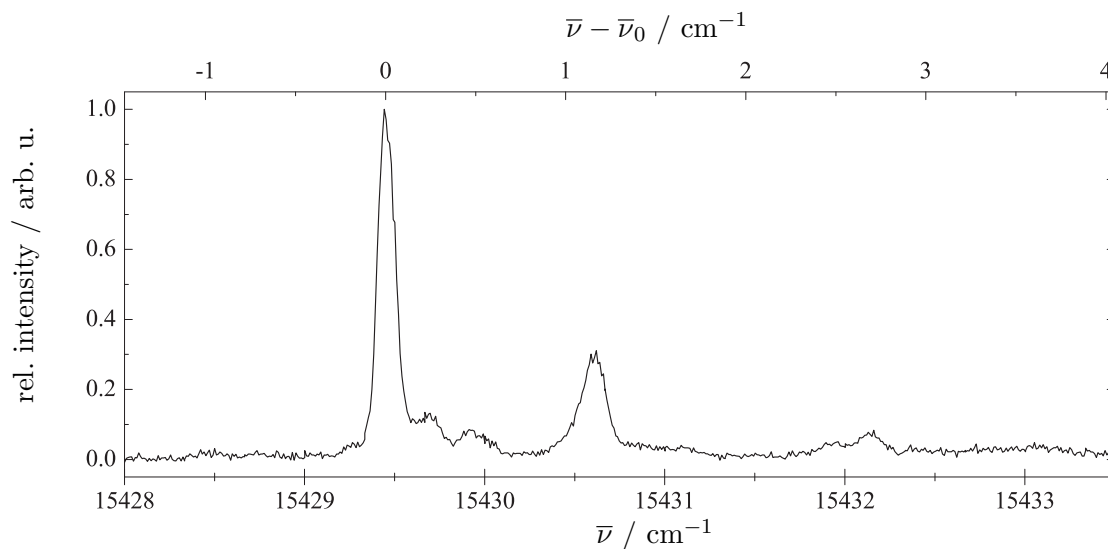


Fig. 7.18: Fluorescence excitation spectrum of TMP measured with the continuous setup normalized to the most intense signal.

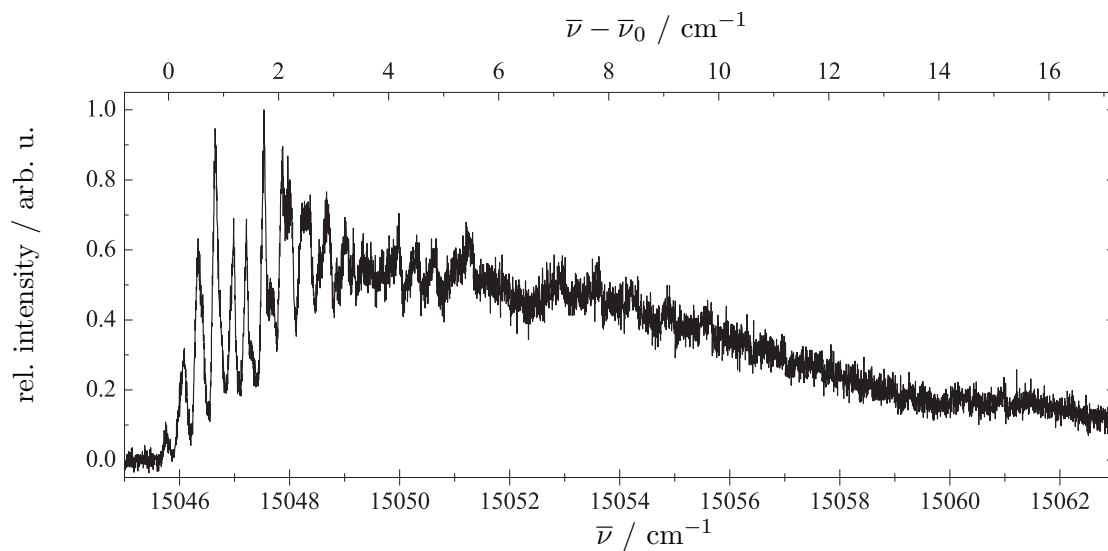


Fig. 7.19: Fluorescence excitation spectrum of TMP measured with the continuous setup normalized to the most intense signal.

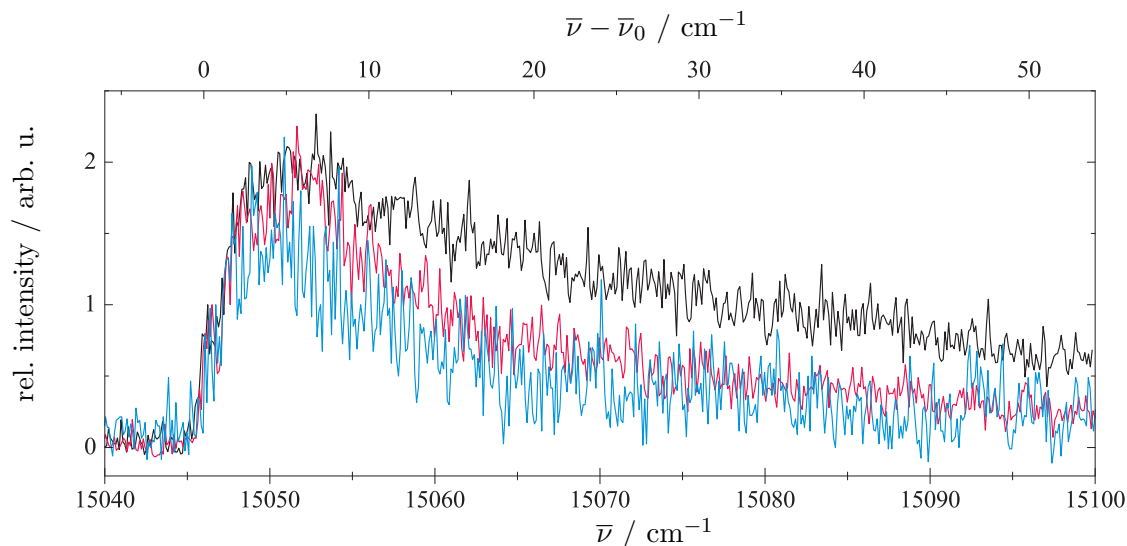


Fig. 7.20: Fluorescence excitation spectrum of TMP measured with the pulsed setup with different laser powers, precisely non-attenuated laser (black), attenuated laser by inserting one (red) or two (blue) lens cleaning tissues into the laser beam. All spectra are normalized to the signal at 15046 cm^{-1} .

However, the spectral feature originating at $\bar{\nu}_0 = 15045.8 \text{ cm}^{-1}$ which is illustrated in figure 7.19 presents an unusual spectral shape which has to our knowledge never been observed before in an excitation spectrum of organic molecules in superfluid helium droplets. A series of at least ten sharp lines separated by about 0.3 cm^{-1} from each other is shown. The intensity is increasing from the first to the fourth and finally the sharp lines merge into a broad unstructured band. Experiments with different laser powers were conducted with the continuous and the pulsed source to investigate the saturation behaviour of this spectral fine structure. While the measurements with the continuous wave laser remained inconclusive concerning an assignment of ZPL and PW, the data recorded with the pulsed apparatus reveal a different saturation behaviour at the rising side compared to the broad spectral feature to the blue. The latter finding is illustrated in figure 7.20 where the excitation spectrum taken with non-attenuated laser (black) as well as with attenuated laser by inserting one (red) or two (blue) lens cleaning tissues into the laser beam path is depicted. All spectra are normalized to the signal at 15046 cm^{-1} . Consequently,

Tab. 7.6: List of vibronic transitions obtained from the fluorescence excitation spectrum of TMP in superfluid helium droplets. The absolute line positions $\bar{\nu}$ could be determined with an accuracy of 1 cm^{-1} . $\bar{\nu}_{rel} (15045.8)$ and $\bar{\nu}_{rel} (15429.4)$ indicate the frequency shift relative to the electronic origin at $\bar{\nu}_0 = 15045.8 \text{ cm}^{-1}$ and $\bar{\nu}_0 = 15429.4 \text{ cm}^{-1}$ (both determined by measurements with the continuous setup). $\bar{\nu}_{rel,FBP}$ are the transition frequencies of FBP relative to the electronic origin in helium droplets at 16312.4 cm^{-1} (cf. section 7.1.1, table 7.1). All data are given in cm^{-1} . For more details see text.

$\bar{\nu}$	$\bar{\nu}_{rel} (15045.8)$	$\bar{\nu}_{rel} (15429.4)$	$\bar{\nu}_{rel,FBP}$	$\bar{\nu}_{rel,FBP}$
15045.8	0	-384	0	-
15138	92	-292	85.4	-
15207	161	-223	147.5	-
15258	212	-172	-	-
15340	294	-90	301.7	-
15429.5	384	0	-	0
15504	458	75	-	85.4
15526	480	97	-	-
15636	590	207	-	-
15724	678	295	-	301.7
15828	782	399	782.4	-
15970	924	541	936.6	-
16066	1020	637	-	-
16093	1047	664	1051.1	-
16106	1060	677	1054.2	-
16176	1130	747	[1162] ^a	726.1
16259	1213	830	[1209] ^a	-

^aGas phase data taken from ref. [106]. Accuracy of the frequencies relative to the electronic origin is $\pm 2 \text{ cm}^{-1}$.

the broad spectral feature is assigned to the PW. Although, due to the low spectral resolution of the pulsed measurement, it remains unclear where exactly the PW begins and which of the sharp lines belong to the ZPL. Yet, an electronic origin where ZPL and PW with comparable intensity merge seamlessly into each other has never been observed before in experiments using continuous wave lasers as excitation source for organic molecules in superfluid helium droplets. However, for experiments with pulsed lasers intense PWs that dominate over ZPLs have been observed before [24, 25, 120]. Intense PWs indicate different solvation configurations in S_0 and S_1 which are probably due to nuclear rearrangement – in the case of TMP via torsional motions of the methyl groups – initiated by the electronic excitation as was discussed in references [11, 24, 25, 64].

A list of all transitions observed in the fluorescence excitation spectrum recorded with the pulsed setup is given in table 7.6. Since there are two electronic origins present in our TMP spectrum, apart from the absolute signal positions $\bar{\nu}$, relative frequencies $\bar{\nu}_{rel} = \bar{\nu} - \bar{\nu}_0$ are tabulated considering both origins at $\bar{\nu}_0 = 15045.8 \text{ cm}^{-1}$ and $\bar{\nu}_0 = 15429.4 \text{ cm}^{-1}$ in column two and three, respectively. For reasons of comparison, column four and five indicate the transition frequencies of FBP $\bar{\nu}_{rel,FBP}$ relative to the electronic origin at 16312.4 cm^{-1} (cf. section 7.1.1). At this, column four gives the frequencies for comparison with the $\bar{\nu}_{rel}$ (15045.8 cm^{-1}) values and column five the frequencies for comparison with the $\bar{\nu}_{rel}$ (15429.4 cm^{-1}) values. It should be noted that not all vibrational modes of FBP are listed but only those that fit to the respective transitions of TMP. For both origins similar agreement is found with the vibrational modes of FBP up to $\bar{\nu}_{rel} \approx 780 \text{ cm}^{-1}$. However, additional modes are present within the spectral range from $\bar{\nu}_{rel} \approx 300 \text{ cm}^{-1}$ up to $\bar{\nu}_{rel} \approx 700 \text{ cm}^{-1}$. These are presumably related to the methine carbon atoms or accordingly the addition of four methyl groups.

7.4.2 Dispersed emission of TMP

The identification of two electronic origins within the fluorescence excitation spectrum of TMP (see figures 7.18 and 7.19) as discussed in the previous section was achieved by taking dispersed emission spectra. The emission spectrum for excitation at $\bar{\nu}_{exc} = 15429.4 \text{ cm}^{-1}$ is shown in figure 7.21. It was recorded by subtracting a background spectrum that takes account of the laser stray light (cf. chapter 4.1.3.2) and is normalized to the most intense signal which coincides with the excitation frequency. The inset shows the region of the vibrational transitions magnified by a factor of 10. It should be noted that the dispersed emission spectrum recorded upon excitation at $\bar{\nu}_{exc} = 15430.6 \text{ cm}^{-1}$, the second intense line shown in the excitation spectrum in figure 7.18 displays identical transition frequencies as shown in figure 7.21.

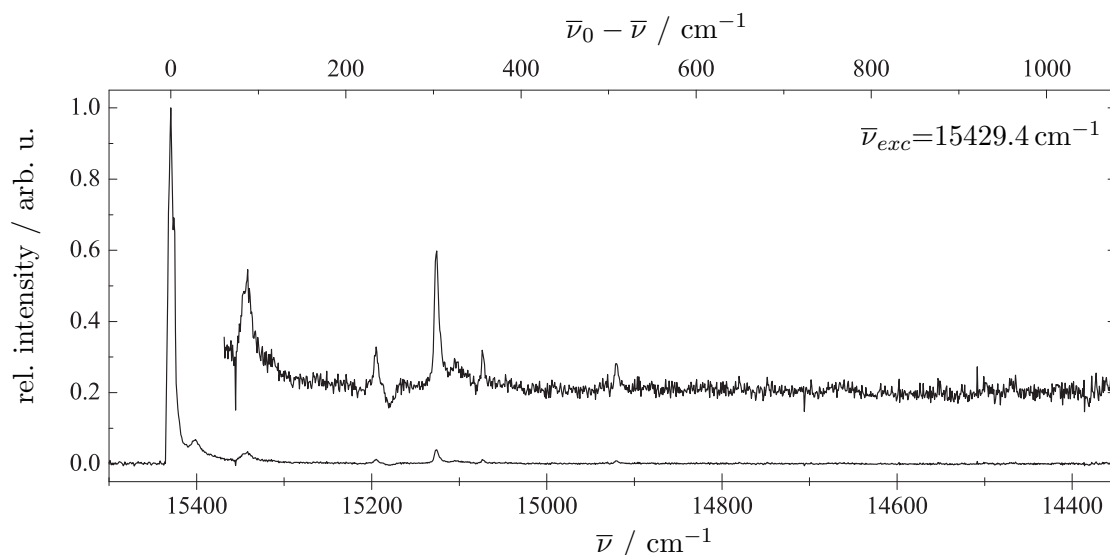


Fig. 7.21: Dispersed emission spectrum of TMP for excitation at 15429.4 cm^{-1} . The inset shows the region of the vibronic transitions magnified by a factor of 10.

Table 7.7 lists the sharp signals $\bar{\nu}$ present throughout the dispersed emission spectrum by excitation at 15429.4 cm^{-1} . The frequencies relative to the electronic origin $\bar{\nu}_{rel}(S_0) = \bar{\nu}_0 - \bar{\nu}$ at $\bar{\nu}_0 = 15429 \text{ cm}^{-1}$ corresponding to the vibrational modes of S_0 are also given together with the respective values $\bar{\nu}_{rel}(S_1^x)$ of the electronically

excited state. It becomes obvious that agreement is found between the vibrational mode patterns in S_0 and S_1 . However, the deviations between the $\bar{\nu}_{rel}$ (S_0) and $\bar{\nu}_{rel}$ (S_1^x) values are large with up to 13%. This reflects the problem of identifying the ZPLs of vibronic transitions exhibiting low signal-to-noise levels (cf. figure 7.17), rather than a change of the intramolecular binding conditions in S_0 and S_1 .

Tab. 7.7: Vibronic transitions $\bar{\nu}$ obtained from the dispersed emission spectrum of TMP in superfluid helium droplets by excitation at the electronic origin ($\bar{\nu}_{exc} = 15429.4 \text{ cm}^{-1}$). The frequencies could be determined with an accuracy of 1 cm^{-1} (cf. chapter 4.1.3.2). In the second column $\bar{\nu}_{rel}$ (S_0) gives the frequencies relative to the electronic origin $\bar{\nu}_0 = 15429 \text{ cm}^{-1}$ corresponding to the vibrational transitions of S_0 . For comparison, column three lists the vibrational transitions $\bar{\nu}_{rel}$ (S_1^x) of the electronically excited state S_1^x . $\Delta\bar{\nu}_{rel}$ (S_0 to S_1^x) is the deviation in percent between the two values taking $\bar{\nu}_{rel}$ (S_0) as reference value.

$\bar{\nu} / \text{cm}^{-1}$	$\bar{\nu}_{rel}$ (S_0) / cm^{-1}	$\bar{\nu}_{rel}$ (S_1^x) / cm^{-1}	$\Delta\bar{\nu}_{rel}$ (S_0 to S_1^x) / %
15429	0	0	0.0
15402	27	-	-
15343	86	97	+12.8
15195	234	207	-11.5
15126	303	295	-2.6
15073	356	399	+12.1
14920	509	541	+6.3

Because of the low signal intensity in the fluorescence excitation spectrum it was not possible to record a dispersed emission spectrum of TMP by exciting at the first sharp line within the electronic origin at $\bar{\nu}_{exc} = 15045.8 \text{ cm}^{-1}$ (cf. figure 7.19). Therefore emission spectra were taken upon excitation at $\bar{\nu}_{exc} = 15046.6 \text{ cm}^{-1}$ and $\bar{\nu}_{exc} = 15047.5 \text{ cm}^{-1}$. Apart from the signal level they were identical. The dispersed emission spectrum of TMP recorded upon excitation at $\bar{\nu}_{exc} = 15047.5 \text{ cm}^{-1}$ is

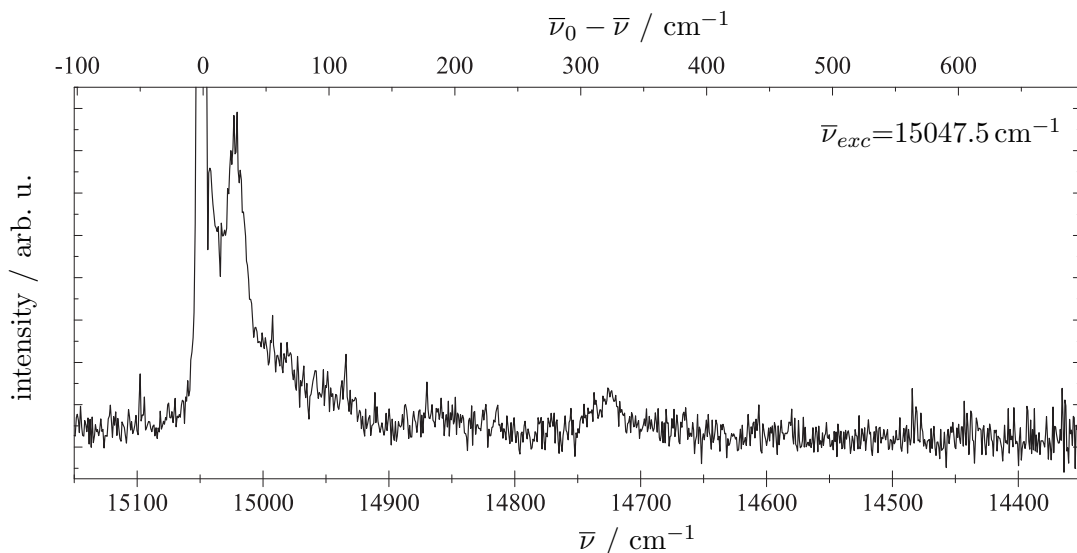


Fig. 7.22: Dispersed emission spectrum of TMP for excitation at 15047.5 cm^{-1} . The intense signal at the excitation frequency is predominantly due to laser stray light.

shown in figure 7.22. Since this spectrum was corrected with a background spectrum taken with closed entrance slit of the spectrograph, an intense stray light signal is visible at the excitation frequency. Aside from the intense signal at the excitation frequency two transitions are present. Their line positions $\bar{\nu}$ are listed in table 7.8 along with $\bar{\nu}_{rel}(S_0)$, the wavenumbers relative to the electronic origin at $\bar{\nu}_{exc} = 15046 \text{ cm}^{-1}$. These values correspond to the vibrational modes of S_0 and are compared to the values of the electronically excited state $\bar{\nu}_{rel}(S_1^x)$ extracted from the fluorescence excitation spectrum. Judging the agreement of the vibrational mode patterns in S_0 and S_1 is not straightforward since, owing to the low signal-to-noise ratio in the dispersed emission spectrum, only two signals are present.

To summarize, obviously at least two different species are present within our TMP sample. A finding which has been confirmed by HPLC analysis [74]. Although one component could be identified as TMP on the basis of its UV-VIS absorption spectrum, due to the low signal-to-noise ratio of the absorption spectrum the origin of the second component remains unidentifiable and could stem from the corresponding chlorin. However, a shift of the electronic origin of 384 cm^{-1} for the

Tab. 7.8: List of vibronic transitions $\bar{\nu}$ obtained from the dispersed emission spectrum of TMP in superfluid helium droplets by excitation at $\bar{\nu}_{exc} = 15047.5 \text{ cm}^{-1}$. The frequencies could be determined with an accuracy of 1 cm^{-1} (cf. chapter 4.1.3.2). In the second column $\bar{\nu}_{rel} (S_0)$ gives the frequencies relative to the electronic origin $\bar{\nu}_0 = 15046 \text{ cm}^{-1}$ corresponding to the vibrational transitions of the electronic ground state S_0 . For comparison, column three lists the vibrational transitions $\bar{\nu}_{rel} (S_1^x)$ of the electronically excited state S_1^x . $\Delta\bar{\nu}_{rel} (S_0 \text{ to } S_1^x)$ is the deviation in percent between the two values taking $\bar{\nu}_{rel} (S_0)$ as reference value.

$\bar{\nu} / \text{cm}^{-1}$	$\bar{\nu}_{rel} (S_0) / \text{cm}^{-1}$	$\bar{\nu}_{rel} (S_1^x) / \text{cm}^{-1}$	$\Delta\bar{\nu}_{rel} (S_0 \text{ to } S_1^x) / \%$
15046	0	0	0.0
15023	27	-	-
14724	326	294	-9.8

electronic origin of TMP compared to the corresponding chlorin seems too large considering $\sim 53 \text{ cm}^{-1}$ for the spectral distance between the proposed electronic origins of TPP and TPC (cf. chapter 7.3.1). To decide which of the two origins may be assigned to TMP one should take into account that, on the one hand, the spectral fine structure of the electronic origin at $\bar{\nu}_0 = 15429.4 \text{ cm}^{-1}$ exhibits closer similarity with the other porphyrin species investigated during this study than the origin at $\bar{\nu}_0 = 15045.8 \text{ cm}^{-1}$. On the other hand, good agreement is found for the vibrational modes of both electronic origins compared to those of FBP (cf. table 7.6). Finally, the dispersed emission spectrum recorded upon excitation at $\bar{\nu}_{exc} = 15429.4 \text{ cm}^{-1}$ exhibits good mirror symmetry with the fluorescence excitation spectrum. Yet, it is difficult to judge the agreement for vibrational modes of S_0 and S_1 in case of the emission spectrum upon excitation at $\bar{\nu}_0 = 15047.5 \text{ cm}^{-1}$ due to the poor signal-to-noise ratio. Altogether, a final assignment of one of the two electronic origins to TMP based on the available data seems difficult and this issue will therefore be left open.

7.5 5,10,15,20-Tetrapropylporphyrin (TPrP)

5,10,15,20-tetrapropylporphyrin (TPrP) is like the previously discussed porphyrin species DPP, TPP and TMP a methine substituted porphyrin. Its structural formula is depicted in figure 7.23. As to our knowledge neither supersonic jet nor helium droplet experiments concerning TPrP have been published. Though, low-temperature measurements at 4.2 K in solid matrices have been published [121, 122], however, with a lower spectral resolution compared to the present study.

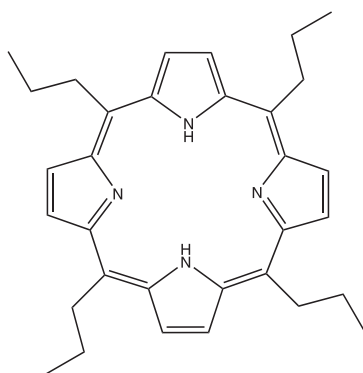


Fig. 7.23: Chemical structure of 5,10,15,20-tetrapropylporphyrin (TPrP).

Fluorescence excitation of TPrP was performed in the continuous helium droplet machine as well as with the pulsed source. Additionally, dispersed emission spectra were recorded in the continuous droplet beam. The high-resolution investigations at the electronic origin were performed with the continuous setup using the continuous wave dye laser (Coherent Innova 899-29 autoscan) operated with DCM yielding an average power of 240 mW (measured directly behind the laser). A color glass filter RG695 (Schott) in front of the PMT was used to eliminate laser stray light. The heating voltage of the pick-up cell optimized for single doping of the droplets was 7.0 V corresponding to an oven temperature of approx. 157 °C. The expansion parameters were $p_0 = 20$ bar and $T_0 = 12.3$ K. Due to the lower laser power of the continuous wave dye laser it was difficult to record the vibronic transitions with the continuous source. Therefore, the excitation spectrum containing the vibronic

transitions of TPrP was recorded in the pulsed machine using the Nd:YAG pumped dye laser (Lambda Physik Scanmate 2E) operated at 20 Hz with DCM yielding an average power of 12 mJ/pulse. Stagnation conditions for the pulsed valve were $p_0 = 80$ bar and $T_0 = 22.5$ K. The color glass filter in front of the PMT and the heating voltage of the pick-up oven were the same as in the continuous experiment.

7.5.1 Fluorescence excitation of TPrP

A moderately resolved fluorescence excitation spectrum of TPrP recorded with the pulsed helium droplet source is displayed in the top panel of figure 7.24. It is normalized to the most intense signal. The weak signal around 15115 cm^{-1} may be due to complexation with impurities of residual gas molecules in the vacuum chamber. For comparison the fluorescence spectrum of FBP is given in the bottom panel of figure 7.24.

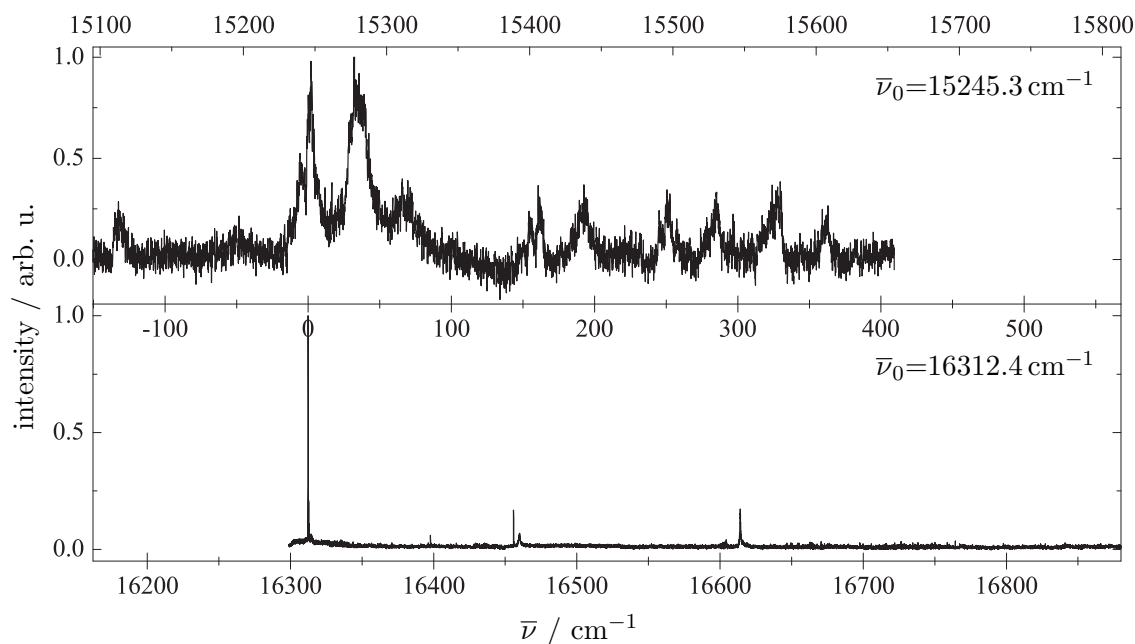


Fig. 7.24: Fluorescence excitation spectrum of TPrP measured with the pulsed source (top panel) and FBP recorded with the continuous helium droplet setup (bottom panel).

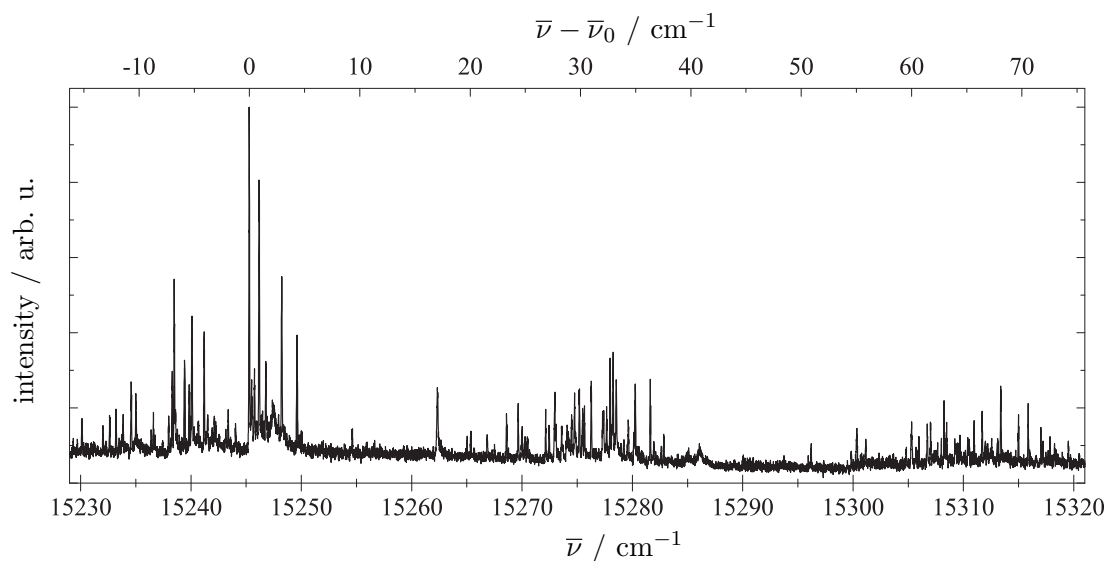


Fig. 7.25: Fluorescence excitation spectrum of TPrP measured with the continuous helium droplet source.

The spectral region from 15230 cm^{-1} up to 15320 cm^{-1} measured in the continuous setup is presented in figure 7.25. It reveals a large number of sharp lines which are not resolved in the pulsed experiment (cf. top panel of figure 7.24). Moreover, comparison of pulsed and continuous helium droplet experiment regarding the fluorescence intensity ratios of various signal groups clearly reveals saturation effects in the pulsed experiment.

From the experiments conducted in the continuous machine one electronic origin including one corresponding vibrational mode could be identified based on the spectral fine structure. Figure 7.26 displays in the top panel the electronic origin at $\bar{\nu}_0 = 15245.3\text{ cm}^{-1}$ and in the bottom panel the vibrational mode at $\bar{\nu}_{rel} = \bar{\nu} - \bar{\nu}_0 = 168.2\text{ cm}^{-1}$. Obviously, the electronic origin itself is defined by several sharp lines of which two are dominating. This structure may indicate different solvation isomers either due to differing conformers of TPrP or due to different solvation shell structures. The spectral fine structure of the electronic origin is with similar line width, namely about $\Delta\bar{\nu}_L = 0.10\text{ cm}^{-1}$ for the first intense signal at $\bar{\nu}_{rel} = 0\text{ cm}^{-1}$ and $\Delta\bar{\nu}_L = 0.12\text{ cm}^{-1}$ for the line at $\bar{\nu}_{rel} = 0.9\text{ cm}^{-1}$, repeated in the

vibrational mode. These Lorentzian line widths correspond to life times of $\tau = 53$ ps and $\tau = 44$ ps, respectively.

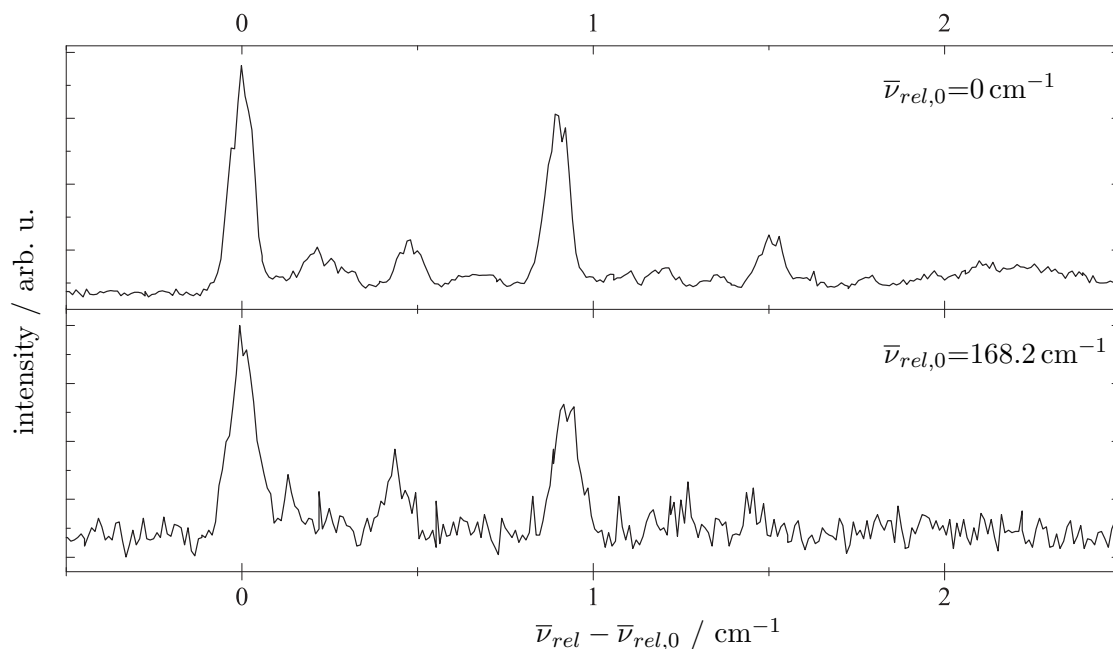


Fig. 7.26: Fluorescence excitation spectra of TPrP showing the electronic origin at 15245.3 cm^{-1} (top panel) and one vibronic transition (bottom panel).

Due to the numerous lines revealed by the continuous measurements which yielded in broad signals in the pulsed experiment, only rough estimates of spectral positions $\bar{\nu}$ for entire groups of signals are given in table 7.9. $\bar{\nu}_{rel}$ denotes the frequency relative to the electronic origin at $\bar{\nu}_0 = 15245.3 \text{ cm}^{-1}$ as determined from the measurements with the continuous source. They are compared to the transition frequencies of FBP $\bar{\nu}_{rel,FBP}$ (cf. chapter 7.1.1).

Since HPLC analysis revealed the presence of at least six components within our TPrP sample (cf. appendix) [74], presumably many of the sharp lines visible in the spectra taken with the continuous helium droplet setup are due to impurities. This makes a comparison with vibrational modes of FBP difficult and may explain the rather poor agreement with the vibrational transitions of the porphyrin core system (see table 7.9). But then, a considerably large mass is added to the porphyrin macro-

cycle by the four propyl substituents which could also be a reasonable explanation for significant changes within the vibrational mode structure of TPrP compared to FBP.

Tab. 7.9: List of vibronic transitions obtained from the fluorescence excitation spectrum of TPrP in superfluid helium droplets. The positions $\bar{\nu}$ are, if not stated otherwise, only rough indications for the position of entire signal groups. $\bar{\nu}_{rel}$ indicates the frequency shift relative to the electronic origin at $\bar{\nu}_0 = 15245.3 \text{ cm}^{-1}$ as determined from measurements in the continuous droplet beam. $\bar{\nu}_{rel,FBP}$ are the transition frequencies of FBP relative to the electronic origin in helium droplets at 16312.4 cm^{-1} (cf. section 7.1.1, table 7.1).

$\bar{\nu} / \text{cm}^{-1}$	$\bar{\nu}_{rel} / \text{cm}^{-1}$	$\bar{\nu}_{rel,FBP} / \text{cm}^{-1}$
15245.3 ^a	0	0
15277	37	-
15310	70	85.4
15413.5 ^a	168.2	147.5
15437	197	-
15496	256	-
15528	288	-
15568	328	301.7
15608	368	-

^aThe accurate line position was determined from the continuous droplet experiment.

7.5.2 Dispersed emission of TPrP

Due to the low signal-to-noise ratio in the fluorescence excitation spectrum dispersed emission spectra of TPrP were only recorded by excitation at the two most intense signals of the excitation spectrum, namely 15245.3 cm^{-1} and 15246.2 cm^{-1} (cf. top panel of figure 7.26). Apart from the signal level the derived dispersed emission spectra were identical. Exemplarily, the dispersed emission spectrum for excitation

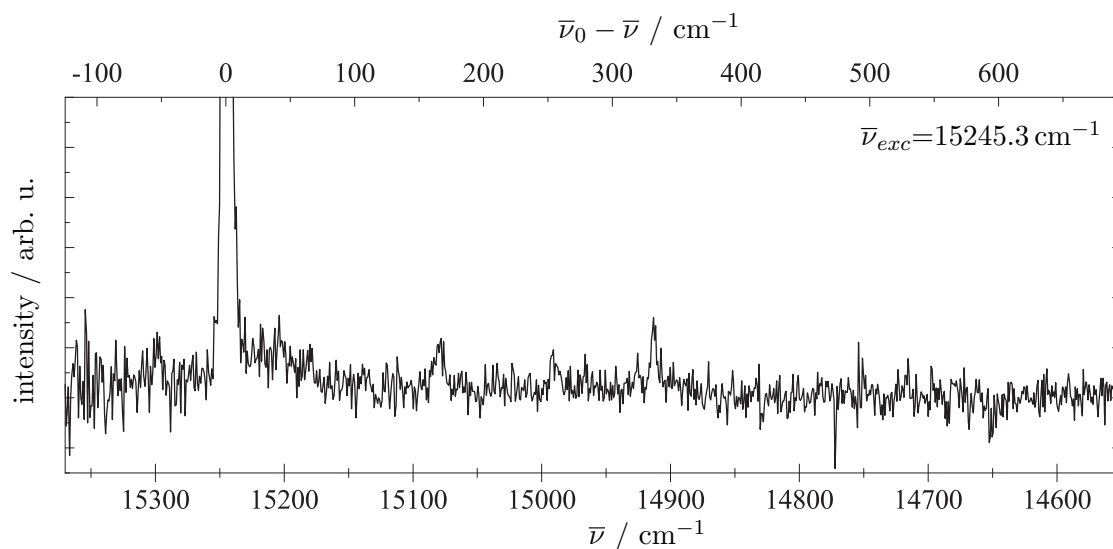


Fig. 7.27: Dispersed emission spectrum of TPrP for excitation at 15245.3 cm^{-1} . The intense signal at the excitation frequency is predominantly due to laser stray light.

at $\bar{\nu}_{exc} = 15245.3 \text{ cm}^{-1}$ is shown in figure 7.27. Apart from the intense signal at the excitation frequency which is mainly due to laser stray light since this spectrum was corrected with a background spectrum taken with closed entrance slit of the spectrograph, it displays three sharp transitions.

The frequencies $\bar{\nu}$ extracted from the emission spectrum are tabulated in table 7.10 along with the frequencies relative to the electronic origin $\bar{\nu}_{rel}(S_0) = \bar{\nu}_0 - \bar{\nu}$ which correspond to the vibrational modes of the electronic ground state. They are compared to the respective transitions of the excited state $\bar{\nu}_{rel}(S_1^x)$. The juxtaposition of the vibrational modes of S_0 and S_1^x thus allows to assign three transitions of the fluorescence excitation spectrum to the electronic origin at $\bar{\nu}_0 = 15245.3 \text{ cm}^{-1}$.

In summary, although assignment to a certain species remains impossible due to the various components within our TPrP sample, one can still conclude that – despite adding rather flexible propyl substituents to the porphyrin macrocycle which certainly enable lots of torsional modes – sharp transitions are present throughout the fluorescence excitation and dispersed emission spectrum. This finding indicates that the molecular structure remains unchanged following electronic excitation.

Tab. 7.10: List of vibronic transitions $\bar{\nu}$ obtained from the dispersed emission spectrum of TPrP in superfluid helium droplets by excitation at $\bar{\nu}_{exc} = 15245.3 \text{ cm}^{-1}$. The frequencies could be determined with an accuracy of 1 cm^{-1} (cf. chapter 4.1.3.2). In the second column $\bar{\nu}_{rel} (S_0)$ gives the frequencies relative to the electronic origin $\bar{\nu}_0 = 15245.3 \text{ cm}^{-1}$ corresponding to the vibrational modes of the electronic ground state S_0 . For comparison, column three lists the vibrational modes $\bar{\nu}_{rel} (S_1^x)$ of the electronically excited state S_1^x . $\Delta\bar{\nu}_{rel} (S_0 \text{ to } S_1^x)$ is the deviation in percent between the two values taking $\bar{\nu}_{rel} (S_0)$ as reference value.

$\bar{\nu} / \text{cm}^{-1}$	$\bar{\nu}_{rel} (S_0) / \text{cm}^{-1}$	$\bar{\nu}_{rel} (S_1^x) / \text{cm}^{-1}$	$\Delta\bar{\nu}_{rel} (S_0 \text{ to } S_1^x) / \%$
15245	0	0	0.0
15080	165	168	+1.8
14990	255	256	+0.4
14913	332	328	-1.2

7.6 Etioporphyrin I (Etio)

In contrast to the previously discussed methine substituted porphyrins (see chapter 7.2 to 7.5) 2,7,12,17-Tetraethyl-3,8,13,18-tetramethylporphyrin or so-called etioporphyrin I (Etio) is a pyrrole substituted porphyrin with a fluorescence quantum yield of $\Phi_f \approx 0.06$ [123]. Its structural formula is shown in figure 7.28. As to our knowledge neither supersonic jet nor helium droplet experiments concerning Etio have been published.

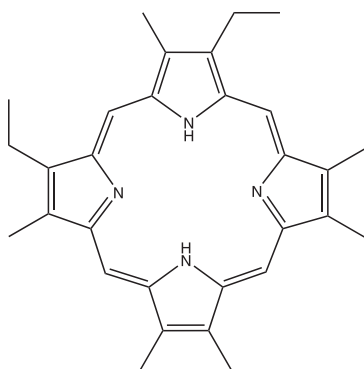


Fig. 7.28: Chemical structure of etioporphyrin I (Etio).

Fluorescence excitation of Etio was performed in the continuous helium droplet machine as well as with the pulsed source. Additionally, dispersed emission spectra were recorded in the continuous droplet beam. The high-resolution investigations at the electronic origin were performed with the continuous setup using the continuous wave dye laser (Coherent Innova 899-29 autoscan) operated with sulforhodamine B yielding an average power of 140 mW (measured directly behind the laser). A color glass filter RG665 (Schott) in front of the PMT was used to eliminate laser stray light. The heating voltage of the pick-up cell optimized for single doping of the droplets was 8.5 V corresponding to an oven temperature of approx. 194 °C. The expansion parameters were $p_0 = 25$ bar and $T_0 = 12.4$ K. Due to the lower laser power of the continuous wave dye laser, the vibronic transitions could not be recorded with the continuous source. Therefore, the excitation spectrum containing the vibronic

transitions of Etio was recorded in the pulsed machine using the Nd:YAG pumped dye laser (Lambda Physik Scanmate 2E) operated at 20 Hz with rhodamine 101 or rhodamine B yielding an average power of 1.0 mJ/pulse. The dye laser was operated with resonator and preamplifier but without amplifier. Stagnation conditions for the pulsed valve were $p_0 = 80$ bar and $T_0 = 22$ K. The color glass filter in front of the PMT and the heating voltage of the pick-up oven were the same as in the continuous experiment. HPLC analysis of our Etio sample revealed no impurities.

7.6.1 Fluorescence excitation of Etio

An overview spectrum of Etio measured in the pulsed helium droplet beam is displayed in figure 7.29. It is normalized to the most intense signal. A list of signals $\bar{\nu}$ derived from the fluorescence excitation spectrum along with the respective frequencies $\bar{\nu}_{rel} = \bar{\nu} - \bar{\nu}_0$ relative to the electronic origin at $\bar{\nu}_0 = 16108.1$ cm^{-1} is given in table 7.11. For comparison the vibrational frequencies of FBP $\bar{\nu}_{rel,FBP}$ are given as well. Although there are similarities to FBP regarding the vibrational modes at 127 cm^{-1} , 322 cm^{-1} and 723 cm^{-1} , adding eight alkyl substituents involving a

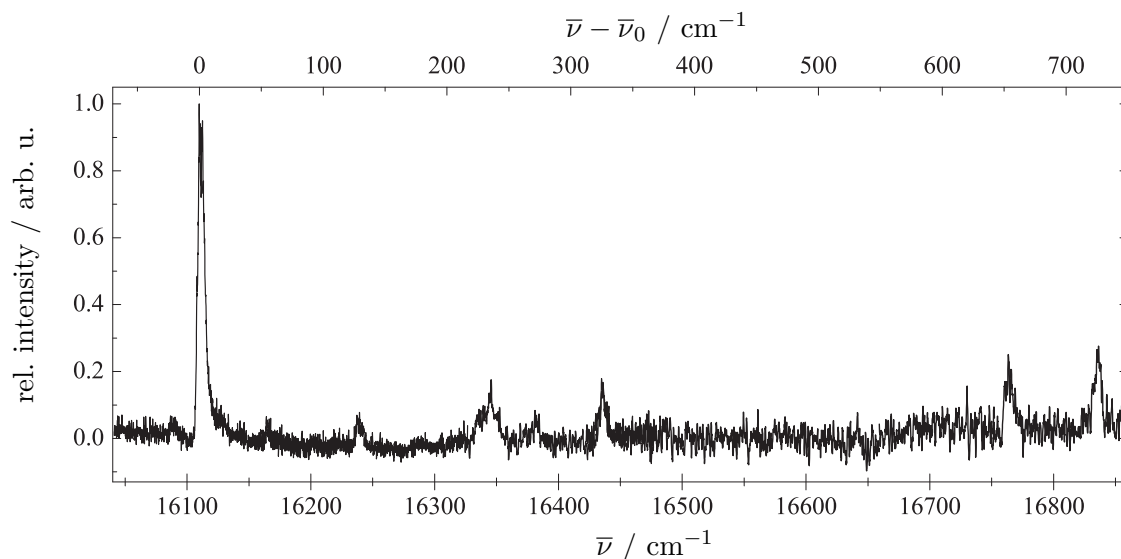


Fig. 7.29: Fluorescence excitation spectrum of Etio measured with the pulsed source normalized to the most intense signal at $\bar{\nu}_0 = 16108$ cm^{-1} .

Tab. 7.11: List of vibronic transitions obtained from the fluorescence excitation spectrum of Etio in superfluid helium droplets. Absolute line positions $\bar{\nu}$ could be determined with an accuracy of 1 cm^{-1} . $\bar{\nu}_{rel}$ indicates the frequency shift relative to the electronic origin at $\bar{\nu}_0 = 16108.1 \text{ cm}^{-1}$ as determined from measurements in the continuous droplet beam. $\bar{\nu}_{rel,FBP}$ are the transition frequencies of FBP relative to the electronic origin in helium droplets at 16312.4 cm^{-1} (cf. section 7.1.1, table 7.1).

$\bar{\nu} / \text{cm}^{-1}$	$\bar{\nu}_{rel} / \text{cm}^{-1}$	$\bar{\nu}_{rel,FBP} / \text{cm}^{-1}$
16108.1	0	0
16164	56	-
16235	127	143.4
16334	226	-
16381	273	-
16430	322	301.7
16761	653	-
16831	723	716.4

considerable mass increase obviously leads to significant disturbances of the vibrational modes of the tetrapyrrole macrocycle. Therefore the additional modes can tentatively be assigned to be caused by the methyl and ethyl substituents.

A high-resolution fluorescence excitation spectrum of the electronic origin of Etio recorded with the continuous source is shown in figure 7.30. It is normalized to the most prominent signal at 16108.1 cm^{-1} and consists of a series of six sharp intense and numerous weak lines. Interestingly, every intense signal is followed by at least one weak signal. Measurements with different laser intensities left the question about an assignment to ZPL or PW for the different signals displayed in figure 7.30 inconclusive since all lines seem to have the same saturation behaviour within the intensity range of the continuous wave laser. Two effects can be responsible for the multitude of lines. On the one hand, the structural formula of the Etio molecule

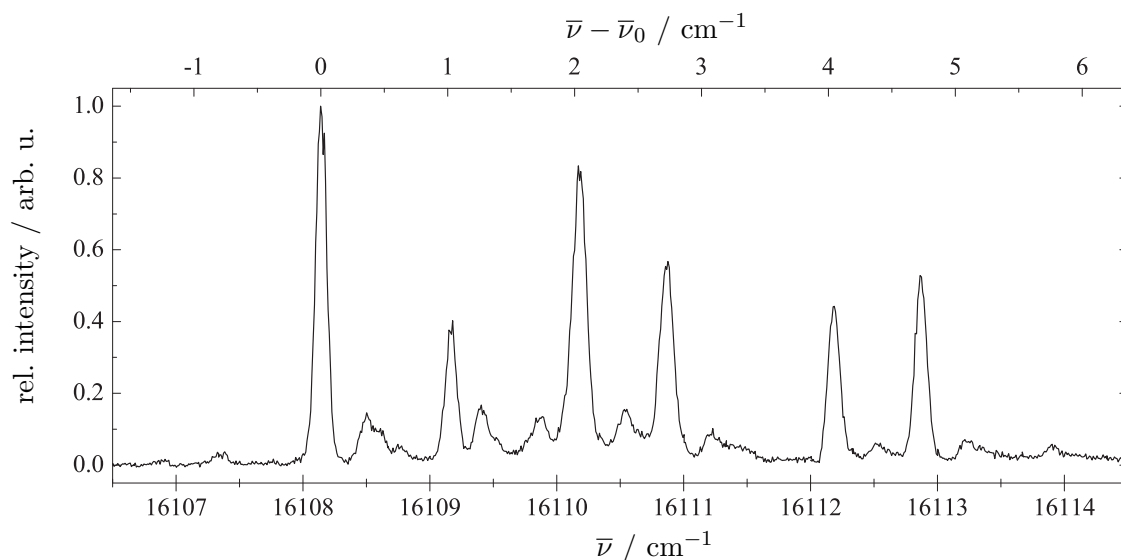


Fig. 7.30: Normalized fluorescence excitation spectrum of the electronic origin of Etio at $\bar{\nu}_0 = 16108.1 \text{ cm}^{-1}$ recorded with the continuous helium droplet setup.

allows in principle for four different configuration isomers where the ethyl and methyl groups are not necessarily arranged alternating around the porphyrin body as depicted in figure 7.28 but randomly which results in four possible isomers. On the other hand, an unknown number of isomers of the helium solvation shell close to the molecule is a plausible cause for the numerous lines exhibited in the excitation spectrum of figure 7.30. Since obviously more than four lines are present within the spectral fine structure of the electronic origin of Etio either both effects or only the latter contribute to the excitation spectrum.

7.6.2 Dispersed emission of Etio

The dispersed emission spectrum of Etio for excitation at the electronic origin ($\bar{\nu}_{exc} = 16108.1 \text{ cm}^{-1}$) is displayed in figure 7.31. Apart from the intense signal at the excitation frequency, which is predominantly due to laser stray light since this spectrum was corrected with a background spectrum taken with closed entrance slit of the spectrograph, sharp lines are present throughout the entire spectrum.

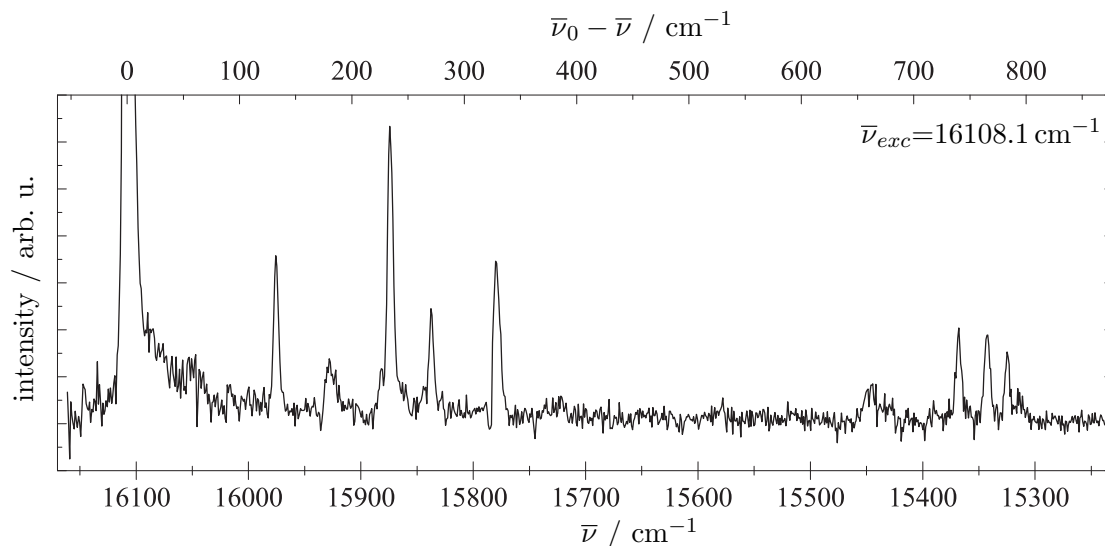


Fig. 7.31: Dispersed emission spectrum of Etio for excitation at 16108.1 cm^{-1} . The intense signal at the excitation frequency is predominantly due to laser stray light.

Table 7.12 lists the absolute frequencies $\bar{\nu}$ of all observed signals as well as the frequencies relative to the electronic origin at 16108 cm^{-1} which correspond to the vibrational modes of the electronic ground state $\bar{\nu}_{rel}(S_0) = \bar{\nu}_0 - \bar{\nu}$. The latter values are compared to the corresponding values $\bar{\nu}_{rel}(S_1^x)$ derived from the fluorescence excitation spectrum. The deviations in per cent between the vibrational modes of S_0 and the electronically excited state are also tabulated. Examining the results, one can readily recognize that, apart from the transition at $\bar{\nu}_{rel} = 179 \text{ cm}^{-1}$, good agreement is found for all transitions extracted from both, fluorescence excitation and dispersed emission spectrum. Regarding the rather low intensity of the vibrational modes in general in the fluorescence excitation spectrum (cf. figure 7.29) it is likely that the comparably weak mode at $\bar{\nu}_{rel} = 179 \text{ cm}^{-1}$ is not present in the fluorescence excitation spectrum due to its low transition probability.

Tab. 7.12: Vibronic transitions $\bar{\nu}$ obtained from the dispersed emission spectrum of Etio by excitation at the electronic origin ($\bar{\nu}_{exc} = 16108.1 \text{ cm}^{-1}$). The frequencies could be determined with an accuracy of 1 cm^{-1} (cf. chapter 4.1.3.2). $\bar{\nu}_{rel} (S_0)$ gives the frequencies relative to the electronic origin $\bar{\nu}_0 = 16108.1 \text{ cm}^{-1}$ corresponding to the vibrational transitions of S_0 . For comparison, column three lists the vibrational transitions $\bar{\nu}_{rel} (S_1^x)$ of the electronically excited state S_1^x . $\Delta\bar{\nu}_{rel} (S_0 \text{ to } S_1^x)$ is the deviation in percent between the two values taking $\bar{\nu}_{rel} (S_0)$ as reference value.

$\bar{\nu} / \text{cm}^{-1}$	$\bar{\nu}_{rel} (S_0) / \text{cm}^{-1}$	$\bar{\nu}_{rel} (S_1^x) / \text{cm}^{-1}$	$\Delta\bar{\nu}_{rel} (S_0 \text{ to } S_1^x) / \%$
16108	0	0	0.0
15977	131	127	-3.1
15929	179	-	-
15875	233	226	-3.0
15839	269	273	+1.5
15781	327	322	-1.5
15448	660	653	-1.1
15370	738	723	-2.0
15345	763	-	-
15326	782	-	-

Exciting Etio at the different resonances displayed in figure 7.30 leads to emission at the respective excitation frequency as is demonstrated exemplarily for excitation at 16108.1 cm^{-1} and 16110.2 cm^{-1} (cf. figure 7.32). The stray light corrected emission spectra are equally shifted with the excitation frequency. This phenomenon of differing emission origins was also observed for emission spectra of AlClPc (cf. chapter 6.1.2). Although the emission frequencies of Etio at the emission origin are different for the various signals, the overall spectral structure with all vibrational modes remains identical. However, as is illustrated in figure 7.33 slight changes can be observed in the vibronic transitions although there is no obvious correlation between excitation frequency and shift of a particular vibrational mode. Thus, one can

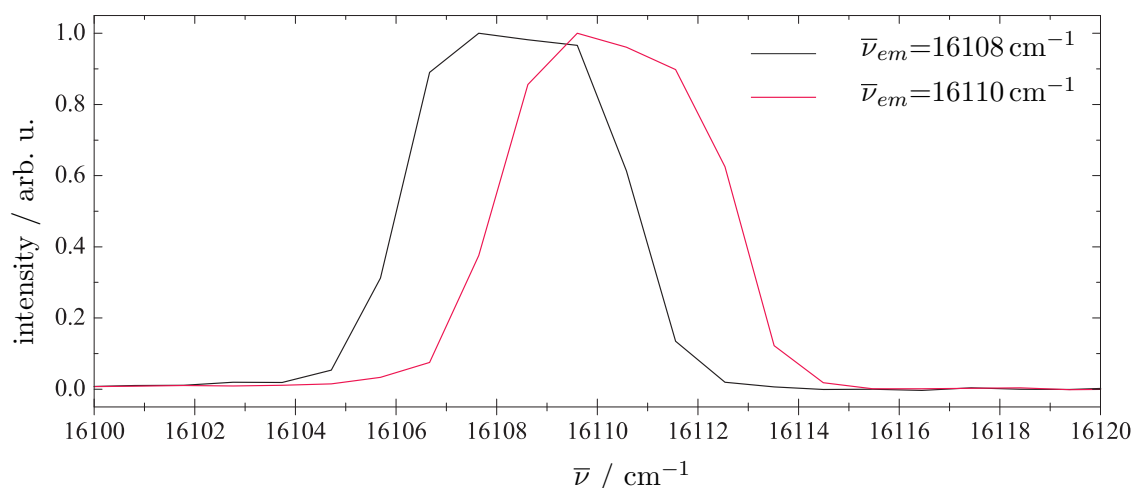


Fig. 7.32: Dispersed emission spectra of Etio for excitation at different frequencies at the electronic origin (cf. figure 7.30), namely $\bar{\nu}_{exc} = 16108.1 \text{ cm}^{-1}$ (black) and $\bar{\nu}_{exc} = 16110.2 \text{ cm}^{-1}$ (red). The stray light corrected emission is equally shifted with the excitation frequency.

conclude that each sharp signal of the excitation spectrum forms its own system. As was already discussed in section 7.6.1, the presence of several species within the Etio sample can either be caused by four different configurational isomers due to the arrangement of the substituents or by different isomers of the helium solvation shell around the molecule which may relax or not prior to radiative decay. Though, an unambiguous assignment remains impossible. Based on the HPLC analysis of the Etio sample (cf. appendix) [74], other impurities than potential configurational isomers can be excluded and, moreover, their frequencies would be expected to be more significantly shifted concerning their electronic transitions.

To summarize, the close similarity of the vibrational modes in S_0 and S_1^x (so-called: mirror symmetry) as observed for Etio indicates that only minor changes of the nuclear arrangement take place upon electronic excitation. In contrast to previous investigations on methyl-substituted anthracene [11], namely 2-methylanthracene, Etio shows no drastic line broadening in its fluorescence excitation spectrum although torsional motion of the methyl and ethyl groups should be allowed.

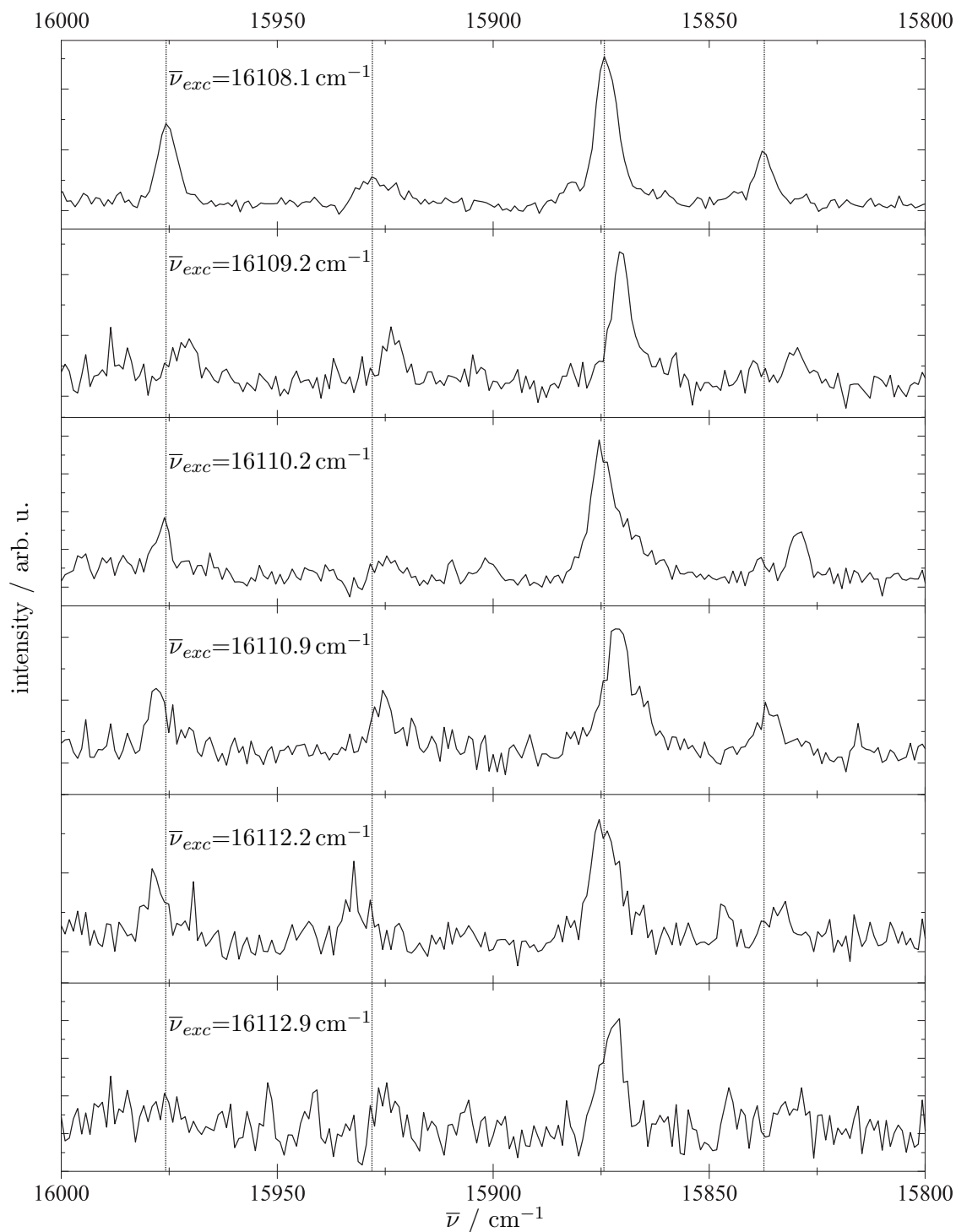


Fig. 7.33: Section of the dispersed emission spectra of Etio for excitation at the six most intense lines of the electronic origin (cf. figure 7.30). The respective excitation frequency is given in each panel. As a guide to the eye dotted lines are plotted which mark the vibrational modes for excitation at $\bar{\nu}_{exc} = 16108.1 \text{ cm}^{-1}$.

Nevertheless, the fine structure in the electronic origin as well as the sensitive reaction of vibrational modes upon electronic excitation is a clear indicator for the coupling of the molecule to its surrounding cryomatrix.

7.7 Comparative summary of the porphyrin species

7.7.1 Fine structure of electronic transitions

Due to the higher spectral resolution compared to dispersed emission spectra, the fine structure of the electronic origins of the previously discussed porphyrin derivatives (cf. chapters 7.1 to 7.6) will be analyzed on the basis of the fluorescence excitation spectra. An overview of the electronic origins is given in figure 7.34. Although for all molecules sharp lines are present with line widths ranging from 0.07 cm^{-1} in the case of DPP up to 0.25 cm^{-1} in the case of FBP, clear differences are visible.

The top panel of figure 7.34 shows the electronic origin of FBP which is considered as benchmark system. The zero phonon line consists of one very intense line followed by two peaks of similar line width and greatly reduced intensity. This feature repeats for the first signal group of the electronic origins of DPP, TPC, TMP (for $\bar{\nu}_0 = 15429.4\text{ cm}^{-1}$), TPrP and Etio.

As the number and size of the substituent increases the fine structure within the first few wavenumbers at the electronic origin increases (cf. for example TPrP and Etio). While the number of possible isomeric variants does not suffice, the appearance of isomeric solvation complexes or of low energy modes of the substituents are possible explanations.

Apparently, the electronic origin of TMP (for $\bar{\nu}_0 = 15045.8\text{ cm}^{-1}$) stands out due to the fact that not the first line within the electronic origin is the most intense one. Moreover, no alternation between intense and weak lines exists, but instead, starting from a weak signal the intensity of sharp lines increases and finally merges into a broad spectral feature.

Regarding the line widths of vibronic transitions in the fluorescence excitation spectra – as far as can be deduced from the data available for FBP, DPP and TPrP (cf. chapters 7.1.1, 7.2.1 and 7.5.1) – the line widths stay approximately within the same order of magnitude as is observed for the corresponding electronic origin. This

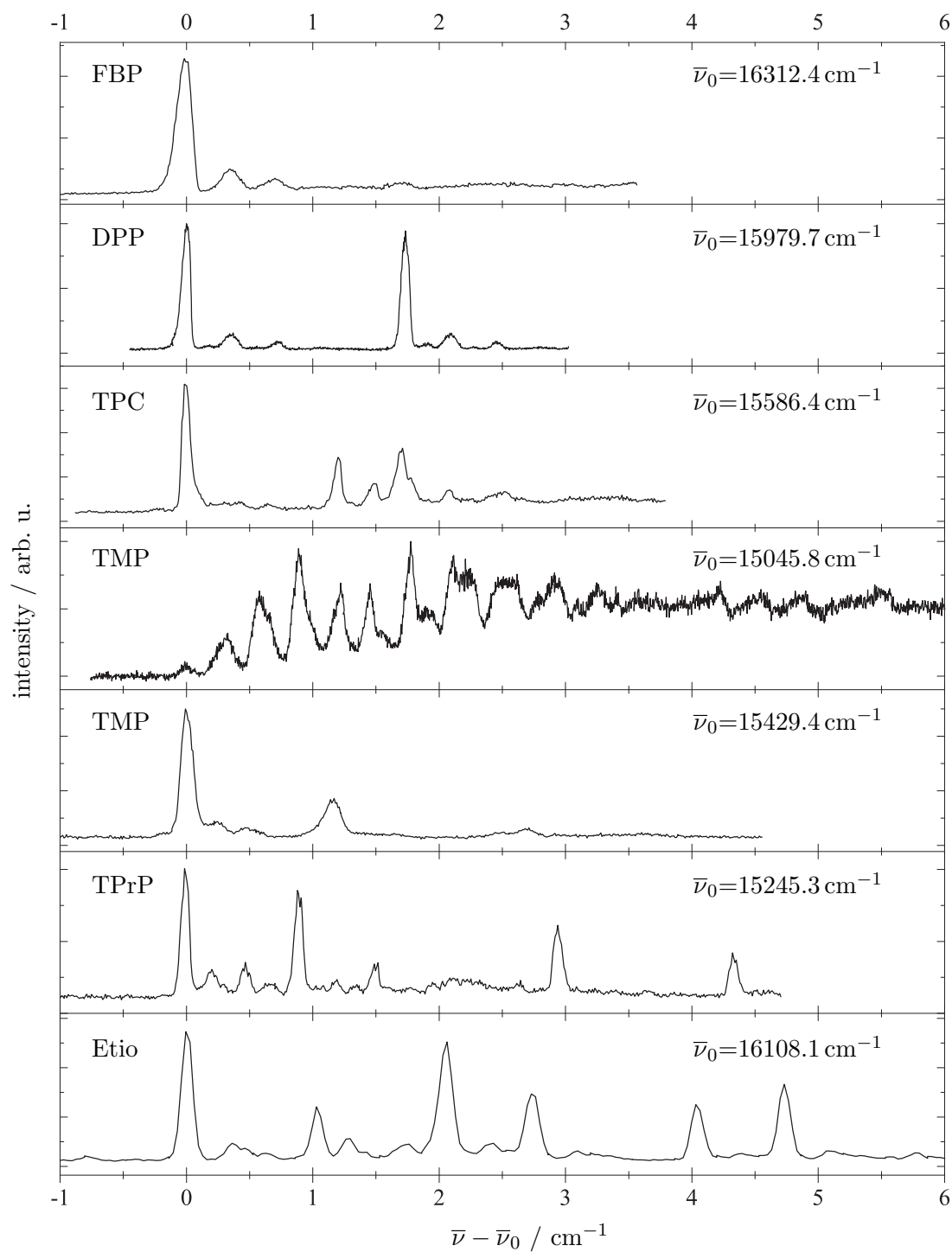


Fig. 7.34: Fluorescence excitation spectra of all porphyrin species discussed in chapters 7.1 to 7.6 showing the electronic origins. The components are indicated in each panel. The wavenumber scale is relative to the respective electronic origin which is also given for each panel.

finding, along with the equivalent conclusion that the life times of the vibrational modes do not significantly deviate from that of the pure electronic transitions (electronic origin), can be explained by fortunate internal vibrational redistribution of the vibrational energy into the surrounding helium droplet mediated via the substituents. Exclusively focussing on the electronic origin, the presence of substituents which inherently enhances the density of states obviously does not lead to a significantly increased transfer ratio since FBP possesses the largest line width of all porphyrins under investigation.

7.7.2 Vibrational mode structure in dispersed emission

The dispersed emission spectra of the porphyrin species (cf. chapters 7.1 to 7.6) will be used to discuss the vibrational mode structure since high-resolution measurements of fluorescence excitation spectra with the continuous helium droplet setup including vibronic transitions were only possible for two porphyrins, namely FBP and TPrP. Generally, one can state that sharp signals are present for all spectra displayed in figure 7.35.

Apart from the dispersed emission spectrum of TPC, all porphyrin derivatives exhibit similar intensity within the range of their vibrational modes. Since the emission spectrum reflects the Franck-Condon factors, this can be interpreted as similar transition probabilities for all molecular vibrations. In the case of TPC, as an exception, one significantly dominating mode is visible at $\bar{\nu}_0 - \bar{\nu} = 191 \text{ cm}^{-1}$ indicating a strongly favored vibrational transition.

Analyzing the dispersed emission spectra of the substituted porphyrins, the TPC and TMP spectra present an additional comparably broad low-energy mode around $\bar{\nu}_0 - \bar{\nu} = 20 - 40 \text{ cm}^{-1}$ while for TPrP and Etio – molecules that show a variety of sharp intense and weak signals at the electronic origin in the fluorescence excitation spectra (cf. chapter 7.7.1 figure 7.34) – this transition is missing.

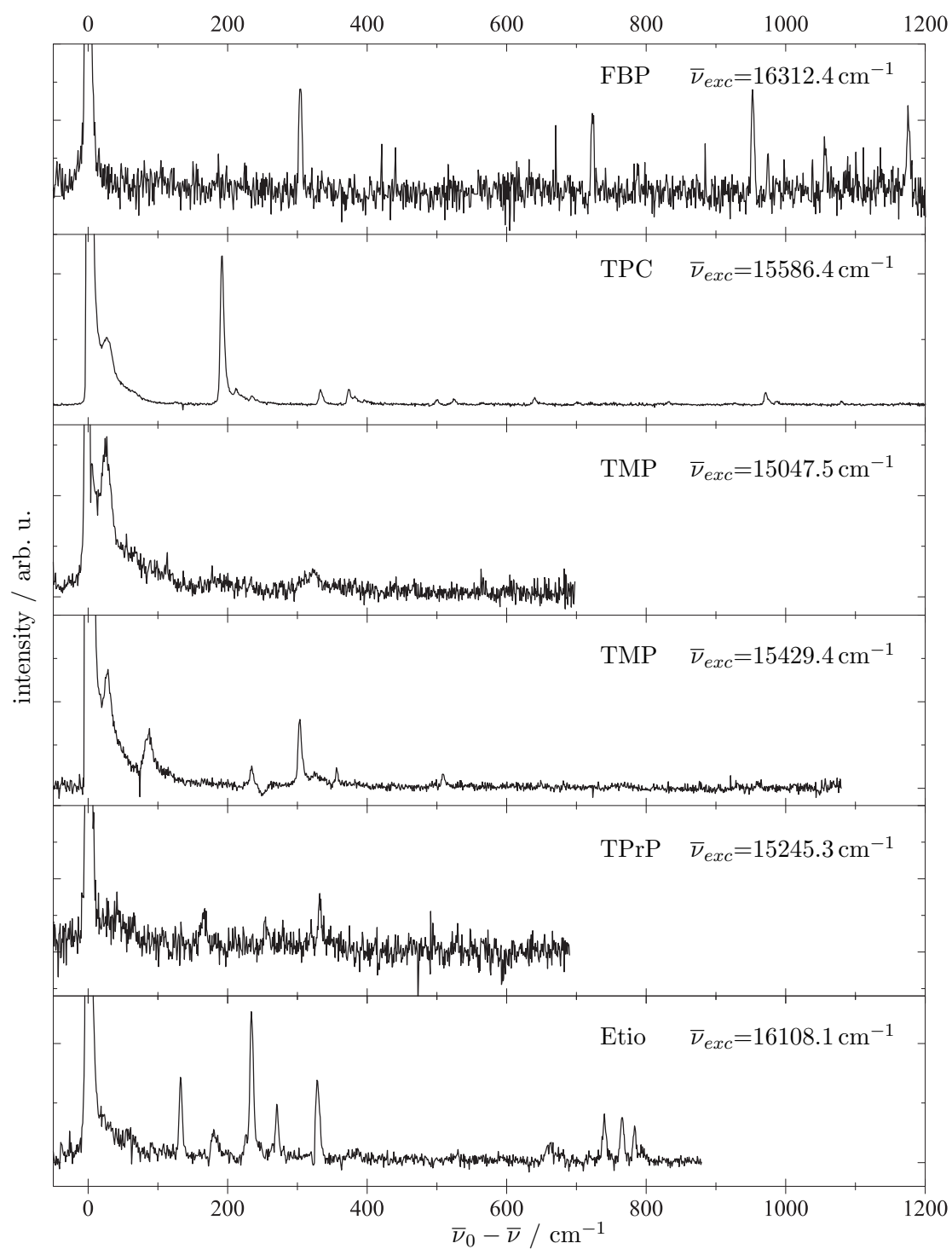


Fig. 7.35: Dispersed emission spectra for all porphyrin species discussed in chapters 7.1 to 7.6 except for DPP. The components are indicated in each panel. The wavenumber scale is relative to the electronic origin or alternatively the excitation frequency which is also given for each panel.

8 Conclusion

In the course of modifying the continuous helium droplet source by implementing a new closed-cycle cryostat, new adjustment of the nozzle unit to the beam axis which is defined by the skimmer and pick-up cell openings became necessary. While doing so, variation of the nozzle position and stagnation conditions to gain maximum fluorescence signal from free-base phthalocyanine revealed not just a single optimum position (case **(1)**)(see chapter 5). Two additional positions (case **(2)**) peaking in intensity were found with the nozzle opening vertically displaced from the regular droplet beam axis by 7.5 mm. As could be concluded from the differing stagnation conditions to gain maximum fluorescence signal for case **(1)** and **(2)**, the initially produced helium droplets differed in their mean droplet sizes by about two orders of magnitude at which the droplets generated in case **(2)** were the larger ones. Furthermore, the asymmetric shape of the ZPL of phthalocyanine was used to estimate droplet sizes after the pick-up process for both cases. While the line shape and spectral position remained constant for the droplets doped with single phthalocyanine molecules in case **(2)**, droplet sizes for case **(1)** varied markedly with the nozzle temperature that led to production of helium droplets large enough to host at least one phthalocyanine molecule. In the latter case, broadening accompanied by a blue shift of the ZPL was observed when initially generating droplets smaller than ~ 8000 atoms while line shape and spectral position were steady when initially generating droplets up to mean droplet sizes of 2000000 atoms. Due to the displacement of the nozzle from the regular beam axis, case **(2)** was finally interpreted as a fraction of the initially produced droplet beam with a mean droplet size of about 2000000 atoms that fragments into a larger number of smaller droplets upon impact

on the skimmer surface and is subsequently reflected back into the optical axis of the continuous machine. This was also confirmed by a geometrical calculation of incident and reflected beam.

The spectroscopic part of this study focussed on the investigation of a series of substituted phthalocyanines and porphyrins in superfluid helium droplets by means of high-resolution electronic spectroscopy using a continuous helium droplet source and a continuous wave dye laser as well as with a pulsed source and pulsed dye laser systems. The latter experiments became necessary since the photon flux of the continuous wave dye laser was not sufficient to record vibronic transitions for most porphyrin compounds. Thus, apart from the electronic origin, no information on the vibrational mode pattern of the electronically excited state was available because of the low fluorescence quantum yield. However, dispersed emission spectra measured with the continuous source provide information about the vibrational modes in the electronic ground state. The vibrational fine structure exhibited in the electronic spectra is supposed to give information about e.g. line shape, line width or line splitting. In a recent model focussing on line broadening phenomena, these factors are discussed to be indicative for intermolecular or intramolecular rearrangement following the electronic excitation of an organic molecule doped into helium droplets [64]. By choosing a series of molecules that is considered to possess a rather rigid molecular backbone, the interaction with the surrounding helium droplet is expected to be mediated via the floppy alkyl and aryl substituent groups.

Recording fluorescence excitation and dispersed emission spectra revealed exclusively sharp transitions for all species. Together with a peak intensity at the electronic origin, the spectra indicate that the molecular structure remains unchanged upon electronic excitation. Although, PWs dominating in their intensities over the ZPLs, even below any saturation limit, were observed when probing TMP with a pulsed dye laser (see chapter 7.4.1). Following the interpretation given in [25], this is an indication for a displacement of the equilibrium configuration of the solvation complex in S_0 and S_1 . This means considerable rearrangement of the helium atoms surrounding the molecular dopant. But, considering experiments performed with the continuous

dye laser, which provides a photon flux that is by about 5 to 6 orders of magnitude lower than for pulsed dye lasers (cf. chapter 3.1.2), the ZPL was the dominating spectral feature of the electronic origin for all molecules within this study with the exception of TMP. The fluorescence excitation spectrum of the latter was found to consist of contributions from two species. This spectroscopic finding was also confirmed by an HPLC analysis of our TMP sample [74]. The electronic origin of one compound within the TMP sample not only presented with a spectral shape that was never observed before in electronic spectra of organic molecules in superfluid helium droplets: a series of several sharp lines separated by about 0.3 cm^{-1} from each other was observed with increasing intensity from the first to the fourth and finally merging of the sharp lines into a broad unstructured band. It also exhibited a PW that was at least of comparable intensity to the ZPL even at the low photon flux provided by the continuous wave dye laser.

Even though sharp lines have been observed in the electronic spectra for all molecules investigated for this study, a result that is generally expected considering the cold helium droplet environment, several molecules in recent studies exhibited significant line broadening in their electronic spectra when doped into superfluid helium droplets (see for example [24]). At this, large amplitude motions were possible via e.g. methyl or phenyl groups [11] for some species and therefore a correlation of line broadening and intramolecular nuclear rearrangement seemed to be a plausible explanation. Taking into account an even larger set of experimental data, a recent attempt to interpret those findings proposes that broadening is a result of intramolecular charge redistribution initiated by the electronic excitation [64]. Precisely, a change of the molecule's electrostatic moments, primarily and most effectively, a change of the molecular dipole moment regarding both magnitude and orientation, was identified as the main contribution for line broadening effects. The ability of a molecule to allow for large amplitude motions is thus not mandatory for line broadening since rigid molecules like e.g. 3-hydroxyflavone [28] or fluorazene [24] exhibit broadened spectra as well. Furthermore, not all molecules with substituents that can undergo torsional motions or the like show line broadening in their electronic

spectra, e.g. the molecules investigated for this study. For the latter, the existence of a molecular dipole moment is excluded due to an inversion center of the symmetrically substituted compounds. Therefore, experiments performed for this study support the model that line broadening in electronic spectra of organic molecules in superfluid helium droplets is caused by intramolecular charge redistribution following the electronic excitation [64]. Hence, the solvation shell of helium atoms tightly adapted to the guest molecule needs to change its configuration in order to adapt to the new charge distribution. This adaption procedure obviously manifests in broadened transitions since the potential energy curves of S_0 and S_1 are considerably shifted against each other.

Apart from the sharp lines presented in their fluorescence excitation spectra, the phthalocyanine derivatives investigated for this study, namely AlClPc and TTBPc, exhibited more than one emission spectrum. In the case of AlClPc, in addition to the emission spectrum coinciding with the excitation spectrum, a second emission spectrum red shifted by 9 cm^{-1} was observed (see chapter 6.1.2). At this, the vibrational energies and Franck-Condon factors were identical for both spectra. The intensity ratio of the first compared to the second emission spectrum was 1:43. Following the interpretation derived from split emission spectra of free-base phthalocyanine and Mg-phthalocyanine, the existence of two emission spectra is interpreted as the result of a four level system consisting of a double minimum potential for both, S_0 and S_1 [27, 52, 90, 96]. Within this system, while the potential curves are not shifted against each other, the global minimum of S_0 corresponds to the local minimum in S_1 and vice versa. Therefore, energetic relaxation of the helium solvation configuration around the guest molecule from the local into the global minimum is believed to take place in S_1 following the electronic excitation and, again in S_0 , following the radiative decay. At this, the relaxation rate compared to the radiative decay rate of the excited molecule determines the intensity ratio between both emission spectra while the energy difference between the corresponding minima in S_0 and S_1 determines the spectral shift. Replacing one helium atom of the molecule's solvation shell by another rare gas atom like e.g. argon, i.e. forming AlClPc-Ar₁ van

der Waals clusters within the superfluid helium droplet, one aims to gain further insight into the dynamics of solvation structures next to the guest molecule. Recording dispersed emission spectra of those complexes revealed again more than one dispersed emission spectrum (see chapter 6.1.3). Yet, vibronic transitions were not just split into two spectra but multiplets consisting of three and more signals. This result is in line with triply split emission spectra observed for a van der Waals complex of free-base phthalocyanine and one argon atom [15, 27] which was, similarly explained with a multiple level system representing different solvation configurations of the first helium layer around the dopant. Combined with the split emission spectra recorded for bare AlClPc, both findings support the existence of different solvation structures of the helium solvation shell directly attached to the dopant. Comparably to AlClPc, for one species within our TTBPc sample a second emission spectrum with a red shift of 6 cm^{-1} was found for excitation at the electronic origin (see chapter 6.2.2). Thus, comparison of the current data with former experiments concentrating on phthalocyanine (derivatives) leads to the conclusion that adding four bulky alkyl groups to the phthalocyanine macrocycle in the case of TTBPc or alternatively replacing the inner hydrogen atoms of the macrocycle by a metal atom that additionally bears an axial ligand in the case of AlClPc, obviously do not alter specific solvation dynamics of phthalocyanines in superfluid helium droplets.

Future work may include the investigation of unsymmetrically substituted porphyrins or, due to their higher fluorescence quantum yields, preferably phthalocyanines that are capable of substantially changing their dipole moment which was found to be most effective concerning broadening of electronic spectra [64]. These experiments would aim at further pursuing the model that electronic excitation followed by a significant change of a molecule's electrostatic moments which, in turn, makes an adaption of the helium solvation shell to the recent changes of the electron density distribution necessary, is a key ingredient for line broadening [64]. Bearing in mind the ambition to get a reliable theory to predict line broadening, results from these experiments could help to confirm the recently proposed model.

Especially with regard to the results for TMP (see chapter 7.4.1), a further investigation of molecules that have been studied previously exclusively by means of the pulsed setup, e.g. pyrromethene derivatives [24, 64], by using the continuous machine seems worthwhile. Recording fluorescence excitation spectra benefitting from the higher spectral resolution of the continuous wave dye laser may reveal additional information about spectral fine structures in the case of molecules whose spectra were apparently dominated by PWs regardless of the laser intensity.

Although, various future experiments can certainly contribute to the understanding of the effects of electronic excitation on the solvation dynamics of organic molecules doped into superfluid helium droplets, theoretical work is needed as well providing quantitative simulations. Preferably, confirmation of the previously discussed model predicting line broadening is achieved in order to judge the chance of success in terms of gaining sharp electronic spectra for experiments concerning photochemistry of organic molecules in the dissipative environment of superfluid helium droplets. However, it is evident that calculating extremely weak interaction potentials for a molecule surrounded by quantum fluid is a challenging task.

Appendix

In the following, the results of the HPLC analyses [74] are presented for the majority of substances investigated for this study. For every substance the isoplot^a along with the UV-VIS absorption spectra for the main components are displayed. A Phenomenex Luna 3 10 μm C18 separating column was used for all samples in combination with a solvent mixture consisting of acetonitrile and water where the latter contained 0.0059 % (w/w) of trifluoroacetic acid. The composition of the eluent, starting with 5 % acetonitrile and 95 % water, was gradually changed during the separation process to finally reach 95 % of acetonitrile and 5 % of water after 20 minutes.

^aIsoplots display on the abscissa the retention time and on the ordinate a wavelength scale. The latter is defined by the diode array detector subsequent to the separating column. Intensity information is given via a false color representation. Note that the false color representation uses a logarithmic scale.

HPLC analysis of FBP

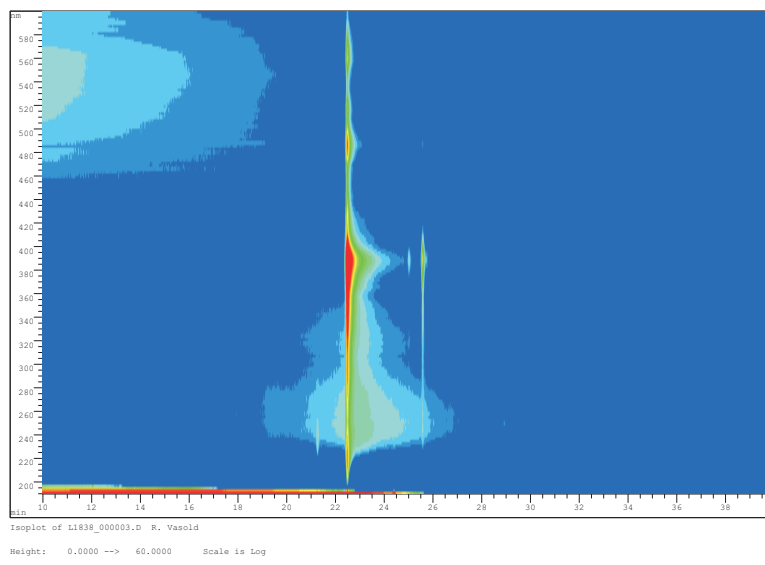


Fig. 8.1: Isoplot for the FBP sample.

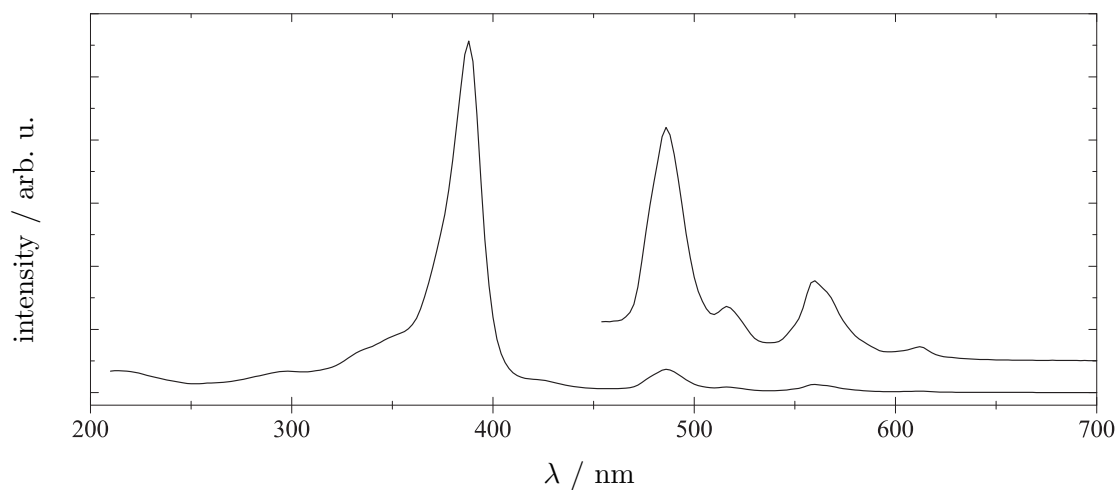


Fig. 8.2: UV-VIS absorption spectrum of the FBP sample at a retention time of 22.5 min. The spectral region of 450 – 700 nm is additionally displayed magnified by a factor of 10.

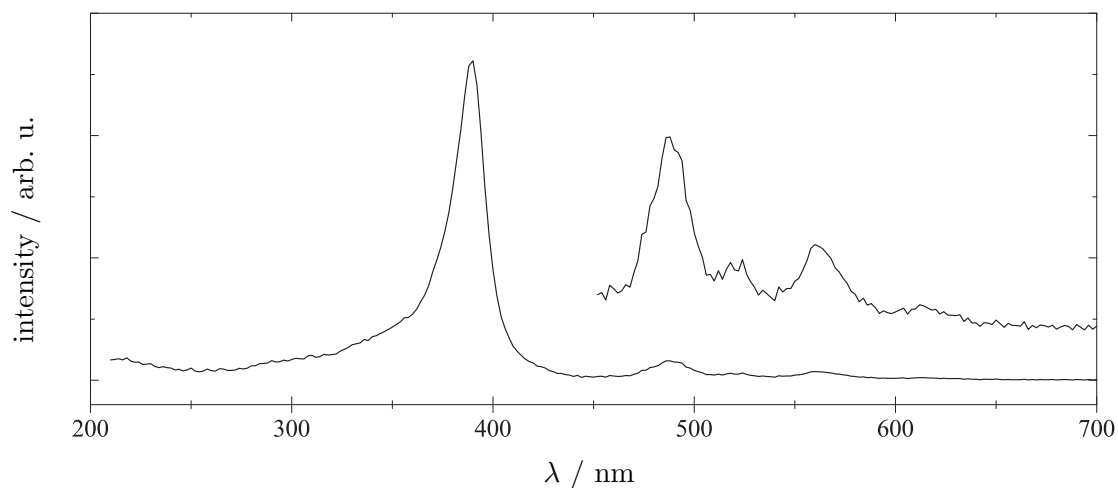


Fig. 8.3: UV-VIS absorption spectrum of the FBP sample at a retention time of 25.6 min.

The spectral region of 450 – 700 nm is additionally displayed magnified by a factor of 10.

Although an assignment of the two species within the FBP sample remains impossible, one can exclude the presence of chlorin impurities by comparison with absorption spectra of FBP and free-base chlorin from the literature (cf. [105]).

HPLC analysis of DPP

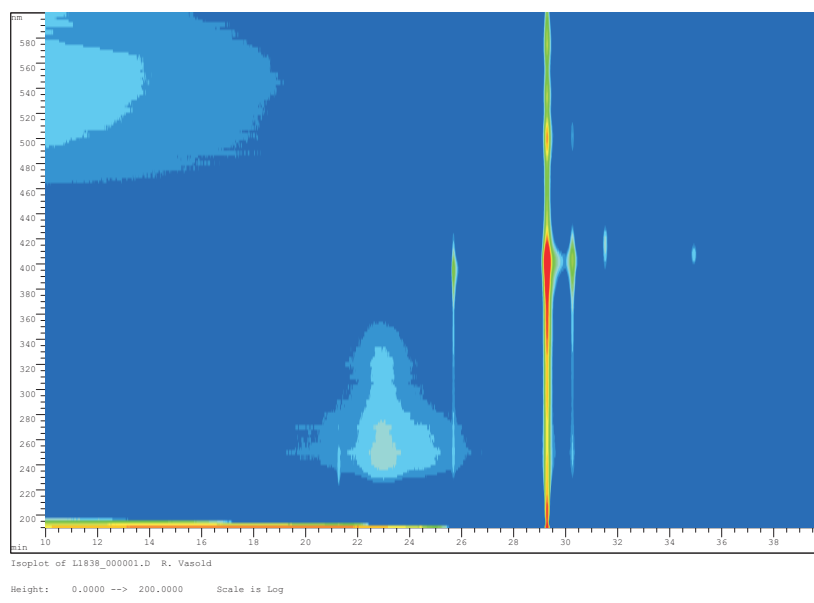


Fig. 8.4: Isoplot for the DPP sample.

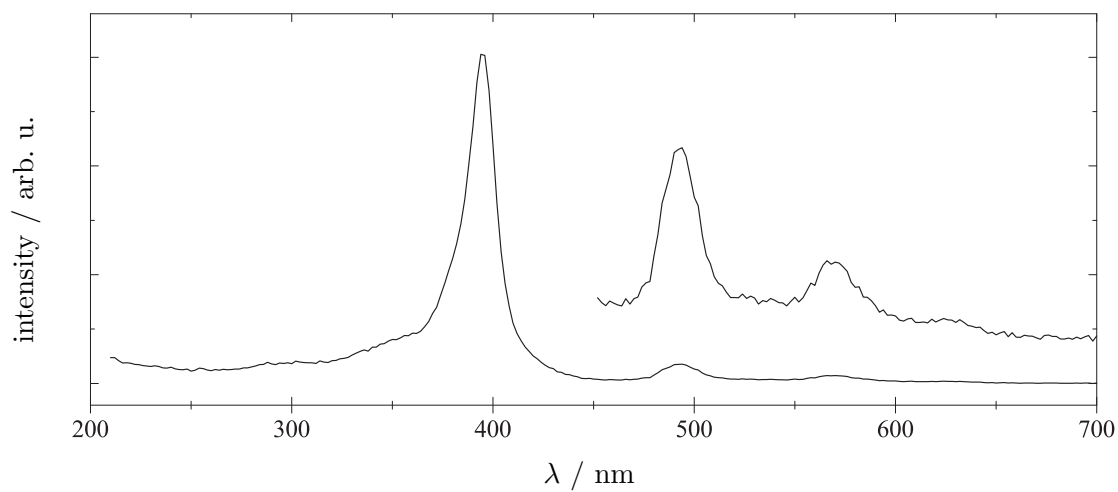


Fig. 8.5: UV-VIS absorption spectrum of the DPP sample at a retention time of 25.7 min. The spectral region of 450 – 700 nm is additionally displayed magnified by a factor of 10.

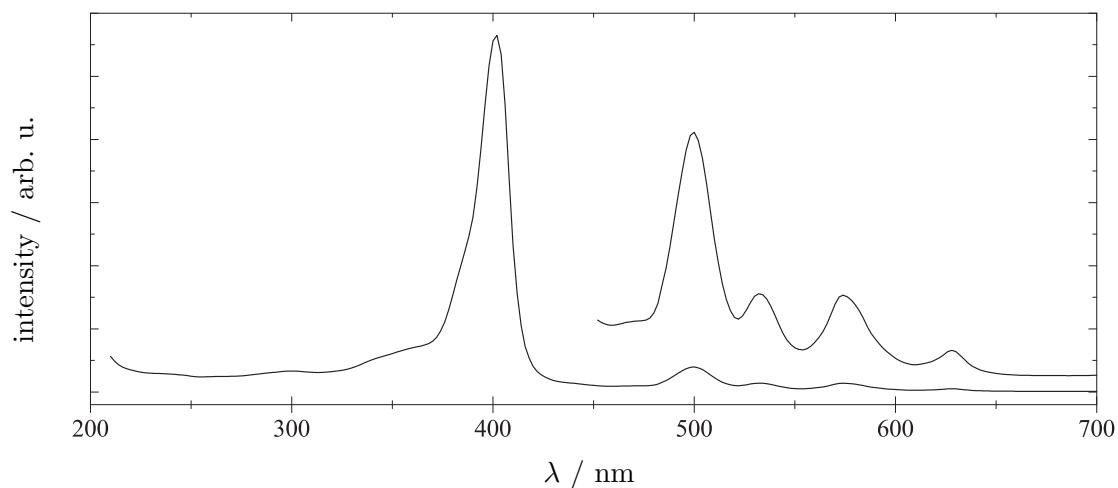


Fig. 8.6: UV-VIS absorption spectrum of the DPP sample at a retention time of 29.3 min. The spectral region of 450 – 700 nm is additionally displayed magnified by a factor of 10.

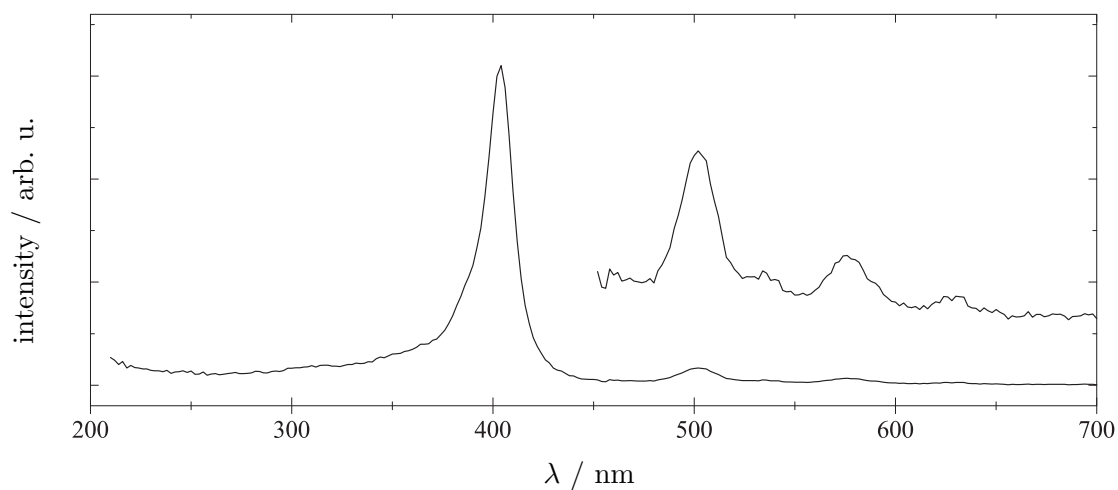


Fig. 8.7: UV-VIS absorption spectrum of the DPP sample at a retention time of 30.3 min. The spectral region of 450 – 700 nm is additionally displayed magnified by a factor of 10.

Although an assignment of the three species within the DPP sample remains impossible, one can exclude the presence of chlorin impurities by comparison with absorption spectra of 5,15-diphenylchlorin from the literature (cf. [124]).

HPLC analysis of TPP

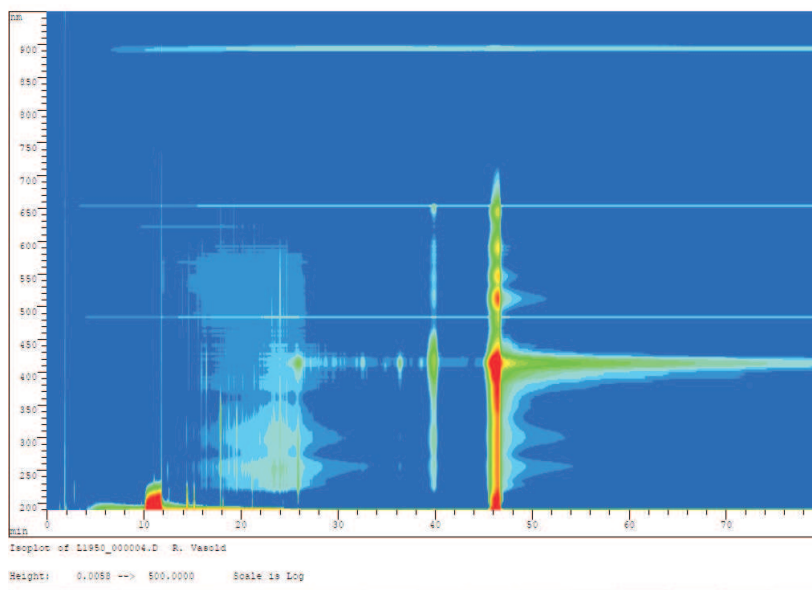


Fig. 8.8: Isoplot for the TPP sample.

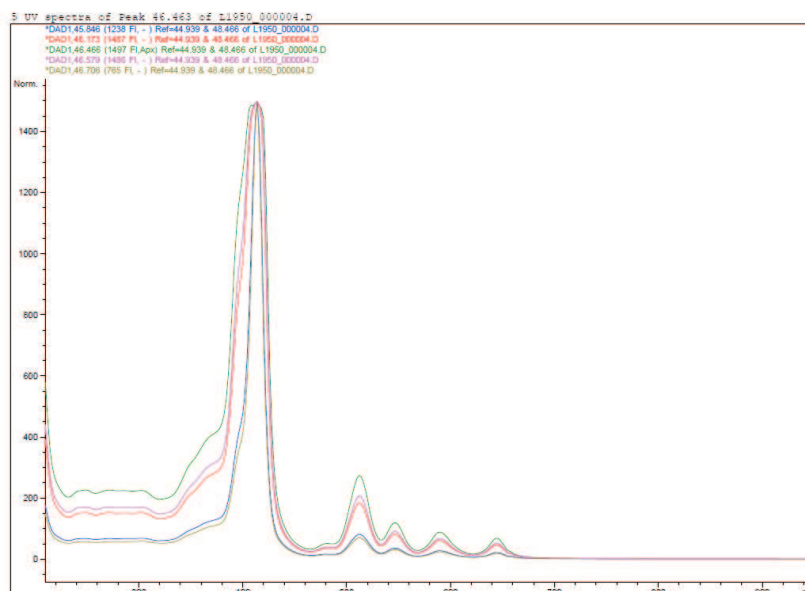


Fig. 8.9: UV-VIS absorption spectrum of the TPP sample at a retention time of about 46.5 min.

The spectrum depicted in figure 8.9 closely resembles data from the literature for TPP (cf. [125]). For an assignment of the species with a retention time of about 40 min see the section about HPLC analysis of TPC.

HPLC analysis of TPC

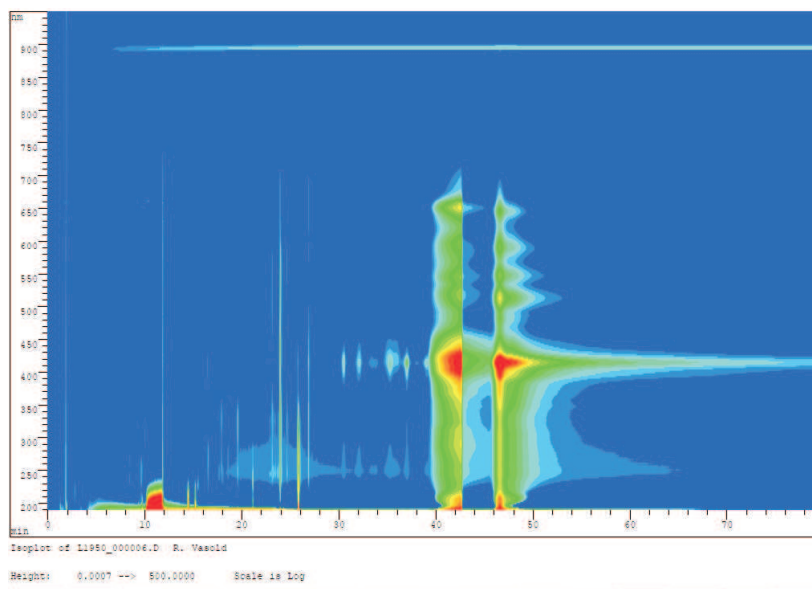


Fig. 8.10: Isoplot for the TPC sample.

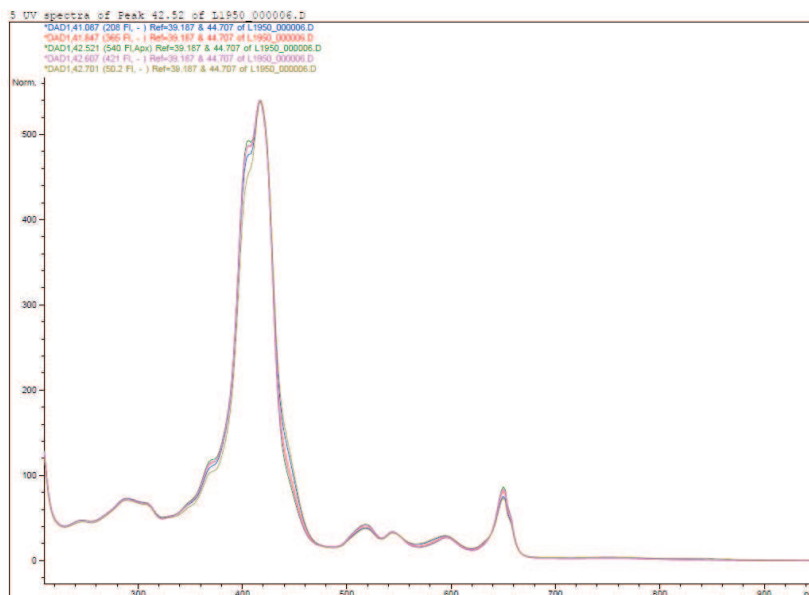


Fig. 8.11: UV-VIS absorption spectrum of the TPC sample at a retention time of about 41.8 min.

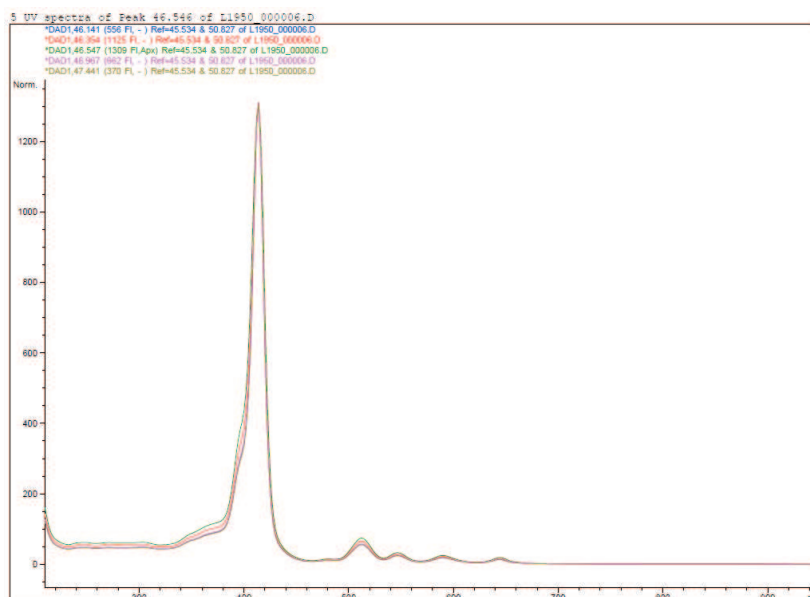


Fig. 8.12: UV-VIS absorption spectrum of the TPC sample at a retention time of about 46.5 min.

The spectrum depicted in figure 8.11 closely resembles data from the literature for TPC (cf. [126]) while the spectrum depicted in figure 8.12 closely resembles data from the literature for TPP (cf. [125]).

HPLC analysis of TMP

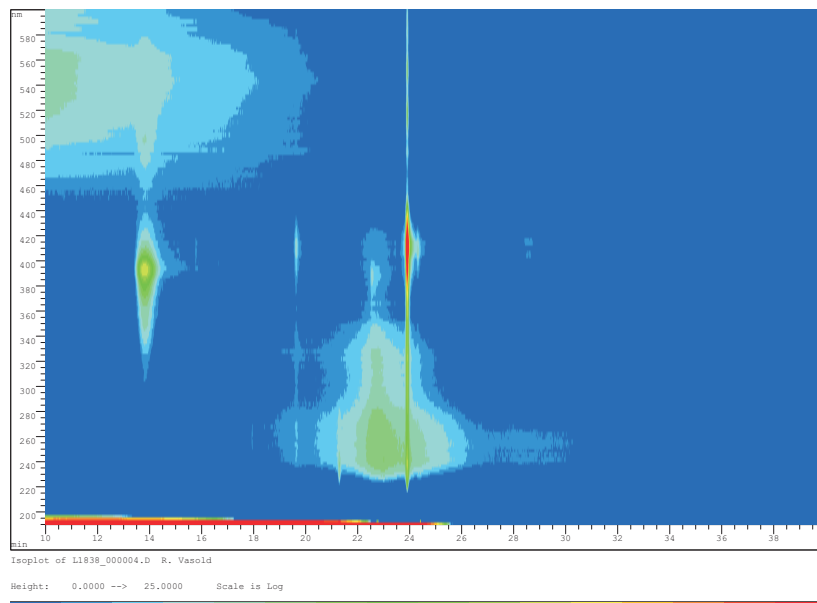


Fig. 8.13: Isoplot for the TMP sample.

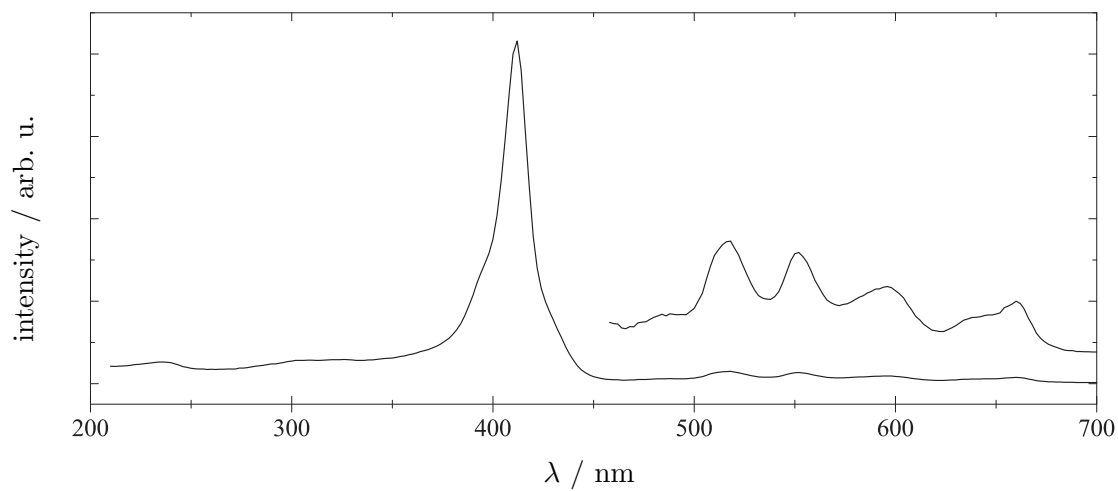


Fig. 8.14: UV-VIS absorption spectrum of the TMP sample at a retention time of 23.9 min. The spectral region of 450 – 700 nm is additionally displayed magnified by a factor of 10.

HPLC analysis of TPrP

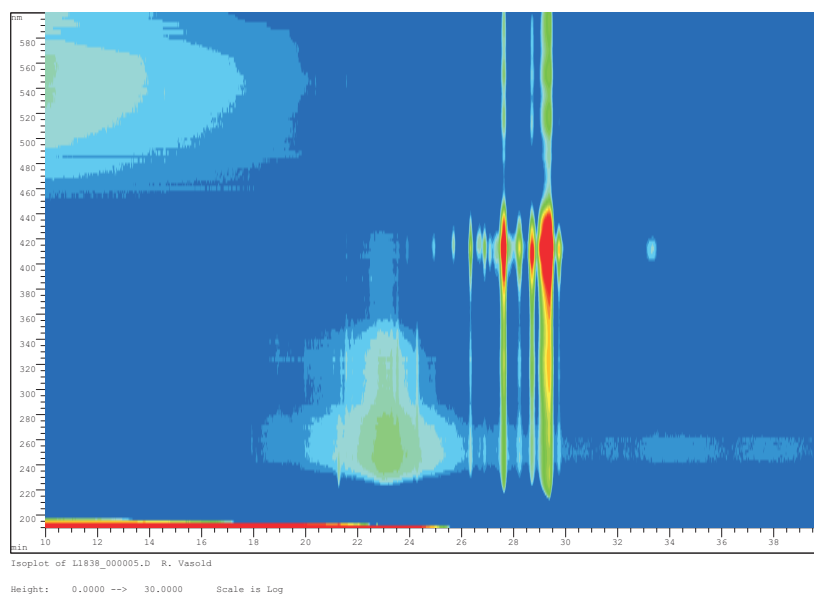


Fig. 8.15: Isoplot for the TPrP sample.

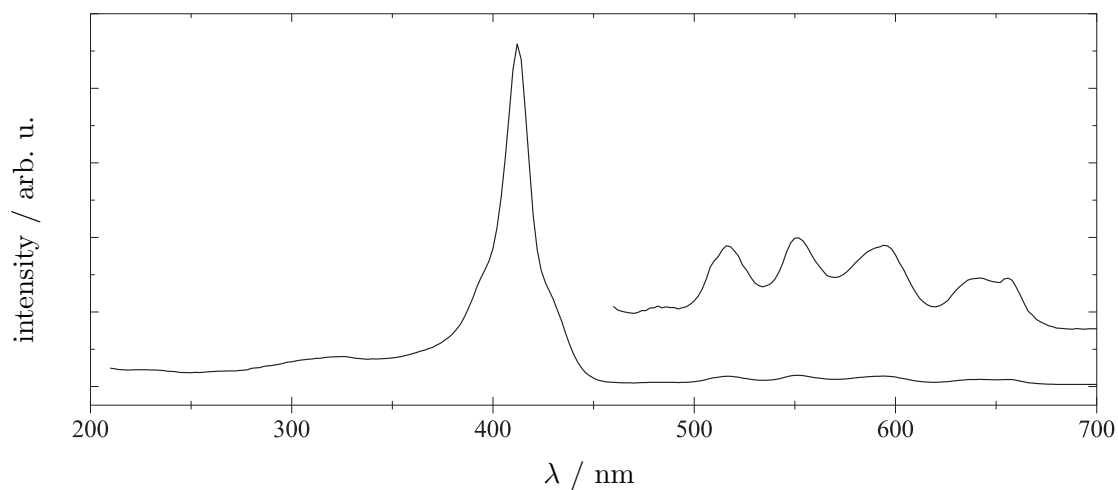


Fig. 8.16: UV-VIS absorption spectrum of the TPrP sample at a retention time of 27.6 min. The spectral region of 450 – 700 nm is additionally displayed magnified by a factor of 10.

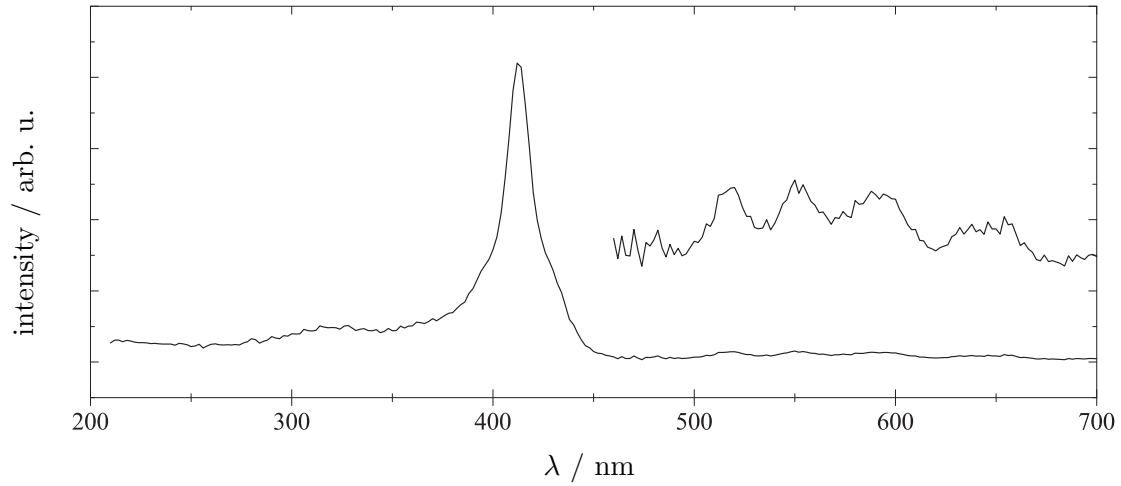


Fig. 8.17: UV-VIS absorption spectrum of the TPrP sample at a retention time of 28.2 min. The spectral region of 450 – 700 nm is additionally displayed magnified by a factor of 10.

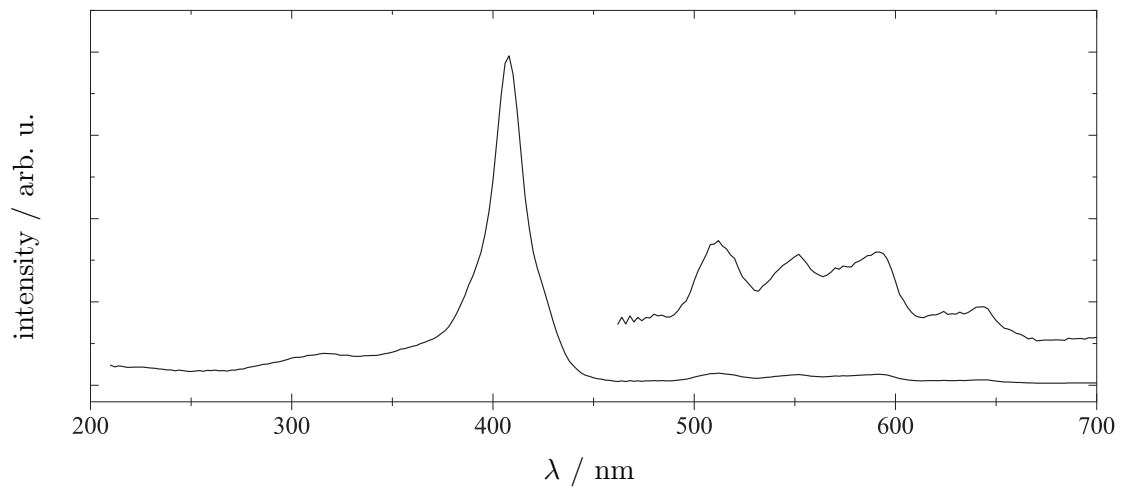


Fig. 8.18: UV-VIS absorption spectrum of the TPrP sample at a retention time of 28.7 min. The spectral region of 450 – 700 nm is additionally displayed magnified by a factor of 10.

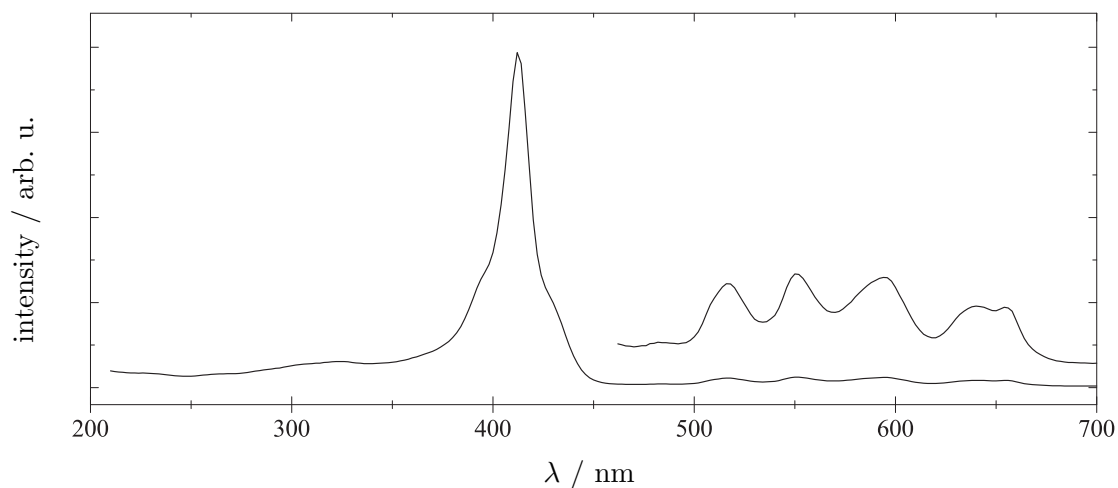


Fig. 8.19: UV-VIS absorption spectrum of the TPrP sample at a retention time of 29.4 min. The spectral region of 450 – 700 nm is additionally displayed magnified by a factor of 10.

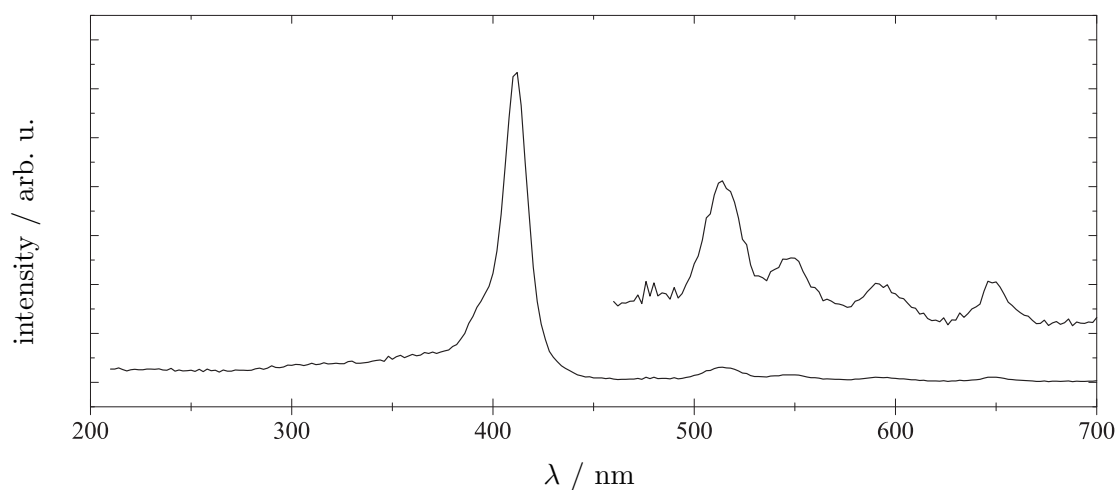


Fig. 8.20: UV-VIS absorption spectrum of the TPrP sample at a retention time of 29.7 min. The spectral region of 450 – 700 nm is additionally displayed magnified by a factor of 10.

HPLC analysis of Etio

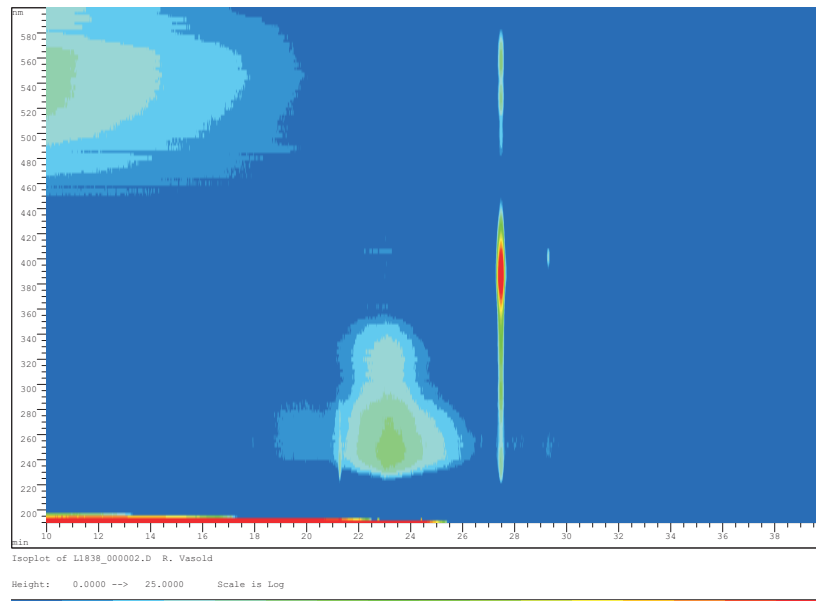


Fig. 8.21: Isoplot for the Etio sample.

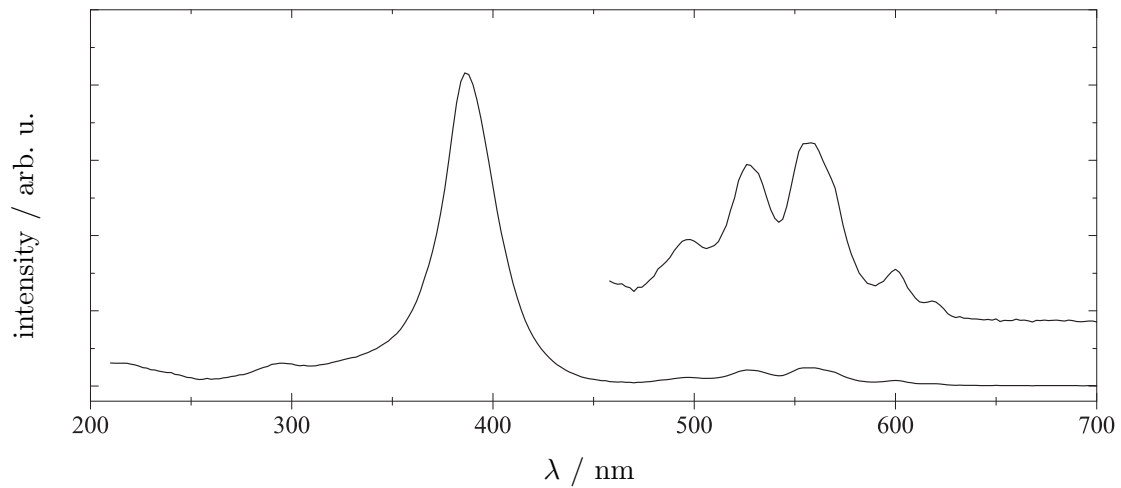


Fig. 8.22: UV-VIS absorption spectrum of the Etio sample at a retention time of 27.5 min. The spectral region of 450 – 700 nm is additionally displayed magnified by a factor of 10.

References

- [1] M. HARTMANN, R. E. MILLER, J. P. TOENNIES, and A. F. VILESOV, *Physical Review Letters* **75**, 1566 (1995).
- [2] F. STIENKEMEIER, J. HIGGINS, C. CALLEGARI, S. I. KANORSKY, W. E. ERNST, and G. SCOLES, *Zeitschrift für Physik D - Atoms, Molecules and Clusters* **38**, 253 (1996).
- [3] F. STIENKEMEIER, F. MEIER, and H. O. LUTZ, *The Journal of Chemical Physics* **107**, 10816 (1997).
- [4] A. PIFRADER, O. ALLARD, G. AUBÖCK, C. CALLEGARI, W. E. ERNST, R. HUBER, and F. ANCILOTTO, *The Journal of Chemical Physics* **133**, 164502/1 (2010).
- [5] K. NAUTA and R. E. MILLER, *The Journal of Chemical Physics* **113**, 9466 (2000).
- [6] S. GREBENEV, M. HARTMANN, M. HAVENITH, B. SARTAKOV, J. P. TOENNIES, and A. F. VILESOV, *The Journal of Physical Chemistry* **112**, 4485 (2000).
- [7] M. HARTMANN, A. LINDINGER, J. P. TOENNIES, and A. F. VILESOV, *Physical Chemistry Chemical Physics* **4**, 4839 (2002).
- [8] R. LEHNIG and A. SLENCZKA, *The Journal of Chemical Physics* **122**, 244317/1 (2005).
- [9] M. Y. CHOI, F. DONG, and R. E. MILLER, *Philosophical Transactions of the Royal Society of London, Series A: Mathematical, Physical and Engineering Sciences* **363**, 393 (2005).

- [10] Ö. BIRER, P. MORESCHINI, K. K. LEHMANN, and G. SCOLES, *The Journal of Physical Chemistry A* **111**, 12200 (2007).
- [11] D. PENTLEHNER, C. GREIL, B. DICK, and A. SLENCZKA, *The Journal of Chemical Physics* **133**, 114505/1 (2010).
- [12] M. HARTMANN, R. E. MILLER, J. P. TOENNIES, and A. F. VILESOV, *Science* **272**, 1631 (1996).
- [13] S. GREBENEV, B. G. SARTAKOV, J. P. TOENNIES, and A. F. VILESOV, *The Journal of Chemical Physics* **118**, 8656 (2003).
- [14] D. T. MOORE and R. E. MILLER, *The Journal of Chemical Physics* **119**, 4713 (2003).
- [15] R. LEHNIG, J. A. SEBREE, and A. SLENCZKA, *Journal of Physical Chemistry A* **111**, 7576 (2007).
- [16] S. RUDIĆ, J. M. MERRITT, and R. E. MILLER, *The Journal of Chemical Physics* **124**, 104305/1 (2006).
- [17] J. KÜPPER and J. M. MERRITT, *International Reviews in Physical Chemistry* **26**, 249 (2007).
- [18] E. LUGOVOJ, J. P. TOENNIES, and A. VILESOV, *The Journal of Chemical Physics* **112**, 8217 (2000).
- [19] S. A. KRASNOKUTSKI and F. HUISKEN, *The Journal of Physical Chemistry A* **114**, 7292 (2010).
- [20] C. CALLEGARI, K. K. LEHMANN, R. SCHMIED, and G. SCOLES, *The Journal of Chemical Physics* **115**, 10090 (2001).
- [21] J. P. TOENNIES and A. F. VILESOV, *Angewandte Chemie* **116**, 2674 (2004).
- [22] M. Y. CHOI, G. E. DOUBERLEY, T. M. FALCONER, W. K. LEWIS, C. M. LINDSAY, J. M. MERRITT, P. L. STILES, and R. E. MILLER, *International Reviews in Physical Chemistry* **25**, 15 (2006).
- [23] F. STIENKEMEIER and K. K. LEHMANN, *Journal of Physics B* **39**, R127 (2006).

- [24] D. PENTLEHNER, *Perturbations of Electronic Transitions of Organic Molecules in Helium Droplets Generated with a New Pulsed Droplet Source*, PhD Thesis, Universität Regensburg, 2010.
- [25] E. LOGINOV, D. ROSSI, and M. DRABBELS, *Physical Review Letters* **95**, 163401/1 (2005).
- [26] R. LEHNIG, M. SLIPCHENKO, S. KUMA, T. MOMOSE, B. SARTAKOV, and A. VILESOV, *The Journal of Chemical Physics* **121**, 9396 (2004).
- [27] R. LEHNIG and A. SLENCZKA, *European Journal of Chemical Physics and Physical Chemistry* **5**, 1014 (2004).
- [28] R. LEHNIG, D. PENTLEHNER, A. VDOVIN, B. DICK, and A. SLENCZKA, *The Journal of Chemical Physics* **131**, 194307/1 (2009).
- [29] H. BUCHENAU, E. L. KNUTH, J. NORTHBY, J. P. TOENNIES, and C. WINKLER, *The Journal of Chemical Physics* **92**, 6875 (1990).
- [30] D. R. TILLEY and J. TILLEY, *Superfluidity and Superconductivity*, Institute of Physics, Bristol, 1990.
- [31] U. HENNE and J. P. TOENNIES, *Journal of Chemical Physics* **108**, 9327 (1998).
- [32] M. LEWERENZ, B. SCHILLING, and J. P. TOENNIES, *Chemical Physics Letters* **206**, 381 (1993).
- [33] J. HARMS, J. P. TOENNIES, and F. DALFOVO, *Physical Review B* **58**, 3341 (1998).
- [34] O. KORNILOV and J. P. TOENNIES, *International Journal of Mass Spectrometry* **280**, 209 (2009).
- [35] W. SCHÖLLKOPF and J. P. TOENNIES, *Science* **266**, 1345 (1994).
- [36] T. JIANG and J. A. NORTHBY, *Physical Review Letters* **68**, 2620 (1992).
- [37] E. L. KNUTH and U. HENNE, *The Journal of Physical Chemistry* **110**, 2664 (1999).

- [38] M. FÁRNÍK, U. HENNE, B. SAMELIN, and J. P. TOENNIES, *Zeitschrift für Physik D - Atoms, Molecules and Clusters* **40**, 93 (1997).
- [39] R. E. GRISENTI and J. P. TOENNIES, *Physical Review Letters* **90**, 234501/1 (2003).
- [40] B. SCHILLING, *Molekularstrahlexperimente mit Helium-Clustern*, PhD Thesis, Max-Planck-Institut für Strömungsforschung, Göttingen, 1993.
- [41] D. M. BRINK and S. STRINGARI, *Zeitschrift für Physik D - Atoms, Molecules and Clusters* **15**, 257 (1990).
- [42] J. HARMS, M. HARTMANN, J. P. TOENNIES, and A. F. VILESOV, *Journal of Molecular Spectroscopy* **185**, 204 (1997).
- [43] M. LEWERENZ, B. SCHILLING, and J. P. TOENNIES, *The Journal of Chemical Physics* **102**, 8191 (1995).
- [44] M. IINO, M. SUZUKI, and A. J. IKUSHIMA, *Journal of Low Temperature Physics* **61**, 155 (1985).
- [45] S. A. CHIN and E. KROTSCHKEK, *Physical Review B* **52**, 10405 (1995).
- [46] S. STRINGARI and J. TREINER, *Journal of Chemical Physics* **87**, 5021 (1987).
- [47] R. FRÖCHTENICHT, J. P. TOENNIES, and A. VILESOV, *Chemical Physics Letters* **229**, 1 (1994).
- [48] B. DICK and A. SLENCZKA, *The Journal of Chemical Physics* **115**, 10206 (2001).
- [49] F. ANCILOTTO, P. B. LERNER, and M. W. COLE, *Journal of Low Temperature Physics* **101**, 1123 (1995).
- [50] F. STIENKEMEIER and A. F. VILESOV, *The Journal of Chemical Physics* **115**, 10119 (2001).
- [51] J. P. TOENNIES and A. F. VILESOV, *Annual Review of Physical Chemistry* **49**, 1 (1998).
- [52] R. LEHNIG, *Anregungs- und Emissionsspektroskopie von organischen Molekülen in ^4He -Tröpfchen*, PhD Thesis, Universität Regensburg, 2004.

- [53] S. KRASNOKUTSKI, G. ROUILLÉ, and F. HUISKEN, *Chemical Physics Letters* **406**, 386 (2005).
- [54] A. AMIRAV, U. EVEN, and J. JORTNER, *The Journal of Chemical Physics* **75**, 3770 (1981).
- [55] M. HARTMANN, *Hochauflösende Spektroskopie von Molekülen in ⁴Helium- und ³Helium-Clustern*, PhD Thesis, Max-Planck-Institut für Strömungsforschung Göttingen, 1997.
- [56] U. EVEN, J. MAGEN, and J. JORTNER, *Chemical Physics Letters* **88**, 131 (1982).
- [57] J. JORTNER, *Zeitschrift für Physik D Atoms, Molecules and Clusters* **24**, 247 (1992).
- [58] S. RUDOLPH, G. WOLLNY, K. VON HAEFTEN, and M. HAVENITH, *The Journal of Chemical Physics* **126**, 124318/1 (2007).
- [59] A. SLENCZKA, B. DICK, M. HARTMANN, and J. P. TOENNIES, *The Journal of Chemical Physics* **115**, 10199 (2001).
- [60] A. LINDINGER, E. LUGOVOJ, J. P. TOENNIES, and A. F. VILESOV, *Zeitschrift für Physikalische Chemie* **215**, 401 (2001).
- [61] M. HARTMANN, A. LINDINGER, J. P. TOENNIES, and A. F. VILESOV, *Journal of Physical Chemistry A* **105**, 6369 (2001).
- [62] Ö. BIRER, P. MORESCHINI, K. K. LEHMANN, and G. SCOLES, *Journal of Physical Chemistry A* **111**, 7624 (2007).
- [63] M. XU and Z. BAČIĆ, *Journal of Physical Chemistry A* **111**, 7653 (2007).
- [64] R. RIECHERS, D. PENTLEHNER, A. VDOVIN, G. M. PÖTZL, and A. SLENCZKA, *The Journal of Chemical Physics*, submitted (2011).
- [65] S. GREBENEV, M. HARTMANN, A. LINDINGER, N. PÖRTNER, B. SARTAKOV, J. P. TOENNIES, and A. F. VILESOV, *Physica B* **280**, 65 (2000).
- [66] M. HARTMANN, F. MIELKE, J. P. TOENNIES, and A. F. VILESOV, *Physical Review Letters* **76**, 4560 (1996).

- [67] R. J. DONNELLY, J. A. DONNELLY, and R. N. HILLS, *Journal of Low Temperature Physics* **44**, 471 (1981).
- [68] Y. KWON and K. B. WHALEY, *The Journal of Chemical Physics* **114**, 3163 (2001).
- [69] P. HUANG, H. D. WHITLEY, and K. B. WHALEY, *Journal of Low Temperature Physics* **134**, 263 (2004).
- [70] H. D. WHITLEY, P. HUANG, Y. KWON, and K. B. WHALEY, *The Journal of Chemical Physics* **123**, 054307/1 (2005).
- [71] Y. RALCHENKO, F.-C. JOU, D. E. KELLEHER, A. E. KRAMIDA, A. MUSGROVE, J. READER, W. L. WIESE, and K. OLSEN, *NIST Atomic Spectra Database (version 3.1.2)*, National Institute of Standards and Technology, Gaithersburg, MD, 2007.
- [72] D. PENTLEHNER, R. RIECHERS, B. DICK, A. SLENCZKA, U. EVEN, N. LAVIE, R. BROWN, and K. LURIA, *Review of Scientific Instruments* **80**, 043302/1 (2009).
- [73] U. KENSY, Institut für Physikalische und Theoretische Chemie, Universität Regensburg, 93053 Regensburg, Germany.
- [74] R. VASOLD, Analytik-Abteilung für HPLC und GC, Universität Regensburg, 93053 Regensburg, Germany.
- [75] E. W. BECKER, J. GSPANN, and G. KRIEG, *Entropie* **30**, 59 (1969).
- [76] W. STECKELMACHER, *Reports on Progress in Physics* **49**, 1083 (1986).
- [77] B. I. KHARISOV, U. O. MÉNDEZ, J. L. ALMARAZ GARZA, and J. R. ALMAGUER RODRÍGUEZ, *New Journal of Chemistry* **29**, 686 (2005).
- [78] R. W. BOYLE, C. C. LEZNOFF, and J. E. VAN LIER, *British Journal of Cancer* **67**, 1177 (1993).
- [79] W.-S. CHAN, N. BRASSEUR, C. LA MADELEINE, R. OUELLET, and J. E. VAN LIER, *European Journal of Cancer* **33**, 1855 (1997).

- [80] M. R. DETTY, S. L. GIBSON, and S. J. WAGNER, *Journal of Medicinal Chemistry* **47**, 3897 (2004).
- [81] A. K. SHUKLA, C. PALITEIRO, R. MANOHARAN, A. HAMNETT, and J. B. GOODENOUGH, *Journal of Applied Electrochemistry* **19**, 105 (1989).
- [82] A. GALAL, S. A. DARWISH, and R. A. AHMED, *Journal of Solid State Electrochemistry* **11**, 521 (2007).
- [83] C. A. BARKER, X. ZENG, S. BETTINGTON, A. S. BATSANOV, M. R. BRYCE, and A. BEEBY, *Chemistry - A European Journal* **13**, 6710 (2007).
- [84] D. DINI, M. BARTHEL, and M. HANACK, *European Journal of Organic Chemistry* **2001**, 3759 (2001).
- [85] K.-L. LAW, *Chemical Reviews* **93**, 449 (1993).
- [86] P. S. VINCETT, E. M. VOIGT, and K. E. RIECKHOFF, *The Journal of Chemical Physics* **55**, 4131 (1971).
- [87] P. S. H. FITCH, C. A. HAYNAM, and D. H. LEVY, *The Journal of Chemical Physics* **73**, 1064 (1980).
- [88] P. S. H. FITCH, L. WHARTON, and D. H. LEVY, *The Journal of Chemical Physics* **70**, 2018 (1979).
- [89] P. S. H. FITCH, C. A. HAYNAM, and D. H. LEVY, *The Journal of Chemical Physics* **74**, 6612 (1981).
- [90] R. LEHNIG and A. SLENCZKA, *The Journal of Chemical Physics* **118**, 8256 (2003).
- [91] F. L. PLOWS and A. C. JONES, *Journal of Molecular Spectroscopy* **194**, 163 (1999).
- [92] L. PEI, J. ZHANG, and W. KONG, *The Journal of Chemical Physics* **127**, 174308/1 (2007).
- [93] L. PEI, J. ZHANG, W. KONG, D. XU, and H. GUO, *Chemical Physics Letters* **462**, 173 (2008).

- [94] T. STRENALYUK, S. SAMDAL, and H. V. VOLDEN, *The Journal of Physical Chemistry A* **112**, 9075 (2008).
- [95] T.-H. HUANG, K. E. RIECKHOFF, and E. M. VOIGT, *The Journal of Chemical Physics* **77**, 3424 (1982).
- [96] R. LEHNIG and A. SLENCZKA, *The Journal of Chemical Physics* **120**, 5064 (2004).
- [97] M. HARTMANN, A. LINDINGER, J. P. TOENNIES, and A. F. VILESOV, *Chemical Physics* **239**, 139 (1998).
- [98] P. ÇARÇABAL, R. SCHMIED, K. K. LEHMANN, and G. SCOLES, *The Journal of Chemical Physics* **120**, 6792 (2004).
- [99] M. C. BERENBAUM, S. L. AKANDE, R. BONNETT, H. KAUR, S. IOANNOU, R. D. WHITE, and U.-J. WINFIELD, *British Journal of Cancer* **54**, 717 (1986).
- [100] M. B. GARIBOLDI, R. RAVIZZA, P. BARANYAI, E. CARUSO, S. BANFI, S. MESCHINI, and E. MONTI, *Bioorganic & Medicinal Chemistry* **17**, 2009 (2009).
- [101] T. VIRGILI, D. G. LIDZEY, and D. D. C. BRADLEY, *Advanced Materials* **12**, 58 (2000).
- [102] A. T. GRADYUSHKO and M. P. TSVIRKO, *Optika i Spektroskopiya* **31**, 548 (1971).
- [103] B. F. MINAEV and A. B. MINAEV, *Optics and Spectroscopy* **98**, 214 (2005).
- [104] L. EDWARDS, D. H. DOLPHIN, M. GOUTERMAN, and A. D. ADLER, *Journal of Molecular Spectroscopy* **38**, 16 (1971).
- [105] U. NAGASHIMA, T. TAKADA, and K. OHNO, *The Journal of Chemical Physics* **85**, 4524 (1986).
- [106] U. EVEN and J. JORTNER, *The Journal of Chemical Physics* **77**, 4391 (1982).
- [107] C. M. WESTERN, *PGOPHER 7.1.108 A Program for Simulating Rotational Structure*, University of Bristol, <http://pgopher.chm.bris.ac.uk>, 2010.

- [108] B. LOCKE, T. LIAN, and R. M. HOCHSTRASSER, *Chemical Physics* **158**, 409 (1991).
- [109] S. GREBENEV, J. P. TOENNIES, and A. VILESOV, *Science* **279**, 2083 (1998).
- [110] C. CALLEGARI, A. CONJUSTEAU, I. REINHARD, K. K. LEHMANN, G. SCOLLES, and F. DALFOVO, *Physical Review Letters* **83**, 5058 (1999).
- [111] K. NAUTA and R. E. MILLER, *The Journal of Chemical Physics* **111**, 3426 (1999).
- [112] C. CALLEGARI, A. CONJUSTEAU, I. REINHARD, K. K. LEHMANN, G. SCOLLES, and F. DALFOVO, *Physical Review Letters* **84**, 1848 (2000).
- [113] S. J. SILVERS and A. TULINSKY, *The Journal of the American Chemical Society* **89**, 3331 (1967).
- [114] P. G. SEYBOLD and M. GOUTERMAN, *Journal of Molecular Spectroscopy* **31**, 1 (1969).
- [115] R. BALLARDINI, B. COLONNA, M. T. GANDOLFI, S. A. KALOVIDOURIS, L. ORZEL, F. M. RAYMO, and J. F. STODDART, *European Journal of Organic Chemistry* **2003**, 288 (2003).
- [116] P. P. KUMAR and B. G. MAIYA, *New Journal of Chemistry* **27**, 619 (2003).
- [117] M. GOUTERMAN and G.-E. KHALIL, *Journal of Molecular Spectroscopy* **53**, 88 (1974).
- [118] M.-C. DESROCHES, S. LAYAC, P. PROGNON, P. MAILLARD, D. S. GRIERSON, E. CURIS, I. NICOLIS, and A. KASSELOURI, *Applied Spectroscopy* **57**, 950 (2003).
- [119] U. EVEN, J. MAGEN, J. JORTNER, J. FRIEDMAN, and H. LEVANON, *The Journal of Chemical Physics* **77**, 4374 (1982).
- [120] S. SMOLAREK, A. M. RIJS, W. J. BUMA, and M. DRABBELS, *Physical Chemistry Chemical Physics* **12**, 15600 (2010).
- [121] S. M. ARABEI, D. V. NOVIK, and T. A. PAVICH, *Journal of Applied Spectroscopy* **73**, 511 (2006).

-
- [122] S. M. ARABEI, V. A. KUZMITSKY, and K. N. SOLOVYOV, *Optics and Spectroscopy* **102**, 692 (2007).
- [123] M. P. TSVIRKO, K. N. SOLOV'EV, A. T. GRADYUSHKO, and S. S. DVORNIKOV, *Journal of Applied Spectroscopy* **20**, 403 (1974).
- [124] T. Y. WANG, J. R. CHEN, and J. S. MA, *Dyes and Pigments* **52**, 199 (2002).
- [125] G. D. DOROUGH, J. R. MILLER, and F. M. HUENNEKENS, *Journal of the American Chemical Society* **73**, 4315 (1951).
- [126] G. D. DOROUGH and F. M. HUENNEKENS, *Journal of the American Chemical Society* **74**, 3974 (1952).

Acknowledgements

A huge thank you goes to my supervisor Prof. Dr. Alkwin Slenczka for his motivation, encouragement, support and the freedom to let me work so independently.

I thank Prof. Dr. Bernhard Dick for useful hints and never letting me forget to think outside the box.

Big thanks go to all former and current members of the helium droplet research group, namely Dr. Alexander Vdovin, Dr. Dominik Pentlechner, Tobias Premke, Eva-Maria Wirths and Lars Christiansen. Thanks for the great team spirit and always being supportive and bearing a hand when necessary.

I am also grateful to my office fellows Dr. Andreas Schmaunz, Dr. Andreas Wenge, Nicole Berner and our 'neighbour' PD Dr. Stephan Bäurle. They are fantastic colleagues always willing to exchange ideas, philosophize about everything under the sun, make a short trip, and lend a hand when heavy things need to be moved or join me at the sports club.

Sincere thanks go as well to Dr. Anja Stromeck-Faderl, Roger-Jan Kutta, Christian Greil, Manuel Schneider and Kathrin Magerl for being great colleagues.

People who contributed to this work by enabling me to concentrate on the scientific issues are Madlene von Sanden-Flohe, Martina Müller and Klaus Ziereis. I highly appreciate your work!

Equally indispensable is the contribution made by Dr. Uwe Kensy who is always willing to share his technical expertise. I also wish to thank the staff of the mechanical and electronic workshops for realizing my ideas as fast as possible.

Last but not least, I would like to thank my family for their great support and belief in me.